Pressure gradient and compressibility effects on high-speed boundary layer stability

by

Miguel A. Ramirez Mendez

A thesis submitted in partial fulfillment of the requirements for the degree of

Doctor of Philosophy
in
Mechanical Engineering

UNIVERSITY OF PUERTO RICO
MAYAGÜEZ CAMPUS

May 2025

Approved by:

Guillermo Araya, Ph.D. President, Graduate Committee	Date
Frederick Just, Ph.D. Co-President, Graduate Committee	Date
Marco Menegozzo, Ph.D. Member, Graduate Committee	Date
Wilson Rivera, Ph.D. Member, Graduate Committee	Date
Dilsom Sanchez Quintero, Ph.D. Representative of the Office of Graduate Studies	Date
Silvina Cancelos, Ph.D. Chairperson of the Department	Date

ABSTRACT

A deeper understanding of the fundamental physics underlying high-speed aerodynamics is pivotal for the advancement of more sophisticated control methodologies for fluid dynamics (e.g., wave drag minimization) and the mitigation of aerodynamic heating in vehicle design. *Blunt bodies immersed in viscous, compressible flows exhibit a distinctively long laminar boundary layer downstream of the stagnation point.* This thin region is critical in governing the majority of transport phenomena between the body and the surrounding fluid flow, with the dynamics being primarily influenced by the Navier-Stokes (NS) equations and the energy conservation principles. Moreover, the complexity of the geometry may lead to the development of localized streamwise pressure gradients, which can have profound effects on the aerothermodynamics characteristics. The Falkner-Skan family of flows represents a class of similarity solutions pertinent to laminar boundary layer flows over a wedge subjected to a pressure gradient, where the external flow velocity varies according to a power law. The incompressible and compressible boundary layer momentum and energy equations are numerically solved through the application of similarity analysis and Finite Difference schemes. This methodology effectively reduces the governing partial differential equations (PDEs) to a system of ordinary differential equations (ODEs) by exploiting a reduced set of independent variables. Subsequently, the resultant mean streamwise velocity and its associated derivatives, derived from the Falkner-Skan (FS) flow, are incorporated into the classical Orr-Sommerfeld equation governing the dynamics of small disturbances for flow stability analysis. This study is primarily concerned with the laminar and early transitional regimes of wall-bounded viscous flows. To accurately assess the impact of external flow conditions on the onset of transition, stability theory is applied to predict the precise conditions at which transition occurs within the laminar boundary layer. The present study systematically examines the following external conditions: (i) compressibility effects, (ii) Reynolds number influence, (iii) wall curvature, (iv) wall thermal boundary conditions, (v) fluid viscosity law, and (vi) radiation heat transfer. These factors collectively encompass the full spectrum of potential scenarios for laminar boundary layers.

RESUMEN

Una comprensión más profunda de la física fundamental que subyace en la aerodinámica a alta velocidad es crucial para el desarrollo de metodologías de control más sofisticadas para la dinámica de fluidos (por ejemplo, la minimización de la resistencia de ondas) y la mitigación del calentamiento aerodinámico en el diseño de vehículos. *Los cuerpos romos inmersos en flujos viscosos y compresibles exhiben una capa límite laminar notablemente larga aguas abajo del punto de estancamiento.* Esta región delgada es fundamental para gobernar la mayoría de los fenómenos de transporte entre el cuerpo y el flujo de fluido circundante, con la dinámica siendo principalmente influenciada por las ecuaciones de Navier-Stokes (NS) y los principios de conservación de la energía. Además, la complejidad de la geometría puede dar lugar al desarrollo de gradientes de presión locales en la dirección del flujo, lo que puede tener efectos profundos en las características aerotérmicas. La familia de flujos de Falkner-Skan representa una clase de soluciones de similitud pertinentes a los flujos laminares de capa límite sobre una cuña sometida a un gradiente de presión, donde la velocidad del flujo externo varía según una ley de potencia. Las ecuaciones de momento y energía de la capa límite, tanto incomprensibles como compresibles, se resuelven numéricamente mediante la aplicación del análisis de similitud y los esquemas de Diferencias Finitas. Esta metodología reduce eficazmente las ecuaciones diferenciales parciales (PDEs) que gobiernan el sistema a un conjunto de ecuaciones diferenciales ordinarias (ODEs) al explotar un conjunto reducido de variables independientes. Posteriormente, la velocidad media en la dirección del flujo resultante y sus derivadas asociadas, derivadas del flujo de Falkner-Skan (FS), se incorporan en la ecuación clásica de Orr-Sommerfeld que gobierna la dinámica de pequeñas perturbaciones para el análisis de estabilidad del flujo. Este estudio se centra principalmente en los regímenes laminares y tempranos de transición de los flujos viscosos confinados por la pared. Para evaluar con precisión el impacto de las condiciones externas del flujo en el inicio de la transición, se aplica la teoría de estabilidad. El presente estudio examina sistemáticamente las siguientes condiciones externas: (i) efectos de la compresibilidad, (ii) influencia del número de Reynolds, (iii) curvatura de la pared, (iv) condiciones térmicas de la pared, (v) ley de viscosidad del fluido, y (vi) transferencia de calor por radiación. Estos factores abarcan colectivamente todo el espectro de posibles escenarios para las capas límite laminares.

Acknowledgments

First and foremost, I would like to express my deepest gratitude to my advisor, Prof. Araya, for his unwavering support throughout my Ph.D. studies and related research. His patience, motivation, and vast expertise have been invaluable. His insightful guidance and mentorship were instrumental in both the research process and the development of this thesis.

Besides my advisor, I would like to thank the rest of my thesis committee: Prof. Frederick Just, Prof. Marco Menegozzo, and Prof. Wilson Rivera, for their insightful comments and encouragement, but also for the hard questions that encouraged me to widen my research from various perspectives.

I would like to express my sincere gratitude to the National Science Foundation for its invaluable support through grants #2314303 and #1847241, which provided the critical resources necessary to conduct this research. Similarly, my deepest thanks go to the Air Force Office of Scientific Research for its sponsorship under agreement number FA9550-23-1-0241, which played a pivotal role in defining the scope and depth of this work.

-Miguel A. Ramirez

This page has been intentionally left blank.

Table of Contents

List of Figures ix

List of Symbols and Abbreviations xv

Preliminary Remarks 1

1.1 Introduction & Background . . . 1

1.1.1 Challenges With Navier-Stokes Solution . . . 1

1.1.2 External Flow Boundary Layer . . . 2

1.1.3 Blasius Flat Plate Solution . . . 3

1.1.4 Falkner-Skan Pressure Gradient Solution . . . 3

1.1.5 Compressible Flow Solution . . . 4

1.1.6 Numerical Methods . . . 4

1.1.7 Flow Characterization . . . 5

1.1.8 The Problem of Transitional Flow . . . 6

1.2 Literature Review . . . 7

1.3 Project Description . . . 10

1.3.1 Goals and Objectives . . . 11

1.3.2 Intellectual Merit . . . 12

1.4 Research Challenges . . . 12

1.5 Intellectual Contributions of Present Work . . . 13

Mathematical and Numerical Formulation of Laminar Boundary Layers 15

2.1 External Conditions on Boundary Layers . . . 15

2.2 Mathematical Formulation . . . 17

2.2.1 The Incompressible Boundary Layer Equations . . . 18

2.2.2 The Blasius Incompressible Flow Solution . . . 18

2.2.3 The Falkner Skan Incompressible Flow Solution . . . 19

2.2.4 The Energy Equation in Incompressible Flows . . . 20

2.2.5 Blasius Incompressible Flow Finite Difference Transformation . . . 21

2.2.6 Falkner-Skan Laminar Incompressible Flow Finite Difference Transformation . . . 22

2.2.7 Finite Difference Scheme for Thermal Laminar Boundary layers in Incompressible Flows . . . 23
2.2.8 Blasius, Falkner Skan and Energy Similarity Boundary Conditions 24
2.2.9 The Compressible Boundary Layer Equations . . . 29
2.2.10 The Falkner-Skan Compressible Flow Solution . . . 29
2.2.11 The Blasius Compressible Flow Solution for C = 1 . . . 30
2.2.12 Blasius Laminar Compressible Flow Solution for Variable C . . . 32
2.2.13 Boundary Condition Prescription . . . 34

Flow Stability Theory 39
3.1 Stability Theory . . . 39
3.2 Orr-Sommerfeld Equation . . . 40
3.3 Orr-Sommerfeld Equation Numerical Solution . . . 46
3.4 Orr-Sommerfeld Equation Numerical Solution Algorithm . . . 48
3.5 Orr-Sommerfeld Equation Neutral Curves . . . 50
3.6 Compressible Flow Stability . . . 51
3.7 Thermal Orr-Sommerfeld Equation with Variable Flow Properties . . . 52

Incompressible boundary layers subject to wall curvature and passive scalar transport 57
4.1 Curved Surface Boundary Layer Theory . . . 57
4.2 Curved Surface Navier Stokes Equations . . . 59
4.3 Curved Surface Boundary Layer Equations . . . 60
4.4 Curved Surface Boundary Layer Similarity Equations . . . 60
4.5 Boundary Layer Curved Surface Numerical Solution . . . 63
4.6 Curved Surface Boundary Layer Flow Studies . . . 64
4.7 Particular Case: Zero Wall Curvature (Flat Plate) . . . 68
4.8 Chapter 4 Conclusions . . . 74

Unsteady Incompressible Laminar Boundary Layers 75
5.1 Unsteady Laminar Boundary Layer . . . 75
5.2 Unsteady Boundary Layer Governing Equations . . . 76
5.3 Unsteady Boundary Layer Similarity Equations . . . 77
5.4 Unsteady Boundary Layer Similarity Equations Finite Difference Solution 83
5.5 Results and Discussion . . . 85
5.6 Chapter 5 Conclusions . . . 101

Compressible Boundary Layers Subject to Streamwise Pressure Gradient 102
6.1 Compressible Boundary Layers Introduction . . . 102
6.2 Blasius Laminar Compressible Flow Solution . . . 103
6.3 Cohen and Reshotko Compressible Flow Similarity Solution . . . 105
6.4 Compressible Flow Similarity Solution Normalizing Temperature . . . 107
6.5 Compressible Flow with Radiation Similarity Solution . . . 111
6.6 Compressible Boundary Layers Studies . . . 116
6.7 Cohen and Reshotko Compressible Flow Studies . . . 124
6.8 Compressible Flow Similarity Solution Normalizing Temperature Study . 136
6.9 Compressible Flow with Radiation Similarity Solution Study . . . 137
6.10 Chapter 6 Conclusions . . . 146

Stability of Incompressible/Compressible Laminar Boundary Layers 147
7.1 Background . . . 147
7.2 Incompressible Flow Stability Studies . . . 149
7.3 Blasius Compressible Flow Stability Studies . . . 150
7.4 Cohen-Reshotko Flow Stability Studies . . . 154
7.5 Chapter 7 Conclusions . . . 162

Conclusions and Future Work 163
8.1 Final Remarks . . . 163
8.2 Future Work . . . 169

Falkner-Skan and Blasius Algorithms 171
A.0.1 Blasius Incompressible Flow Simulation Code . . . 171
A.0.2 Falkner Skan Incompressible Flow Simulation Code . . . 172
A.0.3 Energy Laminar Incompressible Flow Simulation Code . . . 173
A.0.4 Blasius Laminar Compressible Flow C=1 Simulation Algorithm . 174
A.0.5 Blasius Laminar Compressible Flow for Varialble C Simulation Algorithm . . . 176
A.0.6 Orr-Sommerfeld Equation Numerical Solution Code . . . 178
A.0.7 Falkner Skan equation derivation . . . 181

References 183

List of Figures

Figure 1.1 (a) Hypersonic range and (b) X-51 WaveRider cartoon. Reproduced faithfully from]2(1, 2)(Schmisseur, J. D. 2013). 2
Figure 1.2 Prandtl Boundary Layer Diagram.. 2
Figure 1.3 Region of interest in the present study: laminar stage, flow stability, and transition stage. Adapted from (Cengel, Y. A. and Cimbala, J. M. 2014).. 6
Figure 2.1 (a) Pressure Gradient and (b) Flow Regime diagrams.. 17
Figure 2.2 Blasius incompressible flow simulation flow chart.. 26
Figure 2.3 Falkner-Skan incompressible flow simulation flow chart.. 27
Figure 2.4 Energy equation incompressible flow simulation flow chart.. 28
Figure 2.5 Simulation set up diagram.. 35
Figure 2.6 Blasius compressible flow $C = 1$ simulation flow chart.. 37
Figure 2.7 Blasius compressible flow simulation flow chart for $C \neq 1$.. 38
Figure 3.1 Orr-Sommerfeld incompressible flow simulation flow chart.. 49
Figure 3.2 Typical neutral curve from the Blasius velocity profile.. 50
Figure 3.3 Neutral Stability Curves examples for the first n=1 and second n=2 modes. Reproduced faithfully from (White, F. M. 1991).. 51
Figure 4.1 Curved surface coordinate setup.. 58
Figure 4.2 g Grid dependence test for 1000, 2000, and 4000 grid points, and comparison with White (White, F. M. 1991). For $\beta = 0$, $\Omega = 0$ and Pr = 0.1.. 65
Figure 4.3 f'' (normalized wall shear stress) vs η for $\beta = 1$, 0.2, 0 and -0.1.. . . 66
Figure 4.4 g vs η for $\beta = 0.2$, Ω = -0.1, 0 and -0.1 and Pr=0.1.. 66
Figure 4.5 g vs. η for $\beta = 1$, 0.2, 0 and -0.1, Ω = -0.1 and Pr = 0.1.. 67
Figure 4.6 $g'(0)$ vs Ω for $\beta = 1$, 0.2, 0 and -0.1, Pr = 0.1.. 67
Figure 4.7 g vs η for $\beta = 0.2$, Ω = -0.1 and Pr = 0.1, 0.4, 0.72, 1 and 5.. 68
Figure 4.8 $g'(0)$ vs Pr for $\beta = 0.2$ and Ω = -0.1.. 69
Figure 4.9 f'', f', f vs η comparison with White's data (White, F. M. 1991). . . 70
Figure 4.10 f' vs η comparison with White's data (White, F. M. 1991). 71
Figure 4.11 f'' vs η for β -0.1988 to 1.5.. 71
Figure 4.12 g vs η for β -0.1988 to 1.5.. 72
Figure 4.13 g' vs η for β -0.1988 to 1.5.. 72

Figure 4.14 Effect of pressure gradient on Momentum and Thermal Boundary Layer thickness. 73
Figure 5.1 Matlab code execution time for a zero pressure gradient case at different time τ. 86
Figure 5.2 Present and Analytical Skin Friction Coefficient grid test at different τ for a pressure gradient of 0.5.. 87
Figure 5.3 Non-dimensional free stream function distribution at various dimensionless time numbers τ for the Blasius solution.. 87
Figure 5.4 Non-dimensional velocity function distribution at various dimensionless time numbers τ for the Blasius solution.. 88
Figure 5.5 Dimensionless shear stress function distribution at various dimensionless time numbers τ for a pressure gradient of zero.. 89
Figure 5.6 Non-dimensional stream function distribution at a pressure gradient of -0.18, 0, 0.3333 and 0.5 for a τ of 1.. 89
Figure 5.7 Non-dimensional velocity function distribution at a pressure gradient of -0.18, 0, 0.3333 and 0.5 for a τ of 1.. 90
Figure 5.8 Non-dimensional shear stress function distribution at a pressure gradient of -0.18, 0, 0.3333, and 0.5 for a τ of 1.. 90
Figure 5.9 Present and Analytical Nusselt number grid test at different τ for a pressure gradient of 0.5 for a constant wall temperature.. 91
Figure 5.10 Nusselt number vs τ for Prandtl numbers of 0.1, 0.2, 0.71, 2, 5, and 10 for a pressure gradient of 0.5 at a constant wall temperature condition.. . 92
Figure 5.11 Dimensionless temperature function distribution at various dimensionless time numbers τ for the Blasius Solution at a constant wall temperature.. 92
Figure 5.12 Non-dimensional heat flux function distribution at various dimensionless time numbers τ for a pressure gradient of zero for a constant wall temperature.. 93
Figure 5.13 Dimensionless temperature function distribution at various Prandtl numbers for the Blasius Solution at a constant wall temperature for a τ of 1.. 93
Figure 5.14 Non-dimensional heat flux function distribution at various Prandtl numbers for a pressure gradient of zero at a constant wall temperature with a τ of 1.. 94
Figure 5.15 Dimensionless temperature distribution at pressure gradient of -0.18, 0, 0.3333 and 0.5 for a τ of 1 for a constant wall temperature.. 95

Figure 5.16 Dimensionless heat flux function distribution at pressure gradient of -0.18, 0, 0.3333 and 0.5 for a τ of 1 for a constant wall temperature.. 95
Figure 5.17 Non-dimensional wall temperatures at different τ for a pressure gradient of 0.5 for a constant wall heat flux.. 96
Figure 5.18 Non-dimensional temperature function distribution at various Prandtl numbers for pressure gradient of 0.5 at a constant wall heat flux.. 96
Figure 5.19 Non-dimensional temperature function distribution at various dimensionless time numbers τ for the Blasius solution for a constant wall heat flux.. 97
Figure 5.20 Dimensionless heat flux function distribution at various dimensionless time numbers τ for a pressure gradient of zero for a constant wall heat flux.. 98
Figure 5.21 Dimensionless temperature function distribution at different Prandlt numbers for the Blasius solution at a constant wall heat flux with a τ of 1.. 98
Figure 5.22 Dimensionless heat flux function distribution at different Prandlt numbers for the Blasius Solution at a constant wall heat flux with a τ of 1.. . . . 99
Figure 5.23 Dimensionless temperature distribution at pressure gradient of -0.18, 0, 0.3333 and 0.5 for a τ of 1 for a constant wall heat flux.. 99
Figure 5.24 Heat Flux Function distribution at a pressure gradient of -0.18, 0, 0.3333 and 0.5 for a τ of 1 for a constant wall temperature.. 100
Figure 6.1 f' vs η comparison with White data (White, F. M. 1991) for a number of nodes N of 100, 1000, and 5000 at a Mach number of 5.. 116
Figure 6.2 f' vs η for Mach 2 to 12. 117
Figure 6.3 f'' vs η for Mach 2 to 12. 118
Figure 6.4 g vs. η from Mach 2 to 12. 119
Figure 6.5 g' vs. η from Mach 2 to 12. 119
Figure 6.6 $\eta_{99\%}$ and η_T vs. Mach.. 120
Figure 6.7 f'' vs. η at Mach number at 12 for a Power Law n of 1, 0.76, 0.666.. 120
Figure 6.8 $f''(0)$ vs. Mach 12 for Power Law $n = 1, 0.76, 0.666$.. 121
Figure 6.9 f' vs η for Pr numbers of 2, 1, 0.7, 0.2. 121
Figure 6.10 f'' vs η for Pr numbers of 2, 1, 0.7, 0.2. 122
Figure 6.11 g vs η for Pr numbers of 2, 1, 0.7, 0.2.. 122
Figure 6.12 g' vs η for Pr numbers of 2, 1, 0.7, 0.2.. 123
Figure 6.13 f' vs η comparison with Cohen-Reshotko data (Cohen, C. B. and Reshotcko, E. 1955) a number of nodes N of 100, 1000 and 5000. 124
Figure 6.14 f'' vs η comparison with Cohen-Reshotko (Cohen, C. B. and Reshotcko, E. 1955) data for a number of nodes N of 100, 1000 and 5000. 125

Figure 6.15 g vs η comparison with Cohen-Reshotko (Cohen, C. B. and Reshotcko, E. 1955) data for a number of nodes N of 100, 1000 and 5000. 126
Figure 6.16 $g^{'}$ vs η comparison with Cohen-Reshotko (Cohen, C. B. and Reshotcko, E. 1955) data for a number of nodes N of 100, 1000 and 5000. 127
Figure 6.17 $f^{'}$ vs. η for β of -0.1295 to 2 at g_w of 2 or S_w of 1. 128
Figure 6.18 $f^{''}$ vs. η for β -0.1295 to 2 at a g_w for 2 or S_w of 1. 129
Figure 6.19 g vs. η for β -0.1295 to 2 at a g_w of 2 or S_w of 1 129
Figure 6.20 $g^{'}$ vs. η for β -0.1295 to 2 at g_w of 2 or S_w of 1.. 130
Figure 6.21 Effect of pressure gradient on Momentum and Thermal Boundary Layer thicknesses.. 130
Figure 6.22 $f^{'}$ vs. η at β of -0.1295 for g_w 0 to 2 or S_w from -1 to 1.. 131
Figure 6.23 $f^{''}$ vs. η at β of -0.1295 for g_w from 0 to 2 or S_w from -1 to 1.. 131
Figure 6.24 g vs. η at β of -0.1295 for g_w from 0 to 2 or S_w from -1 to 1.. 132
Figure 6.25 $g^{'}$ vs. η at β of -0.1295 for g_w from 0 to 2 or S_w from -1 to 1.. 132
Figure 6.26 $f_w^{''}$ vs. β for g_w from 2 to 0 or S_w from 1 to -1.. 133
Figure 6.27 $f_w^{''}$ vs. β from -0.5 to 0.1 for g_w from 2 to 0 or S_w from 1 to -1.. 133
Figure 6.28 $g_w^{'}$ vs. β for g_w from 2 to 0 or S_w from 1 to -1.. 134
Figure 6.29 $\eta_{99\%}$ vs. β for g_w from 2 to 0 or S_w from 1 to -1.. 134
Figure 6.30 η_T vs. β for a hot wall condition. 135
Figure 6.31 η_T vs. β for a cold wall condition. 135
Figure 6.32 $f^{'}$ vs. η grid test comparison with Alao and Folarin (Alao, F. I. and Folarin, S. B. 2013). 137
Figure 6.33 g vs. η grid test comparison with Alao and Folarin (Alao, F. I. and Folarin, S. B. 2013). 138
Figure 6.34 $f^{'}$ vs. η for different radiation parameters Q at Mach 0.3 for an adverse pressure gradient of -0.02. 139
Figure 6.35 $f^{'}$ vs. η for different radiation parameters Q at Mach 0.3 for a zero pressure gradient. 140
Figure 6.36 $f^{'}$ vs. η for different radiation parameters Q at Mach 0.3 for a favorable pressure gradient of one. 140
Figure 6.37 $f^{''}$ vs. η for different radiation parameters Q at Mach 0.3 for an adverse pressure gradient of -0.02. 141
Figure 6.38 $f^{''}$ vs. η for different radiation parameters Q at Mach 0.3 for a zero pressure gradient. 141

Figure 6.39 f'' vs. η for different radiation parameters Q at Mach 0.3 for a favorable pressure gradient of 0.2. 142
Figure 6.40 g vs. η for different radiation parameters Q at Mach 0.3 for an adverse pressure gradient of -0.02. 142
Figure 6.41 g vs. η for different radiation parameters Q at Mach 0.3 for a zero pressure gradient. 143
Figure 6.42 g vs. η for different radiation parameters Q at Mach 0.3 for a favorable pressure gradient of 0.02. 143
Figure 6.43 g' vs. η for different radiation parameters Q at Mach 0.3 for an adverse pressure gradient of -0.02. 144
Figure 6.44 g' vs. η for different radiation parameters Q at Mach 0.3 for a zero pressure gradient. 144
Figure 6.45 g' vs. η for different radiation parameters Q at Mach 0.3 for a favorable pressure gradient of 0.02. 145
Figure 7.1 Blaisus incompressible flow stability verification using the momentum boundary layer thickness coordinate. 150
Figure 7.2 Blaisus incompressible flow stability verification using the displacement thickness coordinate. 151
Figure 7.3 Falkner-Skan incompressible flow stability for different pressure gradients using the momentum boundary layer thickness coordinate. 152
Figure 7.4 Falkner-Skan incompressible flow $(Re_{cr})_{\eta_{99.9\%}}$ vs β comparison with trendline using the momentum boundary layer thickness coordinate. 153
Figure 7.5 Falkner-Skan incompressible flow stability for different pressure gradients using the displacement thickness coordinate. 154
Figure 7.6 Falkner-Skan incompressible flow $(Re_{cr})_{\eta^*}$ vs β comparison with trendline and Wazzan *et. al.* (Wazzan, A. R., Okamura, T. T. and Smith, A. M. O. 1968) data using the displacement thickness coordinate. 155
Figure 7.7 Blasius stability for compressible flow at different Mach numbers based on the momentum boundary layer thickness coordinate. 156
Figure 7.8 Blasius stability compressible flow $(Re_{cr})_{\eta_{99.9\%}}$ vs Mach comparison with trendline based on the momentum boundary layer thickness coordinate. 157
Figure 7.9 Blaisus stability for compressible flow for different Prandlt numbers at Mach 5 based on the momentum boundary layer thickness coordinate. . . 157

Figure 7.10 Blaisus Stability compressible flow $(Re_{cr})_{\eta_{99.9\%}}$ vs Prandlt number at Mach 5 present result comparison with trendline approximation based on the momentum boundary layer thickness coordinate. 158
Figure 7.11 Blasius stability for compressible flow for different Power Law n at Mach 5 using the momentum boundary layer thickness coordinate. 158
Figure 7.12 Blasius Stability compressible flow $(Re_{cr})_{\eta_{99.9\%}}$ vs Power Law n at Mach 5 present result comparison with trendline approximation based on the momentum boundary layer thickness coordinate. 159
Figure 7.13 Cohen-Reshotko flow stability for different pressure gradients using the momentum boundary layer thickness coordinate. 159
Figure 7.14 Cohen-Reshotko flow $(Re_{cr})_{\eta_{99.9\%}}$ vs β comparison with trendline using the momentum boundary layer thickness coordinate. 160
Figure 7.15 Cohen-Reshotko flow stability for different wall temperatures using the momentum boundary layer thickness coordinate. 160
Figure 7.16 Cohen-Reshotko flow stability $(Re_{cr})_{\eta_{99.9\%}}$ vs wall temperature comparison with trendline using the momentum boundary layer thickness coordinate. 161

List of Symbols and Abbreviations

u	Velocity component parallel to the wall (m/s)
v	Velocity component perpendicular to the wall (m/s)
x	Coordinate parallel to the wall (m)
y	Coordinate perpendicular to the wall (m)
ν	Kinematic viscocity (m^2/s)
T	Temperature (K)
k	Thermal conductivity $(W/m * K)$
C_p	Specific heat at constant pressure $(J/kg * K)$
U	Velocity at boundary layer edge (m/s)
f	Variable associated to the stream function (-)
$f^{'}$	Variable associated to the velocity (-)
$f^{''}$	Variable associated to the shear stress (-)
η	Similarity variable (-)
$\delta_{99\%}$	Momentum boundary layer thickness (m)
m	Falkner-Skan power parameter (-)
β	Falkner-Skan pressure gradient (-)
C_f	Skin friction coefficient (-)
ρ	Density (kg/m^3)
τ_w	Wall shear stress (N/m^2)
g	Variable associated with temperature (-)
$g^{'}$	Variable associated with heat flux (-)
Pr	Prandlt number (-)

T_e	Temperature at the boundary layer edge (K)
T_w	Temperature at the wall (K)
$\Delta\eta$	Node spacing (-)
N	Total number of nodes (-)
P_e	Pressure at the boundary layer edge (Pa)
μ	Dynamic viscosity $(Pa * s)$
h	Enthalpy (J/kg)
ξ	Dimensionless variable (-)
ρ_e	Density at the boundary layer edge (kg/m^3)
μ_e	Dynamic viscosity at the boundary layer edge $(Pa * s)$
U_e	Velocity component parallel to the wall at the boundary layer edge (m/s)
Ma_e	Mach number at the boundary layer edge (-)
γ	Specific heat ratio (-)
n	Power law parameter (-)
g_w	Variable associated to the wall temperature (-)
P	Pressure (Pa)
U_0	Velocity component in x direction (m/s)
V_0	Velocity component in y direction (m/s)
P_0	Pressure (Pa)
$\hat{u}$	Velocity x component disturbance (m/s)
$\hat{v}$	Velocity y component disturbance (m/s)
$\hat{P}$	Pressure disturbance (Pa)
t	time (s)
α	Wave number $(1/m)$
c	Propagation speed (m/s)

$\bar{u}$	Complex amplitude of $\hat{u}$ (m)
$\bar{v}$	Complex amplitude of $\hat{v}$ (m)
$\bar{P}$	Complex amplitude of $\hat{P}$ (m)
Re	Reynolds number (-)
Φ	Viscous dissipation term (m^2/s^2)
μ_{ref}	Reference dynamic viscosity $(Pa * s)$
T_{ref}	Reference temperature (K)
Λ	Surface curvature $(1/m)$
Ω	Variable asociated to the surface curvature (-)
Δ^*	Non-dimensional displacement thickness (-)
θ^*	Non-dimensional Momentum thickness (-)
H	Shape factor (-)
τ	Dimensionless time (-)
Nu	Nusselt number (-)
S	Stagnation enthalpy (-)
S_w	Stagnation enthalpy at the wall (-)
$\eta_{99.9\%}$	Momentum Boundary layer thickness (-)
η^*	Non-dimensional displacement thickness (-)
η_T	Thermal boundary layer thickness (-)
$(Re_{cr})_{\eta_{99.9\%}}$	Critical Reynolds based on the momentum boundary layer thickness coordinate (-)
$(Re_{cr})_{\eta^*}$	Critical Reynolds based on the displacement boundary layer thickness coordinate (-)
$Re_{\eta_{99.9\%}}$	Reynolds coordinate based on the momentum boundary layer thickness coordinate (-)
Re_{η^*}	Reynolds coordinate based on the displacement boundary layer thickness coordinate (-)

$\alpha_{\eta_{99.9\%}}$	α coordinate based on the momentum boundary layer thickness coordinate (-)
α_{η^*}	α coordinate based on the displacement boundary layer thickness coordinate (-)

Chapter 1
Preliminary Remarks

1.1 Introduction & Background

New technologies always require new tactics for their understanding. As technology progresses, the fluid flow speed increases, and issues associated with compressibility emerge (i.e., large variations in density with respect to pressure). It is clear that supersonic-hypersonic capabilities would provide faster response and longer-range coverage to military aircraft systems. For example, vehicles moving at speeds five times higher than the sound speed might reach the U.S. west coast from the east coast of the U.S. in roughly 23 minutes, as seen in Figure 1.1. Thus, the obtained knowledge of the physics behind high-speed aerodynamics can lead to the development of more efficient control techniques for the fluid flow (e.g., wave drag reduction) and aerodynamic heating in high-speed vehicle design. Therefore, new methods and studies are required to solve these issues. An important aspect to start solving this problem is the fluid motion characterization via the Navier-Stokes equations for compressible flow in aerodynamic high-speeds.

1.1.1 Challenges With Navier-Stokes Solution

The Navier-Stokes (NS) equations are the basis of fluid mechanics theory. The Clay Mathematics Institute (Clay Mathematics Institute) has called the analytical solution in three-dimensions of NS equations one of the seven most important open problems in mathematics. There are few analytical or semi-analytical solutions for these equations for external or internal flows due to its complexity, non-linearity, and three-dimensionality. These solutions are achieved by applying certain assumptions to eliminate terms from the NS equation, reducing its complexity. Numerically, NS can be completely solved for a given initial and boundary conditions to study the fluid dynamics. This work focuses on the external flow boundary layer solution.

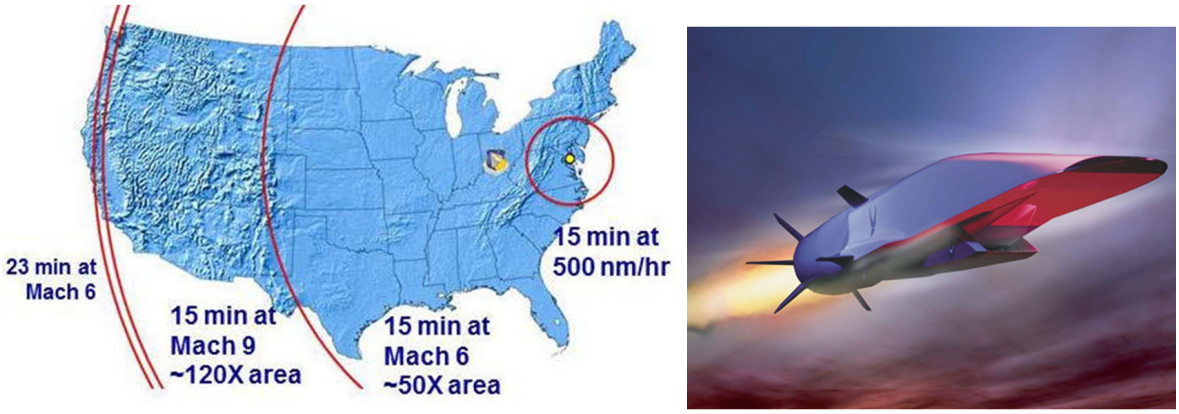

(a) (b)

Figure 1.1: (a) Hypersonic range and (b) X-51 WaveRider cartoon. Reproduced faithfully from (Schmisseur, J. D. 2013)

1.1.2 External Flow Boundary Layer

Prandtl(Cengel, Y. A. and Cimbala, J. M. 2014; Tani 1977) solved the NS for an external flow by dividing the flow into two regions separated by a boundary layer. As seen in Figure 1.2, these regions are classified as a region near the wall or the boundary layer where the viscosity effects are important, and a further wall or inviscid region where the viscosity effects are practically negligible.

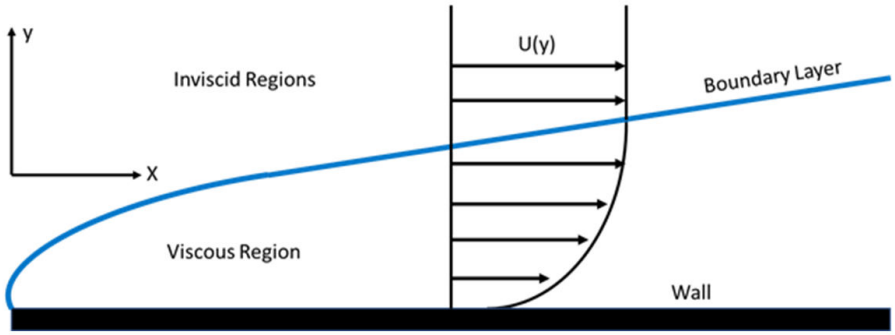

Figure 1.2: Prandtl Boundary Layer Diagram.

Prandtl simplify the NS equations by assuming (Cengel, Y. A. and Ghajar, A. J. 2015):

• That the velocity component parallel to the wall is much larger than the velocity component perpendicular to the wall.

• Steady State condition. No changes in time.

• The velocity component parallel to the wall varies greatly in the direction perpendicular to the wall compared to the direction parallel.

• The heat transfer occurs in the direction perpendicular to the wall.

• Gravity effects are negligible, thus, the variation of the pressure perpendicular to the wall is negligible.

1.1.3 Blasius Flat Plate Solution

Blasius (Cengel, Y. A. and Ghajar, A. J. 2015; White, F. M. 1991; Blasius, H. 1908) developed a solution to the boundary layer equations by introducing the concept of similarity. A similarity solution reduces partial differential equations to an ordinary differential equation with a smaller number of independent variables. Blasius achieved similarity by grouping the parallel and perpendicular coordinates of the wall into a single similarity variable η. Also, it is important to mention that in the Blasius solution, the change in pressure in the direction parallel to the wall is zero.

1.1.4 Falkner-Skan Pressure Gradient Solution

Falkner and Skan (White, F. M. 1991; Falkner, V. M. and Skan, S. W. 1930) introduced the streamwise pressure gradient concept to give a more general solution for wedges and constant pressure gradient situations (Blasius solution). The Falkner-Skan solutions (Falkner, V. M. and Skan, S. W. 1930) form a family of similarity solutions to the Prandtl boundary layer equations, where the freestream velocity, U_∞, vary as a power law, m, of the streamwise coordinate, i.e. $\sim x^m$. These solutions describe steady, two-dimensional, laminar boundary layer flow over a wedge. Falkner-Skan stated that these solutions can be of three types: Favorable Pressure Gradient (flow acceleration), Zero Pressure Gradient (Blasius Solution), and Adverse Pressure Gradient (flow deceleration).

1.1.5 Compressible Flow Solution

When the flow velocity exceeds Mach 0.3, compressibility effects (variations of fluid density with pressure variations are no longer negligible) must be considered, with particular significance in high-speed flows beyond Mach 5, which falls within the hypersonic regime. In these high-speed flows, thermodynamic variations in density, viscosity, thermal conductivity, pressure, and temperature must be incorporated into the Falkner-Skan solutions. This is accomplished by coupling the momentum and energy equations to account for temperature variations, while simultaneously introducing an equation of state, such as the perfect gas law or power law, to characterize the fluid properties, including density, viscosity, and thermal conductivity. It is essential to note that the boundary layer assumptions originally employed by Prandtl to reduce the Navier-Stokes equations must be maintained for the current analysis. To simplify the compressible boundary layer equations, a similarity solution analogous to those developed by Blasius and Falkner-Skan is utilized. Illingworth demonstrated that similarity is achieved by transforming the parallel and perpendicular wall coordinates into two similarity variables: ξ, which accounts for the viscosity effects, and η, which incorporates the effects of density (White, F. M. 1991).

1.1.6 Numerical Methods

The final equations derived from the Blasius, Falkner-Skan, and compressible flow analyses can be employed to determine key quantities such as boundary layer thickness, the skin friction coefficient, and the local streamwise and wall-normal velocity components, typically through numerical methods. A differential equation represents a function that incorporates partial derivatives with respect to various variables. While many differential equations can be solved analytically across the entire domain, certain equations, such as the non-linear Navier-Stokes (NS) equations, cannot be solved in a closed-form expression. In these cases, numerical techniques are utilized to approximate solutions at discrete points in the domain, referred to as nodes. The primary approach is to increase the number of nodes (and spatial resolution) such that their density becomes sufficiently high, making the numerical solution converge to the analytical solution with high accuracy.

Generally speaking, there are two types of numerical problems:

• Initial Conditions problems: in which the problem initial state or the first node is known.

• Boundary Conditions problems: it involves solving a differential equation (or system of equations) with conditions specified on the solution and/or its derivatives at the boundaries of a domain.

Numerous methods are employed to solve differential equations numerically (Zill, D. and Warren, W. 2013), including the Runge-Kutta Third or Fourth-Order and Forward Euler methods, which are typically utilized for initial value problems where the initial condition is provided. Additionally, Finite Difference Methods (FDM) are employed for boundary value problems, where the conditions at the boundary nodes of the domain are specified.

1.1.7 Flow Characterization

The external or internal fluid flow regions are classified according to the Reynolds number (Re number). The Re number is a dimensionless number that describes the ratio between inertia to viscous flow forces (Cengel, Y. A. and Cimbala, J. M. 2014; Cengel, Y. A. and Ghajar, A. J. 2015; Tennekes, H. and Lumley, J. M. 1972). Figure 1.3 shows the three regions of fluid motion for an external flow that are classified according to the Reynolds number:

• Laminar flow: This flow region is characterized by an orderly flow movement due to the fact that viscous forces dominate over inertia forces. In the laminar section, the mass, momentum, and energy are transported among streamlines in an orderly manner by molecular diffusion.

• Transitional flow: This flow region is characterized by a mixture of laminar and turbulent flow. In this region, the flow changes from laminar to turbulent. Since the transitional flow is neither laminar nor turbulent, it is very hard to study, and in many cases, it is not very well understood.

• Turbulent flow: This flow region is characterized by a chaotic flow movement due to the fact that inertial forces dominate over viscous forces. In addition, turbulence is characterized by disorderly and rapid fluctuations called eddies, which transport energy, momentum, and mass more rapidly than molecular diffusion, greatly enhancing them.

1.1.8 The Problem of Transitional Flow

As previously discussed, fluid flow regimes are often classified based on their Reynolds number. For external flows, it is conventionally assumed that when the Reynolds number exceeds 5×10^5 (the critical Reynolds number), the flow transitions from laminar to turbulent. Conversely, flows with Reynolds numbers lower than this threshold are considered laminar. However, this classification serves primarily as an engineering approximation intended to simplify the analysis of external flow problems, as the transitional region is typically very narrow. In reality, the critical Reynolds number at which the flow transitions from laminar to a transitional regime is lower than 5×10^5 (instability flow point). To determine this transition more accurately, a linear stability analysis is conducted. It is important to note that this analysis does not predict the onset of turbulence directly, as turbulence itself is an experimentally observed phenomenon. Instead, empirical correlations are employed to predict the onset of turbulence under various conditions. Despite significant research efforts, the phenomenon of transition remains incompletely understood.

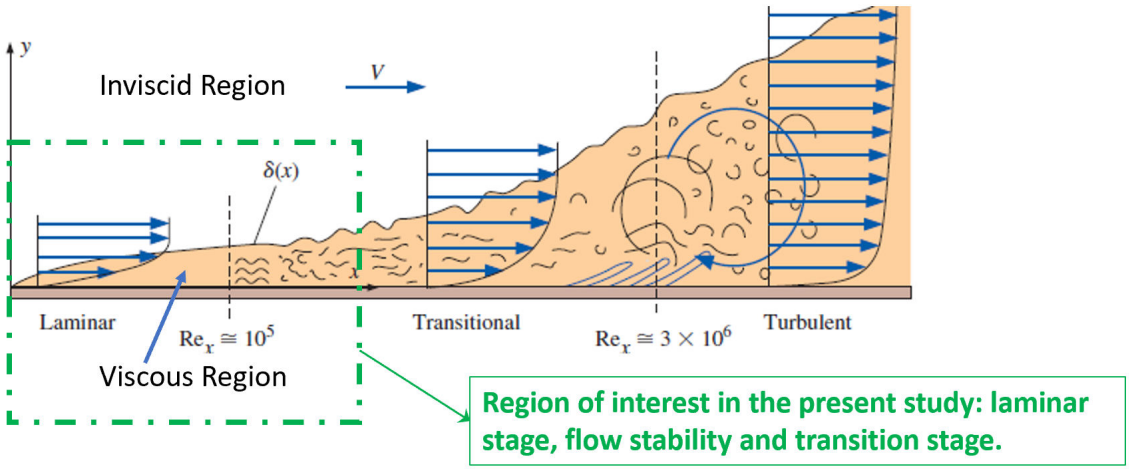

Figure 1.3: Region of interest in the present study: laminar stage, flow stability, and transition stage. Adapted from (Cengel, Y. A. and Cimbala, J. M. 2014).

1.2 Literature Review

Han (Han, S. 2013) developed a finite difference solution to the Falkner-Skan equations by decomposing the third-order differential equation into two ordinary differential equations—one of first order and the other of second order. Han's method offers a means to solve the Falkner-Skan equations without the need for the multiple iterations characteristic of shooting methods. Kaups et al. (Kaups, K. and Smith, A. M. O. 1967) proposed a method for accurately calculating the laminar boundary layer of a liquid with variable fluid properties. They observed that, in contrast to gases, viscosity in liquids decreases with increasing temperature. Kaups et al. (Kaups, K. and Smith, A. M. O. 1967) further concluded that from the perspective of boundary layer stability, surface cooling by mass transfer does not offer advantages. This is due to the destabilizing effect of mass ejection and the cold wall, which causes the boundary layer to separate. Additionally, Kaups et al. (Kaups, K. and Smith, A. M. O. 1967) found that heating combined with blowing is more effective than heating alone, as it results in deeper thermal penetration into the boundary layer. They also noted that, according to inviscid stability theory, heating eliminates the inflection point from the velocity profiles, thereby enhancing stability. Cohen and Reshotko et al. (Cohen, C. B. and Reshotcko, E. 1955) applied the Stewarson transformation to the laminar compressible boundary layer equations and introduced a similarity analysis that allowed for their reduction to a set of ordinary differential equations. Their analysis was based on several assumptions: a Prandtl number of unity, linear viscosity-temperature relationships across the boundary layer, an isothermal surface, and a specific free-stream velocity distribution consistent with similar solutions. Cohen and Reshotko (Cohen, C. B. and Reshotcko, E. 1955) emphasized that the development of the boundary layer is influenced by the pressure gradient, Mach number, heat transfer, and the properties of the fluid in question. They concluded that for favorable pressure gradients, a unique solution exists, while for adverse pressure gradients, two solutions are obtained—one viscous and the other inviscid. Moreover, Cohen and Reshotko (Cohen, C. B. and Reshotcko, E. 1955) found that for a Prandtl number equal to one, the thermal boundary layer is thicker than the dynamic boundary layer under favorable pressure gradients. Recently, Ramirez and Araya (Ramirez, M. A. and Araya, G. 2020) developed a numerical shooting algorithm for solving incompressible and compressible laminar Falkner-Skan flows. Compressibility effects in adiabatic walls have been identified as a local increase of the streamwise velocity U as the Mach number increases for the same normalized wall-normal coordinate. Although the hydrodynamic boundary layer exhibits a strong shrinking process in the hypersonic regime, the thermal boundary layer grows. Lipatov and Ngo (Lipatov, I. I. and Ngo, K. T. 2020) proposed a solution of the Falkner-Skan equation for a hypersonic flow past a flat plate by assuming: large Mach numbers,

a weak regime of hypersonic interaction, that the gas is thermodynamically perfect and characterized by a specific heat ratio, and finally, that the dynamic viscosity is a linear function of temperature. Lipatov and Ngo (Lipatov, I. I. and Ngo, K. T. 2020) found that the presence of heat transfer delays the appearance of separation and that a decrease in temperature leads to a decrease in the critical value of the pressure gradient at which the friction on the surface vanishes.

Murphy (Murphy, J. S. 1965) investigated the effects of surface curvature on the laminar boundary layer flow for both large and moderate wall curvatures under streamwise pressure gradient conditions. He concluded that, for equivalent Reynolds numbers, the shear stresses on convex surfaces are lower than those on concave and flat surfaces. Furthermore, Murphy observed that the smooth transition from viscous flow to outer flow causes the velocity profile to exhibit a negative slope near the outer edge for the convex case, whereas it shows a positive slope for the concave case. Ozgen (Ozgen, S.) highlighted that hydrodynamic stability is one of the most critical yet least understood areas within fluid mechanics. Ozgen emphasized that the primary focus of hydrodynamic stability is to investigate the breakdown of laminar flows and their eventual transition to turbulence. He further asserted that this theory has wide-ranging applications, such as in flow control for the wings of large transport aircraft to improve fuel efficiency, predicting the transition location on airfoils, blade cooling in turbomachinery, and optimizing jet flows for more efficient combustion in gas turbines and internal combustion engines. In his work, Ozgen established that Tollmien-Schlichting waves represent the initial stage of transition and that linear stability theory is applicable to this first stage. Ozgen concluded that for favorable pressure gradients, the flow stabilizes, and the flow wedge angle decreases, thereby reducing the influence of the pressure gradient on stability.

Wazzan et al. (Wazzan, A. R., Okamura, T. T. and Smith, A. M. O. 1968) presented a comprehensive set of spatial and temporal stability charts for the incompressible flow of the Falkner-Skan boundary layer, spanning pressure gradients ranging from -0.1988 to 1. In their work, Wazzan et al. normalized the Orr-Sommerfeld equation coordinates with respect to displacement thickness, rather than boundary layer thickness. This modification allowed for more accurate characterization of the stability behavior across a range of pressure gradients. Ozgen (Ozgen, S. 2004) conducted a numerical study on the stability and transitional effects of boundary layers with heated walls by modifying the incompressible stability equations to incorporate temperature-dependent fluid properties. Ozgen noted several practical applications of this theory, such as in the airflow over overheated aircraft wings to prevent icing, fluid flows over heat exchangers, and related phenomena. In his analysis, Ozgen found that both heating and cooling significantly modify the velocity boundary layer profile, and that heat transfer plays a considerable

role in affecting the stability characteristics of the flow. His findings concluded that heating stabilizes water flows while destabilizing air flows, and that the velocity profile of the boundary layer exerts a strong influence on stability and transition behavior. Furthermore, Ozgen observed that variable viscosity has a pronounced effect on the stability of both air and water flows, with density having a significant impact on airflow stability but a negligible effect on water flow stability.

Wazzan et al. (Wazzan, A. R., Okamura, T. and Smith, A. M. O. 1968) investigated the stability of water boundary layer flow over a flat plate with heated and cooled walls by extending the Orr-Sommerfeld solution to incorporate fluid-dependent properties. They identified several factors that influence stability, including the shape of the boundary layer velocity profile, the pressure gradient, the Reynolds number, and the wave number or frequency of the disturbance. Wazzan et al. concluded that heating the water boundary layer flow has a stabilizing effect, while heating the air boundary layer flow destabilizes it. This is attributed to the fact that the viscosity of water decreases with increasing temperature, whereas the viscosity of air increases with temperature. Ozgen and Kirach (Ozgen, S. and Kircah, S. A. 2008) explored the stability of compressible flat plate boundary layers under adiabatic wall conditions using linear stability theory. They assumed that all fluid properties, including the Prandtl number, are temperature-dependent. Their analysis revealed that once the flow becomes supersonic, a second mode, or Mack mode, emerges in addition to the first mode. They found that the second mode stabilizes as the wave angle increases, and that the reference temperature can determine the stability of the inviscid second mode at high Mach numbers. Furthermore, Ozgen and Kirach concluded that for oblique waves with Mach numbers ranging from 4 to 10, the stability characteristics remain almost unchanged for a constant wave orientation.

Malik (Malik 1989) investigated the application of compressible linear stability theory to predict boundary layer transition at supersonic and hypersonic speeds. For cold walls, he found that the two-dimensional second mode predominantly governs the transition process at lower hypersonic Mach numbers. Malik also noted that a favorable pressure gradient could be utilized to stabilize this second mode, offering potential control over transition behavior. Zurigat et al. (Zurigat, Y. H., Nayfeh, A. H. and Masad, J. A. 1992) explored the influence of pressure gradients on the stability of compressible boundary layers at Mach numbers up to 8 with adiabatic walls, using small-disturbance compressible stability theory. Their study concluded that the second Mack mode waves are stabilized by favorable pressure gradients and destabilized by adverse pressure gradients. This highlights the significant role that pressure gradients play in modulating

the stability characteristics of high-speed compressible boundary layers. Simpson (Simpson, C. 2015b) developed a MATLAB code to solve the temporal or spatial solutions of the Orr-Sommerfeld equation using a finite difference scheme. This approach provides a numerical method for analyzing the stability of boundary layer flows by discretizing the equation and solving it for the desired stability modes, offering an efficient tool for studying flow stability in various contexts.

In summary, the literature review performed has revealed the importance of an accurate understanding of the transport phenomena inside laminar high-speed boundary layers for an efficient aerodynamic and thermal design of hypersonic vehicles. *As a consequence, the proposed body of work makes an effort to achieve a better understanding of external conditions (i.e., compressibility, streamwise/streamline pressure gradient, viscosity-law effects, radiation) on the stability of laminar high-speed flows. To our knowledge, such an extensive analysis has not previously been performed.*

1.3 Project Description

To investigate the onset of the transitional flow region, a linear stability analysis is applied to the Navier-Stokes (NS) equations, leading to the derivation of the Orr-Sommerfeld equations. This analysis is typically carried out through the following steps (White, F. M. 1991):

- Select the basic flow solution (NS).
- Add a disturbance.
- Find the disturbance equations.
- Linearize.
- Simplify (Traveling wave assumption).
- Solve for the eigenvalues.
- Interpret the neutral stability curves.

Compressible flows introduce additional complexity to the stability problem because the pressure is coupled with density and temperature through the equations of state. In incompressible flows, the fluctuations considered are typically the velocities in the x, y,

and x directions, as well as the pressure. However, in compressible flows, fluctuations in density and temperature must also be incorporated into the analysis, considering the variations in fluid transport properties. This extended analysis results in a sixth-order differential equation, which is then solved as an eigenvalue problem. To simplify the stability analysis of compressible flows, a modified version of the Orr-Sommerfeld equation is employed, adjusted to account for changes in viscosity due to temperature and density variations.

1.3.1 Goals and Objectives

The objectives of the proposed work are summarized as follows:

• To accurately model the Boundary Layer and Energy equations based on the Blasius and Falkner-Skan similarity solution for non-reacting laminar incompressible/compressible boundary layers using a Finite Difference scheme.

• To numerically solve the Orr-Sommerfeld and thermal Orr-Sommerfeld equations using a Finite Difference scheme in the flow stability analysis of high-speed flows.

• To evaluate the external effects of different streamwise pressure gradients, Mach numbers, viscosity laws, wall thermal conditions (cold, adiabatic, and hot wall thermal conditions), different Prandtl numbers of the fluid, wall curvature (concave and convex surface curvatures), and radiation heat transfer on the boundary layer parameters and flow stability.

Some research questions to be addressed in this study are:
i) Is there any strong influence of the pressure gradient in the boundary layer thickness?
ii) What is the compressibility effect on the wall shear stress and heat fluxes?
iii) What is the impact of the Prandtl number on viscous dissipation at high Mach numbers?
iv) Does the cold wall condition have a stabilizing or destabilizing effect on flow stability?
v) Does radiative heat transfer significantly influence momentum transport?

1.3.2 Intellectual Merit

This study aims to solve the laminar Boundary Layer equations using the similarity Falkner-Skan equations for compressible flow, incorporating various spatial-velocity scale transformations. A finite difference scheme will be employed to solve the equations, circumventing the need for the shooting method. The focus of this work is on the laminar and transitional flow regimes. The results will be utilized to investigate transition effects through stability analysis. Additionally, a comprehensive parametric study will be conducted to examine the combined effects of pressure gradient, Mach number, viscosity law, Prandtl number, and wall thermal conditions on laminar hypersonic boundary layers and their implications for flow stability. Furthermore, an in-house flow solver has been developed for this analysis within a MATLAB environment, and the resulting code will be made available to the fluid dynamics community upon request.

1.4 Research Challenges

The Blasius and Falkner-Skan (FS) equations, which describe non-linear similarity solutions to the Boundary Layer equations, are applicable to both compressible and incompressible flows. The similarity solutions for the velocity and thermal fields are governed by third-order and second-order differential equations (ODE), respectively, for a flat surface. When these equations are applied to curved walls, they yield a fourth-order differential equation. These problems are typically solved in one dimension using a Runge-Kutta fourth-order method (Zill, D. and Warren, W. 2013) in combination with a shooting method algorithm to estimate the wall shear stress. The complexity of the shooting method lies in the necessity of having an initial guess for the wall shear stress, or some bounds (e.g., using methods such as Newton-Raphson or Regula-Falsi), to iterate towards the correct value.

In contrast, by reformulating the equations in terms of $f^{'}$ and f, the problem reduces to a set of first and second-order differential equations. These can be solved for $f^{'}$ and f using a Finite Difference method combined with a modified Forward Euler scheme. This approach bypasses the difficulties associated with the shooting method, as the boundary conditions for $f^{'}$ and the initial conditions for f are known a priori. Fluid flow is generally categorized into three phases: laminar, transitional, and turbulent. In laminar flow, the fluid moves in a smooth, orderly manner, while in turbulent flow, it exhibits chaotic behavior due to vortex formations. The transitional phase, however, is characterized by

a mix of both laminar and turbulent behaviors, making it difficult to classify as either. This phase presents a significant challenge in fluid dynamics. One approach to studying its effects and potentially extending laminar flow is through stability analysis. In stability analysis, a disturbance is introduced to the Navier-Stokes equations in the form of a wave, allowing for the examination of the equations' stability and providing insights into the precise location where the flow transitions from laminar to transitional, driven by inherent flow instabilities in space or time. Solving the Orr-Sommerfeld problem in compressible flows is particularly challenging due to the added complexity of the governing equations, which must account for density variations and thermodynamic effects—factors not present in the simpler incompressible flow case, not to mention the strong influence of wall thermal conditions (cold, adiabatic, and hot wall conditions) on high-speed flows.

1.5 Intellectual Contributions of Present Work

This work describes a method for solving the The Blasius, Falkner-Skan, and Cohen & Reshotko similarity equations are solved using an innovative finite difference scheme, which eliminates the need for the tedious iterations typically required by the shooting method. The solution methodology employed for these equations follows a similar approach to that presented in (Han, S. 2013), with the key distinction that (Han, S. 2013) addressed the incompressible Falkner-Skan equation using an implicit finite difference scheme. In this work, the finite difference solutions were extended to solve not only the incompressible flow similarity equations but also to solve compressible flow similarity equations by using an explicit finite difference scheme, which opens these types of codes to further future optimization and parallelization. Additionally, it could be said that this work could be the initial step in building similarity solvers that do not require guesses or shooting techniques.

The influence of various external flow conditions, including pressure gradients, Mach numbers, viscosity laws, wall temperature, Prandtl numbers, wall curvature, and radiation heat transfer, on the dynamics and stability of the laminar boundary layer has been systematically investigated. These comprehensive studies provide crucial insights into the flow behavior and underlying complexities, thereby enhancing the understanding necessary for advancing future projects in fluid mechanics. Such investigations offer valuable guidance on how to strategically manipulate these parameters to optimize design considerations, particularly in the context of aerodynamic vehicle performance and design.

In the literature review of this work, stability analysis was conducted on laminar compressible flow under the assumption of a zero pressure gradient. In contrast, the present study extends this analysis by considering a Cohen-Reshotko velocity profile, accounting not only for the effects of wall temperature but also for the influence of the pressure gradient. A significant aspect of this work is the investigation of the critical Reynolds number, which governs the transition from laminar to turbulent flow. The study explores how this critical Reynolds number is affected by variations in the pressure gradient, Prandtl number, power-law exponent n, Mach number, and wall temperature. Additionally, trendline equations were derived to approximate the critical Reynolds number as a function of these external parameters, providing a framework for future stability analyses. To the best of our knowledge, this comprehensive approach has not been previously explored in the literature.

Furthermore, the MATLAB code developed in this work was extended to solve the thermal Orr-Sommerfeld equation (temporal solution) for a variable-property flow. This extension enhances the program's versatility, enabling it to address more realistic flow scenarios that involve heat transfer, where the energy equations are coupled with the momentum equations.

In summary, this thesis makes the following contributions to the field of fluid dynamics and numerical methods: 1) It develops an explicit finite difference solver for both incompressible and compressible similarity flows, providing a foundational step towards the creation of more efficient algorithms capable of solving these equations without the reliance on the shooting method; 2) It conducts a comprehensive analysis of the effects of external conditions on flow dynamics and stability, with implications for the optimization of vehicle design; 3) It performs a stability analysis of an APG flow at varying wall temperatures (Cohen-Reshotko profile), offering deeper insights into the mechanisms for extending the laminar flow regime and delaying transition; and 4) It derives trendline approximations to facilitate the computation of the critical Reynolds number for various flow conditions, thereby enabling faster and more efficient calculations in future studies.

Chapter 2
Mathematical and Numerical Formulation of Laminar Boundary Layers

2.1 External Conditions on Boundary Layers

A flow can be categorized as either incompressible or compressible based on the extent of density variation in response to pressure changes within the fluid flow (Cengel, Y. A. and Cimbala, J. M. 2014). Specifically, a flow is deemed incompressible if the density variations with respect to pressure fluctuations are negligible (i.e., $\partial\rho/\partial p \approx 0$). Conversely, it is considered compressible when density undergoes significant variations. In the context of high-speed vehicular motion, the flow is typically characterized using the Mach number, which is defined as the ratio of the flow velocity to the local speed of sound. The speed of sound, representing the propagation velocity of an infinitesimal pressure wave induced by a slight disturbance within a medium, is typically approximated as 346 m/s at sea level. However, a more accurate determination of the speed of sound requires calculating the square root of the product of the specific heat ratio, the universal gas constant, and the absolute temperature in a perfect gas. For air (the working fluid in this study), compressibility effects become notably significant at Mach numbers exceeding 0.3, as depicted in Figure 2.1 (a). It is crucial to highlight that the compressibility of a flow does not necessitate a high flow velocity per se; it can be influenced by variations in thermodynamic properties that affect the calculation of the speed of sound. In the regime of compressible flow, the critical Mach number corresponds to the surface point where the Mach number attains a value of unity (the sonic condition). As the flow progresses along a surface, it initially behaves as subsonic ($0.3 < \text{Mach} < M_{critical}$), transitions into a transonic state ($M_{critical} \leq \text{Mach} < 1.2$), becomes fully supersonic for Mach numbers exceeding 1.2, and ultimately reaches a hypersonic regime at Mach numbers greater than 5. The concept of the critical Mach number is defined as the freestream Mach number

at which the flow begins to exhibit sonic velocities at any point within the system. This threshold represents the onset of compressibility effects, where localized regions within the flow transition to Mach 1 (sonic conditions), marking the transition from subsonic to transonic flow behavior. The three primary categories of streamwise pressure gradients, commonly encountered in wall-bounded flows (either in isolation or in combination), are illustrated in Figure 2.1 (b).

• Zero Pressure Gradient (ZPG): the pressure variation along the flow direction is negligible. The classical example is flow over a thin flat plate.

• Favorable Pressure Gradient (FPG): in this case, there is said to be a flow acceleration that causes an increase in the flow speed and a decrease in pressure. Since the flow is in an accelerating condition and the speed increases, the boundary layer becomes thinner and closer to the surface, decreasing the probability of flow separation.

• Adverse Pressure Gradient (APG): it means that there is a prescribed deceleration that slows the flow as the pressure increases. This is an undesirable condition, because as the velocity decreases, the boundary layer becomes thicker and gets farther from the wall, which may lead to flow separation. It is important to mention that the boundary layer equations are based on parabolic conditions, and if flow separation occurs, this could lead to a reverse backflow where the boundary layer equations cannot be applied.

Furthermore, in all cases, the pressure remains approximately constant normal to the surface inside the boundary layer according to the assumptions of the boundary layer (that is, $\partial P/\partial n \approx 0$).

Viscosity is defined as the property related to fluid friction or the internal resistance of the flow to be deformed by shear stresses (stickiness of the fluid) (Cengel, Y. A. and Ghajar, A. J. 2015). A flow is considered viscous when the frictional interactions between the fluid and the wall are non-negligible. In contrast, an inviscid flow is characterized by the absence of significant viscous effects, where the transport phenomena associated with mass, momentum, and energy are effectively negligible. It is important to note that no flow is perfectly inviscid; all fluids possess some degree of viscosity. However, the concept of inviscid flow is utilized in regions where the effects of viscosity are sufficiently small to be ignored, simplifying the analysis of certain flow phenomena, such as outside of the boundary layer. In the vicinity of a solid surface, the no-slip condition arises due to the strong molecular attraction between the surface and the fluid, causing the fluid molecules to adhere to the surface. As a result, the fluid velocity at the wall is zero, and the velocity increases with distance from the surface, leading to a reduction in

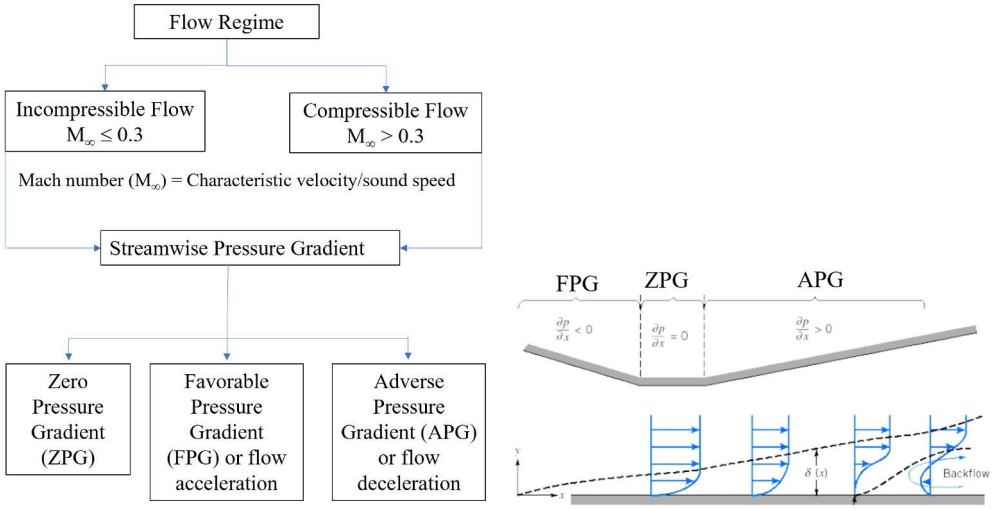

(a) (b)

Figure 2.1: (a) Pressure Gradient and (b) Flow Regime diagrams.

shear stress. According to Prandtl's boundary layer theory, a boundary layer forms along the surface, within which viscous effects cannot be neglected. In this boundary layer, shear stress develops, which is proportional to the local velocity gradient. Given that viscosity is directly related to shear stress, it can be understood as the fluid's resistance to shear deformation. In compressible flows, thermal transport plays a crucial role. The thermal boundary layer, which forms as a result of temperature gradients between the solid surface and the freestream, influences the overall heat transfer characteristics of the system (Cengel, Y. A. and Ghajar, A. J. 2015).

2.2 Mathematical Formulation

This section presents a discussion on the governing equations of laminar boundary layers, along with the associated initial and boundary conditions. Additionally, it addresses the coordinate and velocity transformations necessary to achieve a similarity state. These transformations are fundamental in reducing the complexity of the governing partial differential equations, enabling their solution under the assumption of similarity, which leads to a more tractable form of the boundary layer problem.

2.2.1 The Incompressible Boundary Layer Equations

Applying the Prandtl assumptions to the NS and neglecting buoyancy, the velocity is uncoupled from the temperature field. This means that the Boundary Layer equations can be applied without taking into account the energy section (White, F. M. 1991) as:

The continuity equation:

$$\frac{\partial u}{\partial x} + \frac{\partial v}{\partial y} = 0 \tag{2.1}$$

The x-momentum equation in two-dimensional form reads:

$$u\frac{\partial u}{\partial x} + v\frac{\partial u}{\partial y} = U\frac{dU}{dx} + \nu\frac{\partial^2 u}{\partial y^2} \tag{2.2}$$

In the case of the energy equation for Incompressible flows at moderate speeds the shear stresses that results from the viscous effects can be neglected:

$$u\frac{\partial T}{\partial x} + v\frac{\partial T}{\partial y} = \frac{k}{\rho C_p}\frac{\partial^2 T}{\partial y^2} \tag{2.3}$$

2.2.2 The Blasius Incompressible Flow Solution

The Blasius solution (Blasius, H. 1908) for incompressible flow is obtained by applying a similarity transformation to the Boundary Layer equations (equations 2.1 and 2.2) for a constant pressure gradient, $\frac{dU}{dx} = 0$.

Blasius found that similarity was achieved when:

$$\eta = y\sqrt{\frac{U}{2\nu x}} \tag{2.4}$$

Applying the similarity variable (equation 2.4) to equations 2.1 and 2.2 the Blasius momentum solution is obtained:

$$f''' + ff'' = 0 \tag{2.5}$$

In this equation, f'' is related to shear stress, f' is related to velocity, and f is related to the stream function.

According to the Prandtl assumptions the normal component of the velocity dominates over the parallel component in the direction perpendicular to the wall, so:

$$u = U_e f' \tag{2.6}$$

The momentum boundary layer can be found by searching for what η the local speed is 99% of the free stream velocity.

In the Blasius solution this value is around $\eta = 3.5$ and can be found analytically as:

$$\delta_{99\%} = 3.5\sqrt{\frac{2\nu x}{U}} \tag{2.7}$$

2.2.3 The Falkner Skan Incompressible Flow Solution

The Falkner-Skan solution (Falkner, V. M. and Skan, S. W. 1930) for incompressible flow is obtained by applying a similarity transformation to the Boundary Layer equations (equation 2.1 and 2.2).

Falkner Skan found that the similarity condition was achieved when:

$$\eta = Cyx^a \tag{2.8}$$

Where:

$$U(x) = Kx^m \tag{2.9}$$

$$m = 2a + 1 \tag{2.10}$$

$$C^2 = \frac{K(1+m)}{2\nu} \tag{2.11}$$

Note: ν is the kinematic viscosity in m^2/s.

Applying equations 2.9, 2.10 and 2.11 into equation 2.8 the similarity equation is obtained:

$$\eta = Y\sqrt{\frac{(m+1)U(x)}{2\nu x}} \tag{2.12}$$

Applying this similarity equation (equation 2.12) to the Boundary Layer incompressible equations (equations 2.1 and 2.2) the following Falkner-Skan similarity incompressible flow monetum equation is obtained:

Momentum equation:

$$f''' + ff'' + \beta(1 - f'\ f') = 0 \tag{2.13}$$

In this equation, f'' is related to shear stress, f' is related to the velocity, f is related to the stream function, and β is the pressure gradient related to the wedge angle.

The local velocity can be obtained by the equation 2.6.

The skin friction coefficient is obtained as:

$$C_f = \frac{2\tau_w}{\rho U^2} \tag{2.14}$$

The β parameter can be obtained as:

$$\beta = \frac{2\theta}{\pi} \tag{2.15}$$

Or

$$\beta = \frac{2m}{1+m} \tag{2.16}$$

The momentum boundary layer thickness can be obtained by finding η where the local speed is 99% of the free stream velocity, this value is used in equation 2.12 to obtain the y coordinate when this happens for different x values. Note that the Blasius solution can be obtained by setting $\beta = 0$ for a flat plate.

2.2.4 The Energy Equation in Incompressible Flows

Applying equation 2.4 to the Energy equation (equation 2.3) the following similarity equation is obtained:

$$g'' + Prfg' = 0 \tag{2.17}$$

In this equation g is related to dimensionless temperature and g' is related to the heat flux.

The local temperature can be obtained as:

$$g = \frac{T - T_e}{T_w - T_e} \tag{2.18}$$

The thermal boundary layer thickness can be obtained by finding η where the local temperature is 1% of the free stream temperature. The energy similarity equation holds for Blasius and Falkner-Skan similarity solutions if the viscous dissipation term is neglected and if the wall and stream temperatures remain constant.

2.2.5 Blasius Incompressible Flow Finite Difference Transformation

As stated before Finite Difference is going to be used to avoid the shooting method in the Forward Euler (FE) and Runge-Kutta Fourth Order (RK4) formulations. When applying the FE and RK4 methods, an order reduction is required to write the third-order differential equation in terms of four differential equations. In the finite-difference analysis the Blasius equation is written in terms of two ordinary equations one of first order and the other one of second order (Han, S. 2013).

Equation 2.5 in terms of the $f^{'}$ is written as:

$$\frac{\partial^2 f^{'}}{\partial \eta^2} + f\frac{\partial f^{'}}{\partial \eta} = 0 \tag{2.19}$$

The free stream term in equation 2.19 can be written as:

$$\frac{\partial f}{\partial \eta} = f^{'} \tag{2.20}$$

Applying a modified Forward Euler (Zill, D. and Warren, W. 2013; Han, S. 2013) to equation 2.20 yields:

$$f_{i+1} = f_i + \Delta\eta\frac{(f^{'}_{i+1} + f^{'}_i)}{2} \tag{2.21}$$

Applying Central Difference to equation 2.19 yields:

Implicit:

$$(2 + \Delta\eta f_i)f^{'}_{i+1} - 4f^{'}_i + (2 - \Delta\eta f_i)f^{'}_{i-1} = 0 \tag{2.22}$$

Explicit:

$$f^{'}_i = \frac{(2 + \Delta\eta f_i)f^{'}_{i+1} + (2 - \Delta\eta f_i)f^{'}_{i-1}}{4} \tag{2.23}$$

Its important to mention that the implicit solution is solved by the Thomas algorithm and that the explicit solution is solved by a standard iterative procedure where the previous values are used to find the next values until a convergence is reached.

2.2.6 Falkner-Skan Laminar Incompressible Flow Finite Difference Transformation

In the Falkner-Skan equation the same procedure as stated in 2.2.5 is used.

Equation 2.13 in terms of $f^{'}$ is written as:

$$\frac{\partial^2 f^{'}}{\partial \eta^2} + f\frac{\partial f^{'}}{\partial \eta} - \beta(1 - f^{'}f^{'}) = 0 \tag{2.24}$$

The f term is solved by applying a Modified Forward Euler to equation 2.20 yielding equation 2.21.

Applying Central difference to equation 2.24 yields:

Implicit:

$$(2 + \Delta\eta f_i)f^{'}_{i+1} - (4 + 2\beta\Delta\eta^2 f^{'}_i)f^{'}_i + (2 - \Delta\eta f_i)f^{'}_{i-1} = -2\Delta\eta^2\beta \tag{2.25}$$

Explicit:

$$f^{'}_i = \frac{(2 + \Delta\eta f_i)f^{'}_{i+1} + (2 - \Delta\eta f_i)f^{'}_{i-1} + 2\Delta\eta^2\beta}{(4 + 2\beta\Delta\eta^2 f^{'}_i)} \tag{2.26}$$

Finally the $f^{''}$ can be found by solving:

$$\frac{\partial f^{'}}{\partial \eta} = f^{''} \tag{2.27}$$

Applying a high order Forward difference at the first node yields:

$$f^{''}_1 = \frac{-f^{'}_{1+2} + 4f^{'}_{1+1} - 3f^{'}_1}{2\Delta\eta} \tag{2.28}$$

Applying a high-order Backward difference at the last node N yields:

$$f_N^{''} = \frac{3f_N^{'} - 4f_{N-1}^{'} + f_{N-2}^{'}}{2\Delta\eta} \tag{2.29}$$

Applying a Central difference at the interior nodes yields:

$$f_i^{''} = \frac{f_{i+1}^{'} - f_{i-1}^{'}}{2\Delta\eta} \tag{2.30}$$

In the end equations 2.21, 2.25 and 2.26 are used to find the values of f and $f^{'}$ via an implicit or explicit an method. Equation 2.28 can be used to find the shear stress in the wall and equations 2.29 and 2.30 are used to completely solve the term $f^{''}$.

2.2.7 Finite Difference Scheme for Thermal Laminar Boundary layers in Incompressible Flows

In the Energy equation the same procedure stated in section 2.2.5 and 2.2.6 is used.

Equation 2.17 in terms of the g is written as:

$$\frac{\partial^2 g}{\partial \eta^2} + Prf\frac{\partial g}{\partial \eta} = 0 \tag{2.31}$$

Applying Central difference to equation 2.31 yields:

Implicit:

$$(2 + Pr\Delta\eta f_i)g_{i+1} - 4g_i + (2 - Pr\Delta\eta f_i)g_{i-1} = 0 \tag{2.32}$$

Explicit:

$$g_i = \frac{(2 + Pr\Delta\eta f_i)g_{i+1} + (2 - Pr\Delta\eta f_i)g_{i-1}}{4} \tag{2.33}$$

Finally the $g^{'}$ can be found by solving:

$$\frac{\partial g}{\partial \eta} = g^{'} \tag{2.34}$$

Applying a high order Forward difference at the first node yields:

$$g_1^{'} = \frac{-g_{1+2} + 4g_{1+1} - 3g_1}{2\Delta\eta} \tag{2.35}$$

Applying a high order Backward difference at the last node N yields:

$$g_N^{'} = \frac{3g_N - 4g_{N-1} + g_{N-2}}{2\Delta\eta} \tag{2.36}$$

Applying a Central difference at the interior nodes yields:

$$g_i^{'} = \frac{g_{i+1} - g_{i-1}}{2\Delta\eta} \tag{2.37}$$

In the final stage, the equations 2.32 and 2.33 are employed to determine the value of g using either an implicit or an explicit method. Equation 2.35 is utilized to calculate the heat flux at the wall, while equations 2.36 and 2.37 are applied to fully resolve the $g^{'}$ term throughout the domain.

2.2.8 Blasius, Falkner Skan and Energy Similarity Boundary Conditions

These types of problems are solved as a boundary condition problem. The setup of the incompressible flow simulation is very similar to the compressible set up detailed in Figure 2.5.

The boundary conditions near the wall are:

$$f(0) = f'(0) = 0 \tag{2.38}$$

$$g(0) = 1 \tag{2.39}$$

The boundary conditions far from the wall:

$$f'(\infty) = 1 \tag{2.40}$$

$$g(\infty) = 0 \tag{2.41}$$

Figure 2.2 shows a flow chart of the procedure used to perform the Blasius incompressible flow simulation. Figure 2.3 shows a flow chart of the procedure used to perform the Falkner-Skan simulation. Figure 2.4 shows a flow chart of the procedure used to perform the Energy equation simulation.

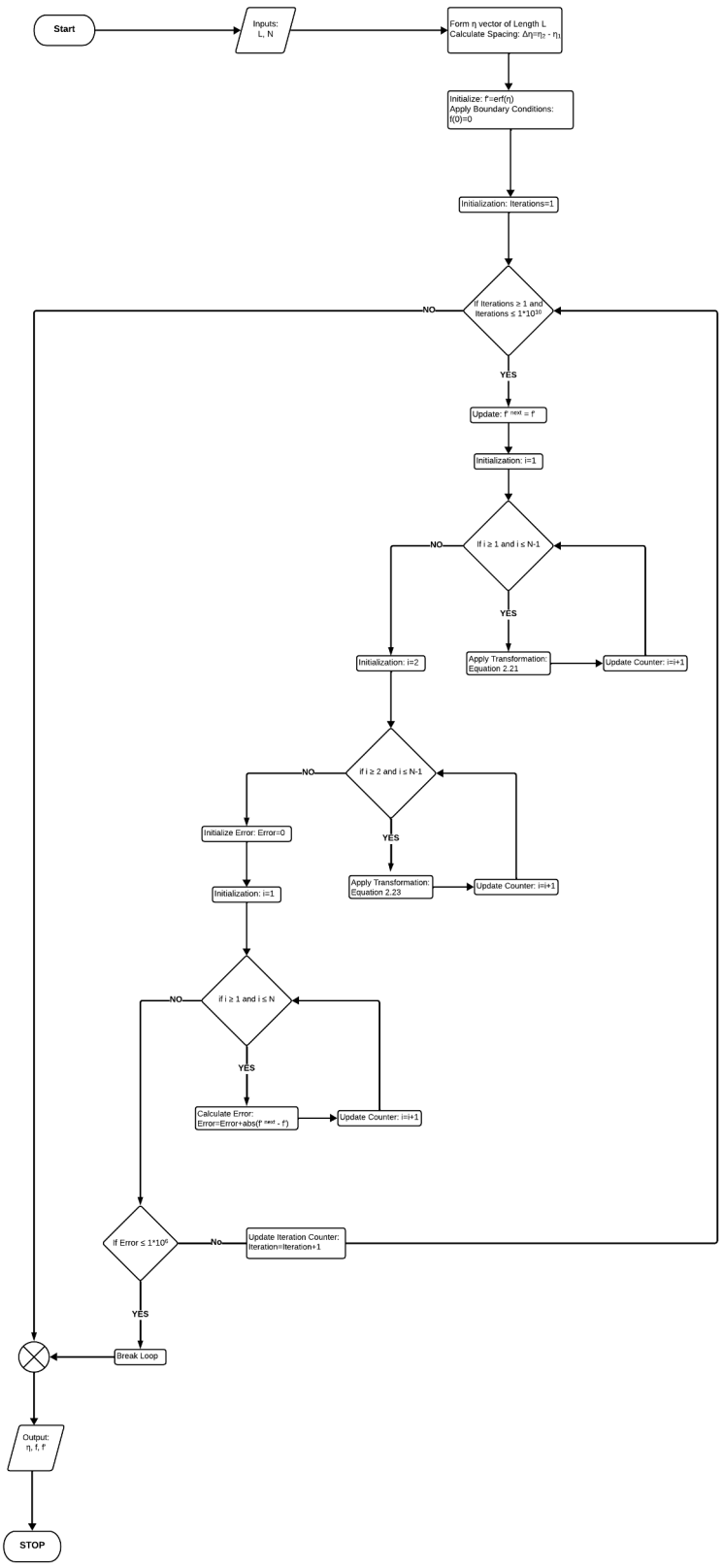

Figure 2.2: Blasius incompressible flow simulation flow chart.

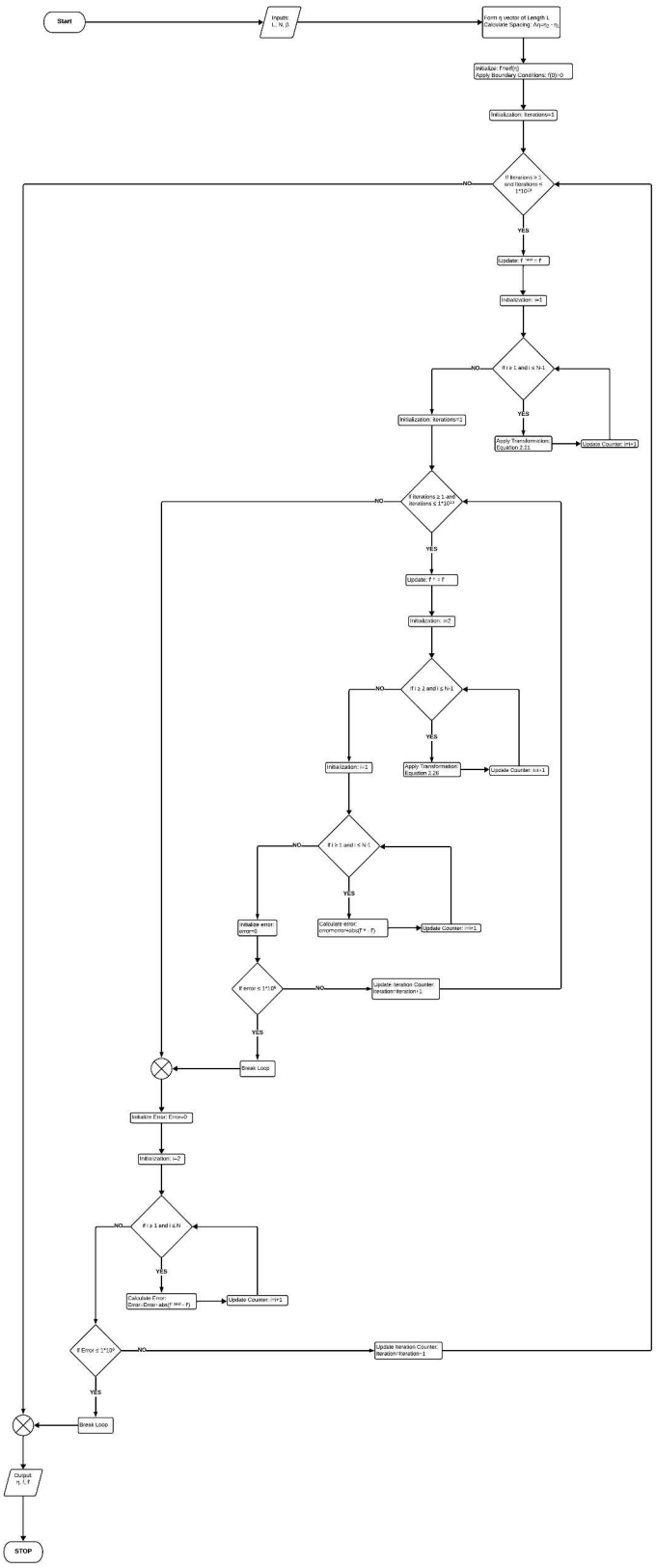

Figure 2.3: Falkner-Skan incompressible flow simulation flow chart.

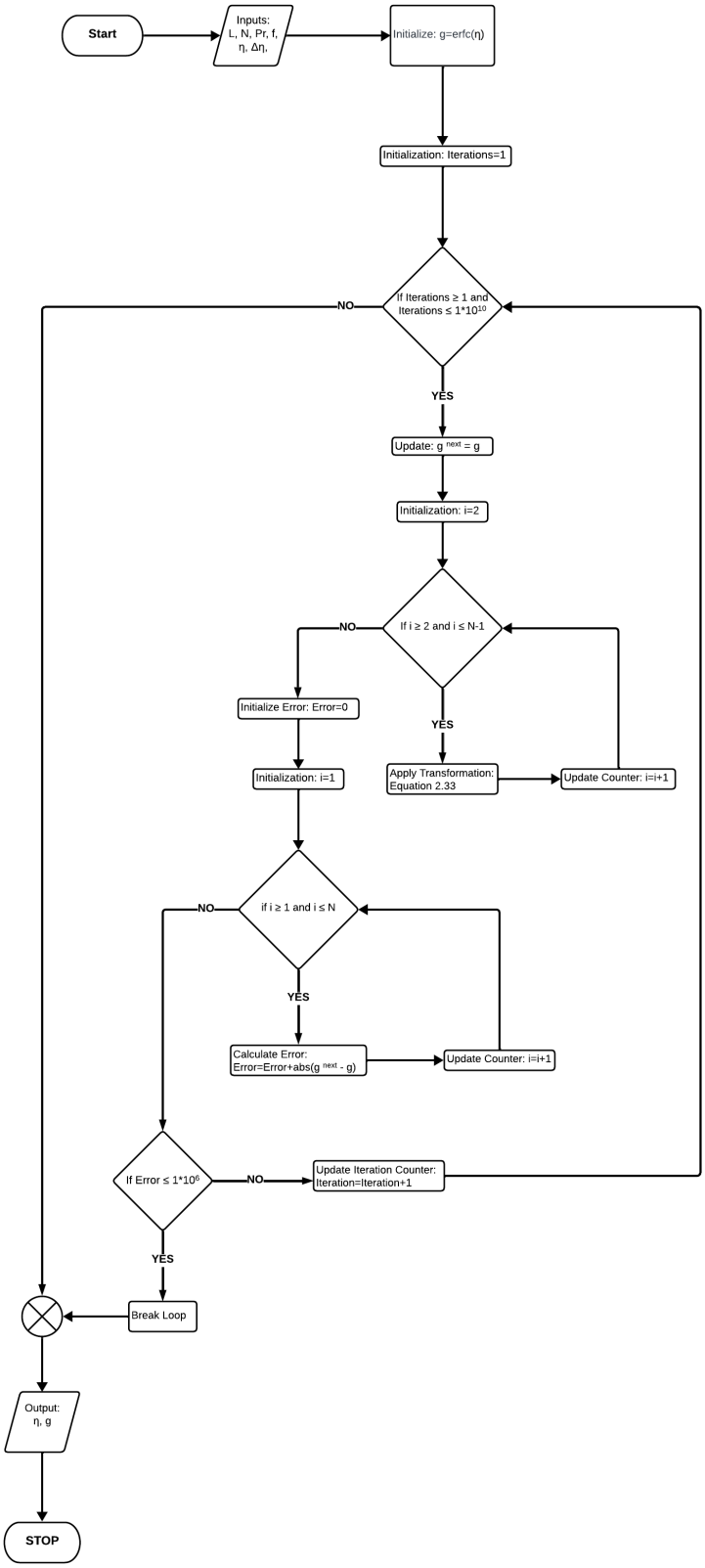

Figure 2.4: Energy equation incompressible flow simulation flow chart.

2.2.9 The Compressible Boundary Layer Equations

The boundary layer equations, as outlined by White (White, F. M. 1991), are composed of three distinct sections: a continuity equation that ensures mass conservation of the flow, a momentum equation that governs the dynamics of the flow, and an energy equation that describes the transfer of energy within the fluid. It is crucial to note that for compressible flow, the Prandtl assumption must be satisfied. This assumption asserts that the viscosity and thermal conductivity are functions of temperature, which leads to the coupling of the energy equation with the momentum equation. As a result, the temperature variation within the flow directly influences the flow's velocity field, requiring a simultaneous solution of both equations to fully characterize the system.

The continuity equation:

$$\frac{\partial(\rho u)}{\partial x} + \frac{\partial(\rho v)}{\partial y} = 0 \tag{2.42}$$

The x-momentum equation reads:

$$\rho u\frac{\partial u}{\partial x} + \rho v\frac{\partial u}{\partial y} = -\frac{dP_e}{dx} + \frac{\partial}{\partial y}\left(\mu\frac{\partial u}{\partial y}\right) \tag{2.43}$$

The energy equation is given as:

$$\rho u\frac{\partial h}{\partial x} + \rho v\frac{\partial h}{\partial y} = u\frac{dP_e}{dx} + \frac{\partial}{\partial y}\left(\frac{\mu}{Pr}\frac{\partial h}{\partial y}\right) + \mu\left(\frac{\partial u}{\partial y}\right)^2 \tag{2.44}$$

Where:

$$h = C_p T \tag{2.45}$$

2.2.10 The Falkner-Skan Compressible Flow Solution

The Falkner-Skan solution for compressible flow is obtained via the application of the Illingworth transformation to equations 2.42, 2.43 and 2.44.

Illingworth accounted for viscosity effects in ξ and density effects in η, as seen in the

following equations (White, F. M. 1991):

$$\xi(x) = \int_0^x \rho_e\ (x)\ U_e\ (x)\mu_e\ (x)\ dx \tag{2.46}$$

$$\eta(x,y) = \frac{U_e}{\sqrt{2\xi}} \int_0^y \rho\ dy \tag{2.47}$$

Applying this similarity transformation coordinate (equations 2.46 and 2.47) to equations 2.42, 2.43 and 2.44 the following Falkner-Skan compressible flow similarity equations are obtained:

Momentum equation:

$$(Cf'')' + ff'' = \beta(f'f' - g) \tag{2.48}$$

Energy equation:

$$(Cg')' + Prfg' = -BC(f''\ f'') \tag{2.49}$$

Where:

$$C = \frac{\rho\mu}{\rho_e\mu_e} = g^{n-1} \tag{2.50}$$

$$B = Pr(\gamma - 1)M_{ae}^2 \tag{2.51}$$

In this equations f'' is related to the shear stress, f' is related to the velocity, f is related to the stream function, β is the pressure gradient related to the wedge angle, C is the ratio between the density and viscosity and the freestream density and viscosity, g' is related to the heat flux and g is related to the temperature and density ratios, respectively. The local velocity and skin friction coefficient can be obtained by equations 2.6 and 2.14. The momentum boundary layer thickness can be obtained by finding η where the local speed is 99% of the free stream velocity. In addition, the thermal boundary layer can be obtained by finding the coordinate η where the normalized local temperature has a value of 1.01 for a heated wall and 0.99 for a cold wall. Notice that the Blasius solution can be obtained by setting C = 1 and $\beta = 0$ for a flat plate.

2.2.11 The Blasius Compressible Flow Solution for C = 1

As stated in section 2.2.10, the Blasius solution for compressible flow is obtained by setting $C = 1$ and a β of zero in equations 2.48 and 2.49.

Blasius compressible Momentum equation:

$$f''' + ff'' = 0 \tag{2.52}$$

Blasius compressible Energy equation:

$$g'' + g' Prf = -Bf'' f'' \tag{2.53}$$

Where:

$$B = Pr(\gamma - 1)M_{ae}^2 \tag{2.54}$$

As in section 2.2.10, in these equations,f'' is associated with the shear stress, f' corresponds to the velocity gradient, f represents the stream function, g is related to the temperature distribution, and g' is connected to the heat flux. These relationships are essential for analyzing the behavior of the boundary layer, as they provide a link between the velocity, temperature, and shear stress profiles within the flow.

The local velocity and the skin friction coefficient can be obtained by using equations 2.6 and 2.14 located in section 2.2.3.

A procedure analogous to the one described in Section 2.2.5 is employed to overcome the shooting method utilized in the Forward Euler (FE) and Runge-Kutta 4th order (RK4) formulations.

Equation 2.52 in term of the f' is written as:

$$\frac{\partial^2 f'}{\partial \eta^2} + f\frac{\partial f'}{\partial \eta} = 0 \tag{2.55}$$

Equation 2.53 in term of the g is written as:

$$\frac{\partial^2 g}{\partial \eta^2} + Prf\frac{\partial g}{\partial \eta} = -Bf'' f'' \tag{2.56}$$

The f term is solved by applying a Modified Forward Euler to equation 2.20 yielding equation 2.21.

Applying central difference to equation 2.55 yields:

Implicit:

$$(2 + \Delta\eta f_i)f'_{i+1} - 4f'_i + (2 - \Delta\eta f_i)f'_{i-1} = 0 \tag{2.57}$$

Explicit:

$$f'_i = \frac{(2 + \Delta\eta f_i)f'_{i+1} + (2 - \Delta\eta f_i)f'_{i-1}}{4} \tag{2.58}$$

Applying central difference to equation 2.56 yields:

Implicit:

$$(2 + \Delta\eta Pr f_i)g_{i+1} - 4g_i + (2 - \Delta\eta Pr f_i)g_{i-1} = -2\Delta\eta^2 B f''_i f''_i \tag{2.59}$$

Explicit:

$$g_i = \frac{(2 + \Delta\eta Pr f_i)g_{i+1} + (2 - \Delta\eta Pr f_i)g_{i-1} + 2\Delta\eta^2 B f''_i f''_i}{4} \tag{2.60}$$

The terms f'' and g' terms can be found by solving equations 2.27 and 2.34. These equations are solved via a Finite Difference transformation by a applying a high order Forward Difference at the first node (equations 2.28 and 2.35), Central Difference at the interior nodes (equations 2.30 and 2.37) and a high order Backward Finite Difference at the last node N (equations 2.29 and 2.36).

As stated before, equations 2.57, 2.58, 2.59, 2.60 and 2.21 can be used to solve for the f', g and f terms via an implicit or explicit method. Equations 2.28 and 2.35 can be used to find the shear stress and heat flux at the wall and equations 2.30, 2.37, 2.29 and 2.36 are used to completely solve the f'' and g' terms.

2.2.12 Blasius Laminar Compressible Flow Solution for Variable C

In this section, a Blasius laminar compressible flow solution with a variable C value is assumed. When C varies with η, the momentum and energy equations become strongly coupled.

Blasius compressible momentum equation:

$$Cf''' + f''(C' + f) = 0 \tag{2.61}$$

Blasius compressible energy equation:

$$Cg'' + g'(C' + Prf) = -BCf''f'' \tag{2.62}$$

Where:

$$C' = (n-1)g^{n-2}g' \tag{2.63}$$

C and B are given by equations 2.50 and 2.51.

As seen in the previous sections, f'' is related to the shear stress, f' is related to the velocity, f is related to the stream function, g is related to the temperature, g' is related to the heat flux and C is related to the temperature and density ratios.

The local velocity and the skin friction coefficient can be obtained by using equations 2.6 and 2.14 located in section 2.2.3.

A similar procedure to Section 2.2.5 is used to eliminate the shooting method used in the FE and RK4 formulations. Equation 2.61 in term of the f' is written as:

$$C\frac{\partial^2 f'}{\partial \eta^2} + \frac{\partial f'}{\partial \eta}(C' + f) = 0 \tag{2.64}$$

Equation 2.62 in term of the g is written as:

$$C\frac{\partial^2 g}{\partial \eta^2} + \frac{\partial g}{\partial \eta}(C' + Prf) = -BCf''f'' \tag{2.65}$$

The f term is solved by applying a Modified Forward Euler to equation 2.20 yielding equation 2.21. Applying central difference to equation 2.64 yields:

Implicit:

$$(2C_i + \Delta\eta(C_i' + f_i))f_{i+1}' - 4C_i f_i' + (2C_i - \Delta\eta(C_i' + f_i))f_{i-1}' = 0 \tag{2.66}$$

Explicit:

$$f_i' = \frac{(2C_i + \Delta\eta(C_i' + f_i))f_{i+1}' + (2C_i - \Delta\eta(C_i' + f_i))f_{i-1}'}{4C_i} \tag{2.67}$$

Applying central difference to equation 2.65 yields the following schemes.

Implicit:

$$(2C_i+\Delta\eta(C_i^{'}+Prf_i))g_{i+1}-4C_ig_i+(2C_i-\Delta\eta(C_i^{'}+Prf_i))g_{i-1}=-2\Delta\eta^2BC_if_i^{''}f_i^{''} \quad (2.68)$$

Explicit:

$$g_i=\frac{(2C_i+\Delta\eta(C_i^{'}+Prf_i))g_{i+1}+(2C_i-\Delta\eta(C_i^{'}+Prf_i))g_{i-1}+2\Delta\eta^2BC_if_i^{''}f_i^{''}}{4C_i} \quad (2.69)$$

The terms $f^{''}$ and $g^{'}$ can be found by solving equations 2.27 and 2.34. These equations are solved via a Finite Difference transformation by a applying a high order Forward Difference at the first node (equations 2.28 and 2.35), Central Difference at the interior nodes (equations 2.30 and 2.37) and a high order Backward Finite Difference at the last node N (equations 2.29 and 2.36). As stated before, equations 2.66, 2.67, 2.68, 6.14 and 2.21 can be used to solve for the $f^{'}$, g and f terms via an explicit or implicit method. Equations 2.28 and 2.35 can be used to find the shear stress and heat flux at the wall and equations 2.30, 2.37, 2.29 and 2.36 are used to completely solve the $f^{''}$ and $g^{'}$ terms.

2.2.13 Boundary Condition Prescription

This type of problem is solved as a boundary condition value problem. Figure 2.5 shows the setup of the laminar compressible flow simulation.

For a C equal to one and a variable C at Mach number equal to zero:

• The boundary conditions near the wall are:

$$f(0)=f^{'}(0)=0 \quad (2.70)$$

$$g\ (0)=1\ for\ Adiabatic\ wall \quad (2.71)$$

$$g'\ (0)=0\ for\ Adiabatic\ wall \quad (2.72)$$

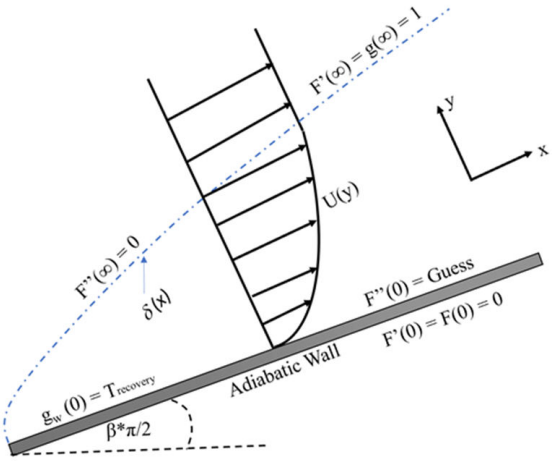

Figure 2.5: Simulation set up diagram.

• The boundary conditions far from the wall:

$$f'(\infty) = 1 \tag{2.73}$$

$$g(\infty) = 1 \tag{2.74}$$

For the hot and cold wall cases with constant C equal to one and the hot and the cold wall cases with variable C at a Mach number of zero the boundary conditions are as follows:

• The f and $f^{'}$ boundary conditions at the wall stay the same.

• The g boundary conditions at the wall:

$$g(0) = g_w \tag{2.75}$$

• The $f^{'}$ and g boundary conditions at far from the wall stay the same.

Note: In this case if the g_w is more than one the flow is considered a hot wall flow and if is less than one is considered a cold wall flow.

For the case of C equal to one and the case with variable C at a Mach number not equal to zero, the boundary conditions are as follows:

- The f and $f^{'}$ boundary conditions at the wall stay the same.

- The $f^{'}$ and g boundary conditions at far from the wall stay the same.

- The adiabatic condition at the wall is found by changing g_w until the $g_w^{'}$ is zero. In the case of hot and cold wall conditions, the values of g_w are prescribed larger or lower than the adiabatic temperature, respectively.

Figure 2.6 show a flow chart of the procedure used to perform the Blasius compressible simulation for $C = 1$. In a similar way, Figure 2.7 shows a flow chart of the procedure used to perform the Blasius compressible flow simulation under variable C.

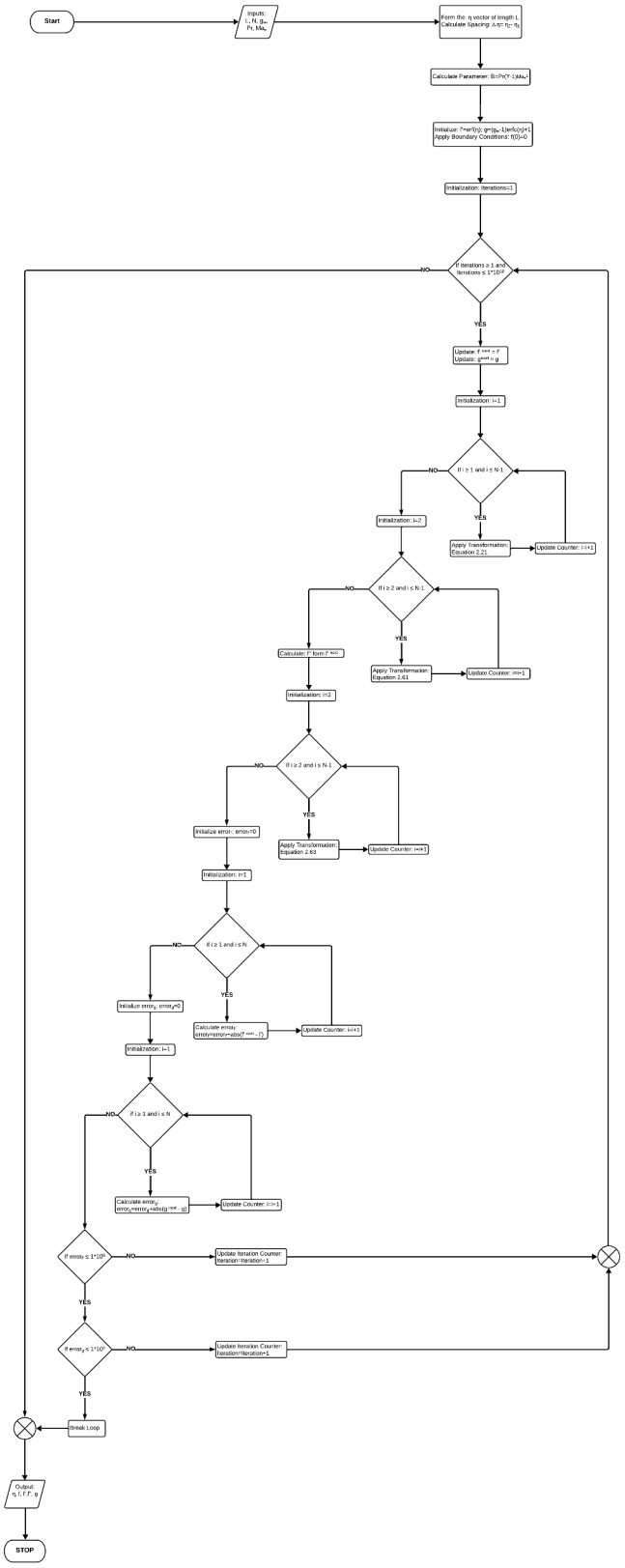

Figure 2.6: Blasius compressible flow $C = 1$ simulation flow chart.

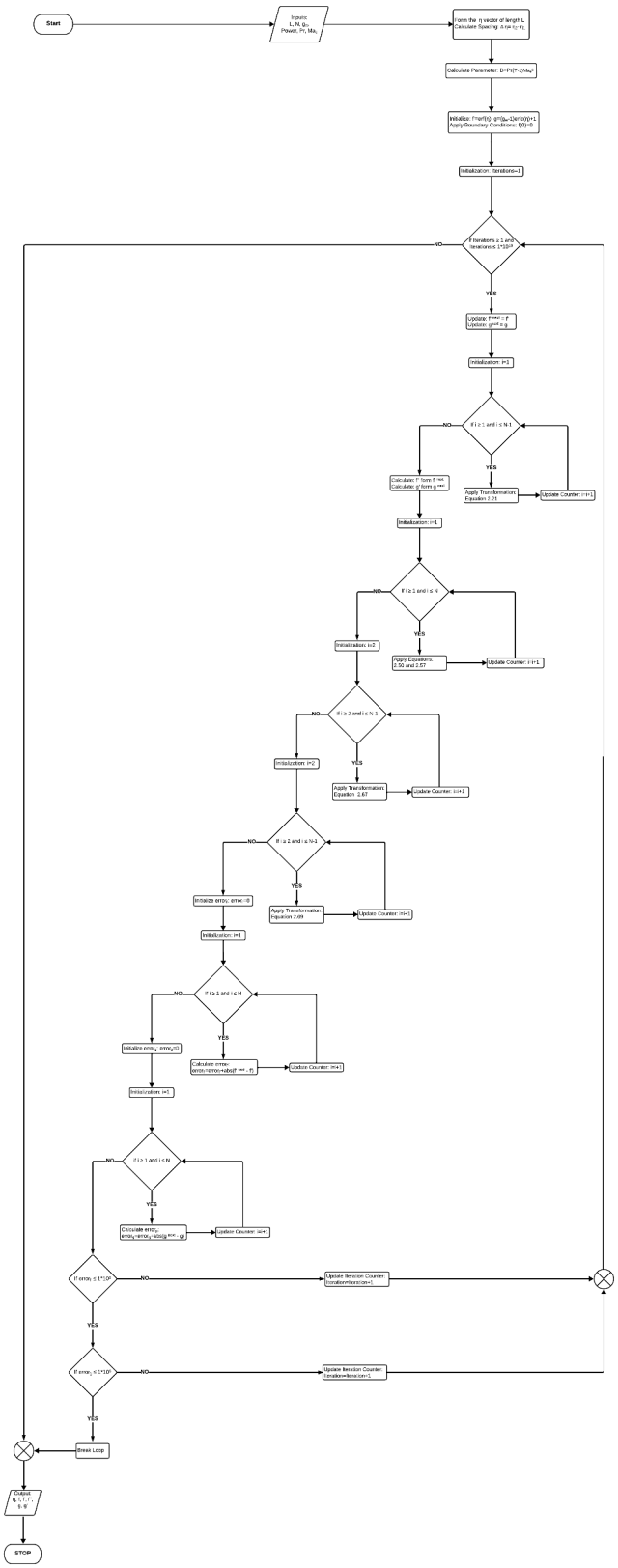

Figure 2.7: Blasius compressible flow simulation flow chart for $C \neq 1$.

Chapter 3
Flow Stability Theory

3.1 Stability Theory

As previously discussed, fluid flow can exist in laminar, transitional, or turbulent regimes. To classify the flow state, the Reynolds number is utilized, representing the ratio of inertial forces to viscous forces within the fluid. Laminar flow is characterized by smooth, orderly motion, while turbulent flow is defined by chaotic and irregular fluid movement. Laminar flows are susceptible to instability at high Reynolds numbers, making them prone to transition to turbulence (White, F. M. 1991). For any laminar flow, there exists a critical Reynolds number−typically small−at which the flow transitions to a mixed state, known as transitional flow. Since transitional flow exhibits characteristics of both laminar and turbulent flows, it is analyzed by performing a stability analysis on the Navier-Stokes (NS) equations. Stability analysis examines whether a physical system can return to its original state or position following a disturbance. Four types of stability conditions are typically considered:

• Unconditionally stable: where the physical state returns to its original form no matter the disturbance.

• Unstable state: where the physical state cannot return to its original physical form.

• Neutral stability: where the physical state will have its original form no matter the disturbance.

• Partial stability: where the physical state is a mixture of unconditional or unstable state. This is the case for laminar boundary layer flow.

Stability is studied in fluid mechanics by adding a disturbance to the NS equations in the form of a traveling wave. Stability theory predicts the end of the laminar flow section but does not predict the beginning of turbulence. According to (White, F. M. 1991), there is still no clear theory on transition. It should be mentioned that stability theory

can be used to predict the effect of the wall temperature, streamwise pressure gradient, and Mach number on the stability of laminar flow.

The stability analysis on the NS equations is done by performing the following steps (White, F. M. 1991):

• Choose a flow solution Q_0. Examples of flow solutions: Couette Flow, Poiseuille Flow, Boundary Layer Flow, etc. In this case, the Navier-Stokes equations.

• Add a disturbance $\hat{Q}$ and plug in $Q_0 + \hat{Q}$ in to the NS equations.

• Simplify NS by subtracting the basic terms that Q_0 satisfy identically.

• Linearize the NS disturbance equations assuming small disturbances $\hat{Q} << Q_0$ and neglect terms like $\hat{Q}^2$, $\hat{Q}^3$, etc..

• Assume a form of the disturbance. In the case of NS a Tollmien-Schlichting wave.

• The linearized NS equations are homogeneous with homogeneous boundary conditions. This is an eigenvalue problem.

• Finally, the eigenvalue problem solution is a chart showing the regions of stability separated from the unstable region by a neutral curve.

According to (Wazzan, A. R., Okamura, T. and Smith, A. M. O. 1968; Ozgen, S. 2004), several assumptions can be made to simplify the stability analysis:

• Parallel flow is assumed, meaning that the velocity component u varies in the y-direction, while the v-component is negligible compared to the u-component. As a result, the v-component is considered to be zero.

• The temperature is assumed to vary solely in the y-direction. This implies that flow properties such as density, viscosity, thermal conductivity, and others, which are temperature-dependent, will also exhibit variation in the y-direction.

3.2 Orr-Sommerfeld Equation

As stated in the previous section, the stability analysis is performed by applying a disturbance to NS.

NS for incompressible flow consists of a continuity, momentum and energy (energy equation is decoupled from momentum equations) equations:

- Continuity equation which studies the mass conservation:

$$\frac{\partial u}{\partial x} + \frac{\partial v}{\partial y} + \frac{\partial w}{\partial z} = 0 \tag{3.1}$$

- X-Momentum equation which studies the flow dynamics in the x direction:

$$\frac{\partial u}{\partial t} + u\frac{\partial u}{\partial x} + v\frac{\partial u}{\partial y} + w\frac{\partial u}{\partial z} = \frac{-1}{\rho}\frac{dP}{dx} + \nu\left(\frac{\partial^2 u}{\partial x^2} + \frac{\partial^2 u}{\partial y^2} + \frac{\partial^2 u}{\partial z^2}\right) \tag{3.2}$$

- Y-Momentum equation which studies the flow dynamics in the y direction:

$$\frac{\partial v}{\partial t} + u\frac{\partial v}{\partial x} + v\frac{\partial v}{\partial y} + w\frac{\partial v}{\partial z} = \frac{-1}{\rho}\frac{dP}{dy} + \nu\left(\frac{\partial^2 v}{\partial x^2} + \frac{\partial^2 v}{\partial y^2} + \frac{\partial^2 v}{\partial z^2}\right) \tag{3.3}$$

- Z-Momentum equation which studies the flow dynamics in the z direction:

$$\frac{\partial w}{\partial t} + u\frac{\partial w}{\partial x} + v\frac{\partial w}{\partial y} + w\frac{\partial w}{\partial z} = \frac{-1}{\rho}\frac{dP}{dz} + \nu\left(\frac{\partial^2 w}{\partial x^2} + \frac{\partial^2 w}{\partial y^2} + \frac{\partial^2 w}{\partial z^2}\right) \tag{3.4}$$

It is important to mention that stability for incompressible flow is applied to the continuity and momentum equations. One of the main assumptions when applying a stability analysis to NS is the Squires theorem. Squires theorem states: that for any two-dimensional parallel flow, the minimum critical unstable Reynolds number is for the case of a two-dimensional disturbance propagating along the same direction. This means that the most unstable disturbance occurs at 2D parallel flow (White, F. M. 1991; Cimbala, J. M.). Since the most unstable disturbance occurs in two dimensions the stability analysis of NS can be performed for a two-dimensional flow (Simpson, C. 2015a).

For two-dimensional flow, NS reduces to:

- Continuity equation:

$$\frac{\partial u}{\partial x} + \frac{\partial v}{\partial y} = 0 \tag{3.5}$$

- X-Momentum equation:

$$\frac{\partial u}{\partial t} + u\frac{\partial u}{\partial x} + v\frac{\partial u}{\partial y} = \frac{-1}{\rho}\frac{dP}{dx} + \nu\left(\frac{\partial^2 u}{\partial x^2} + \frac{\partial^2 u}{\partial y^2}\right) \tag{3.6}$$

- Y-Momentum equation:

$$\frac{\partial v}{\partial t} + u\frac{\partial v}{\partial x} + v\frac{\partial v}{\partial y} = \frac{-1}{\rho}\frac{dP}{dy} + \nu\left(\frac{\partial^2 v}{\partial x^2} + \frac{\partial^2 v}{\partial y^2}\right) \tag{3.7}$$

First, in order to perform a stability analysis a disturbance of the following form is added to NS for the velocity components and pressure:

$$u = U_0 + \hat{u} \tag{3.8}$$

$$v = V_0 + \hat{v} \tag{3.9}$$

$$P = P_0 + \hat{P} \tag{3.10}$$

Adding equations 3.8, 3.9 and 3.10 to equations 3.5, 3.6 and 3.7 yields:

- Continuity equation:

$$\frac{\partial}{\partial x}(U_0 + \hat{u}) + \frac{\partial}{\partial y}(U_0 + \hat{v}) = 0 \tag{3.11}$$

- X-Momentum equation:

$$\begin{aligned} &\frac{\partial(U_0 + \hat{u})}{\partial t} + (U_0 + \hat{u})\frac{\partial(U_0 + \hat{u})}{\partial x} + (V_0 + \hat{v})\frac{\partial(U_0 + \hat{u})}{\partial y} = \\ &\frac{-1}{\rho}\frac{d(P_0 + \hat{P})}{dx} + \nu\left[\frac{\partial^2(U_0 + \hat{u})}{\partial x^2} + \frac{\partial^2(U_0 + \hat{u})}{\partial y^2}\right] \end{aligned} \tag{3.12}$$

• Y-Momentum equation:

$$\frac{\partial(V_0+\hat{v})}{\partial t}+(U_0+\hat{u})\frac{\partial(V_0+\hat{v})}{\partial x}+(V_0+\hat{v})\frac{\partial(V_0+\hat{v})}{\partial y}= \\ \frac{-1}{\rho}\frac{d(P_0+\hat{P})}{dy}+\nu\left[\frac{\partial^2(V_0+\hat{v})}{\partial x^2}+\frac{\partial^2(V_0+\hat{v})}{\partial y^2}\right] \tag{3.13}$$

Simplifying, linearizing, and assuming parallel flow equations ($U = U(y)$ and $V = 0$) 3.11, 3.12 and 3.13 yield (White, F. M. 1991; Simpson, C. 2015a):

• Continuity equation:

$$\frac{\partial\hat{u}}{\partial x}+\frac{\partial\hat{v}}{\partial y}=0 \tag{3.14}$$

• X-Momentum equation:

$$\frac{\partial\hat{u}}{\partial t}+\hat{v}\frac{\partial U_0}{\partial y}+U_0\frac{\partial\hat{u}}{\partial x}=\frac{-1}{\rho}\frac{\partial\hat{P}}{\partial x}+\nu\left(\frac{\partial^2\hat{u}}{\partial x^2}+\frac{\partial^2\hat{u}}{\partial y^2}\right) \tag{3.15}$$

• Y-Momentum equation:

$$\frac{\partial\hat{v}}{\partial t}+U_0\frac{\partial\hat{v}}{\partial x}=\frac{-1}{\rho}\frac{\partial\hat{P}}{\partial y}+\nu\left(\frac{\partial^2\hat{v}}{\partial x^2}+\frac{\partial^2\hat{v}}{\partial y^2}\right) \tag{3.16}$$

The Tollmien-Schlichting wave for two dimensional flow is modeled by:

$$\hat{u}(x,y,t)=\bar{u}e^{i\alpha(xcos\theta-ct)} \tag{3.17}$$

$$\hat{v}(x,y,t)=\bar{v}e^{i\alpha(xcos\theta-ct)} \tag{3.18}$$

$$\hat{P}(x,y,t)=\bar{P}e^{i\alpha(xcos\theta-ct)} \tag{3.19}$$

Where t is the time, α is the wave number, c the wave propagation speed, $i=\sqrt{-1}$, x is a Cartesian coordinate, and θ is the wall wave angle with respect to the x-axis.

Note: The variables with the bar in equations 3.17, 3.18 and 3.19 are complex amplitudes of the $\hat{u}$, $\hat{v}$ and $\hat{P}$ disturbances.

Applying Squires theorem ($\theta = 0$) and rearranging equations 3.17, 3.18 and 3.19 yields:

$$\hat{u}(x, y, t) = \bar{u}e^{i\alpha(x-ct)} \tag{3.20}$$

$$\hat{v}(x, y, t) = \bar{v}e^{i\alpha(x-ct)} \tag{3.21}$$

$$\hat{P}(x, y, t) = \bar{P}e^{i\alpha(x-ct)} \tag{3.22}$$

Plugging equations 3.20, 3.21 and 3.22 in to equations 3.14, 3.15 and 3.16 yields:

- Continuity equation:

$$\bar{u}i\alpha + \bar{v}' = 0 \tag{3.23}$$

- X-Momentum equation:

$$i\alpha\bar{u}[U_0 - c] + \bar{v}U_0' = \frac{-i\alpha\bar{P}}{\rho} + \nu[\bar{u}'' + \bar{u}(i\alpha)^2] \tag{3.24}$$

- Y-Momentum equation:

$$i\alpha\bar{v}(U_0 - c) = \frac{-\bar{P}'}{\rho} + \nu[\bar{v}'' + \bar{v}(i\alpha)^2] \tag{3.25}$$

Where prime indicates differentiation with respect to y.

Now, the $\bar{u}$ and $\bar{p}$ terms must be eliminated. Rearranging equation 3.23 for $\bar{u}$:

$$\bar{u} = -\frac{\bar{v}'}{i\alpha} \tag{3.26}$$

Rearranging equation 3.24 for $\bar{p}$ and differentiating with respect to y:

$$\bar{P}' = -\rho[\bar{u}U_0' + U_0\bar{u}' - \bar{u}'c] - \frac{\bar{v}'U_0'}{i\alpha}\rho - \frac{\bar{v}U_0''}{i\alpha}\rho + \frac{\nu\rho}{i\alpha}[\bar{u}''' + \bar{u}(i\alpha)^2] \tag{3.27}$$

Rearranging equation 3.25 for $-\bar{P}'$:

$$-\bar{P}' = i\alpha\bar{v}\rho(U_0 - c) - \nu\rho[\bar{v}'' + \bar{v}(i\alpha)^2] \tag{3.28}$$

Adding equations 3.27 and 3.28 to eliminate the pressure term and plugging in equation 3.26 to eliminate $\bar{u}$ yields the Orr-Sommerfeld equation in dimensional form:

$$(U_0 - c)(\bar{v}'' - \alpha^2\bar{v}) - U_0''\bar{v} + \frac{\nu i}{\alpha}[\bar{v}'''' - 2\alpha^2\bar{v}'' + \alpha^4\bar{v}] = 0 \tag{3.29}$$

The Orr-Sommerfeld equation can be written in dimensionless form as:

$$(U^* - c^*)(\bar{\phi}'' - \alpha_\delta^2\bar{\phi}) - U^{*''}\bar{\phi} + \frac{i}{Re_\delta\alpha_\delta}[\bar{\phi}'''' - 2\alpha_\delta^2\bar{\phi}'' + \alpha_\delta^4\bar{\phi}] = 0 \tag{3.30}$$

Where:

$$\phi = \frac{\bar{v}}{U_e} \tag{3.31}$$

$$U^* = \frac{U_0}{U_e} \tag{3.32}$$

$$c^* = \frac{c}{U_e} \tag{3.33}$$

$$\alpha_\delta = \alpha\delta \tag{3.34}$$

$$Re_\delta = \frac{U_e\delta}{\nu} \tag{3.35}$$

Note: The Orr-Sommerfeld equation is non-dimensionalized with respect to the $\xi = \frac{y}{\delta}$ coordinate. In this case δ can be either the Boundary Layer thickness or the Displacement thickness.

In the Orr-Sommerfeld equation the disturbances must vanish at the wall and infinity. So for a Boundary Layer flow the boundary conditions are:

- At the wall:

$$\bar{v} = \bar{v}^{'} = \phi = \phi^{'} = 0 \tag{3.36}$$

- At infinity:

$$\bar{v} = \bar{v}^{'} = \phi = \phi^{'} = 0 \tag{3.37}$$

It can be noted that from equations 3.29, 3.30, 3.36 and 3.37 that this is an Eigenvalue problem due to the fact that the Orr-Sommerfeld equation and its boundary conditions are homogeneous.

In order to solve the Orr-Somerfeld equation it can be assumed that the disturbance grow spatialy (α complex and αc real) or temporally (α real and c complex). This research focuses on the temporal solution of Orr-Somerfeld.

3.3 Orr-Sommerfeld Equation Numerical Solution

The Orr-Sommerfeld can be solved using a Finite Difference scheme (Simpson, C. 2015b). Rearranging equation 3.30 so the c terms are in the right side and the non c terms in the left side yields:

$$a_1\phi^{''''} + a_2\phi^{''} + a_3\phi = c^*(b_1\phi^{''} + b_2\phi) \tag{3.38}$$

Where:

$$a_1 = -1 \tag{3.39}$$

$$a_2 = i\alpha_\delta Re_\delta U^* + 2\alpha_\delta^2 \tag{3.40}$$

$$a_3 = -i\alpha_\delta^3 Re_\delta U^* - i\alpha_\delta Re_\delta U^{*''} - \alpha_\delta^4 \tag{3.41}$$

$$b_1 = i\alpha_\delta Re_\delta \tag{3.42}$$

$$b_2 = -i\alpha_\delta^3 Re_\delta \tag{3.43}$$

Applying finite difference to equation 3.38 gives:

$$A_2\phi_{i+2} + A_1\phi_{i+1} + A_0\phi_i + A_{-1}\phi_{i-1} + A_{-2}\phi_{i-2} = c^*(B_1\phi_{i+1} + B_0\phi_i + B_{-1}\phi_{i-1}) \tag{3.44}$$

Where:

$$A_2 = a_1 \tag{3.45}$$

$$A_1 = -4a_1 + a_2\Delta\xi^2 \tag{3.46}$$

$$A_0 = 6a_1 - 2a_2\Delta\xi^2 + a_3\Delta\xi^4 \tag{3.47}$$

$$A_{-1} = -4a_1 + a_2\Delta\xi^2 \tag{3.48}$$

$$A_{-2} = a_1 \tag{3.49}$$

$$B_1 = b_1\Delta\xi^2 \tag{3.50}$$

$$B_0 = -2b_1\Delta\xi^2 + b_2\Delta\xi^4 \tag{3.51}$$

$$B_{-1} = b_1\Delta\xi^2 \tag{3.52}$$

Equation 3.44 can be written in matrix form as:

$$A\phi = c^* B\phi \tag{3.53}$$

Where A and B are the left and right hand matrices of equation 3.44.

Form equations 3.44 and 3.53 it can be seen that A is pentadiagonal matrix and B is a tridiagonal matrix.

In order to solve for the complex value c^* equation 3.53 yields:

$$B^{-1}A = c^* \tag{3.54}$$

This Eigenvalue problem can be solved using a Gram-Schmidt with a QR matrix algorithm. In this case a the Matlab EIG function is going to be used to solve this problem.

In order to solve the Orr-Sommerfeld equation, the U^* and $U^{*''}$ in terms of the ξ coordinate must be known. Next, the α_δ and Re_δ coordinates are set up. Once this is done, for each α_δ value at a Re_δ, the A and B matrix are assembled and equation 3.54 is solved using the Matlab EIG function and the most unstable eigenvalue is found and stored at that α_δ and Re_δ coordinate. Finally, using the Matlab contour plot the neutral curves are drawn.

3.4 Orr-Sommerfeld Equation Numerical Solution Algorithm

Figure 3.1 shows a flow chart of the procedure used to perform the Orr-Sommerfeld numerical solution.

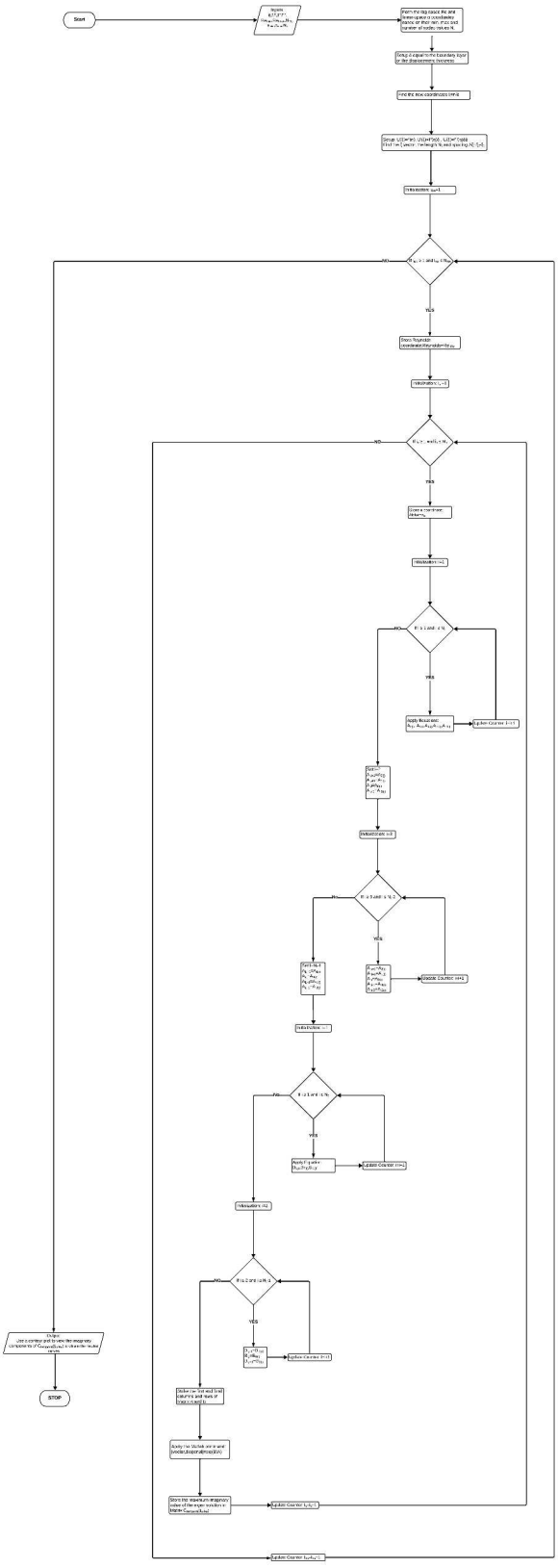

Figure 3.1: Orr-Sommerfeld incompressible flow simulation flow chart.

3.5 Orr-Sommerfeld Equation Neutral Curves

According to (White, F. M. 1991), viscous theories predict a finite region at low Reynolds where infinitesimal disturbances are amplified. This happens when the imaginary component of the wave speed is greater than zero. The boundary of this region where this starts to happen is called the neutral curve. Figure 3.2 shows the neutral graph of a thumb curve for the Blasius velocity profile. One of the most important parameters of this curve is the $Re_{critical}$ or critical Reynolds number. The $Re_{critical}$ is the smallest Reynolds number at which the disturbance can be amplified (when the flow start to change from laminar to transitional flow). This number can be found by locating the minimal or leftmost coordinate Re in Figure 3.2. Its important to mention that the boundary of this neutral curve is located at the section where the wave propagation speed imaginary component is zero. In the case of the temporal stability solution, every region outside the neutral curve is considered stable and everything inside is considered unstable. So, the objective is to manipulate the flow so that the curve decreases its unstable area and increases its critical Reynolds number.

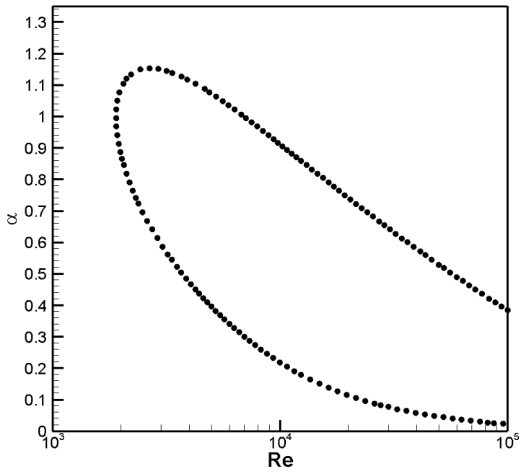

Figure 3.2: Typical neutral curve from the Blasius velocity profile.

3.6 Compressible Flow Stability

Compressible flow couples the pressure to temperature through the equations of state. In the stability analysis, the fluctuations of density, viscosity, thermal conductivity, specific heat at constant pressure and temperature must be accounted for, as well as the fluctuations of the velocity in the x, y, and z directions and pressure. This increases the complexity of the stability analysis, which results in a sixth order differential equation. Also, as shown in the previous sections, the disturbance is modeled as a traveling wave (White, F. M. 1991). Figure 3.3 shows an example of a compressible flow neutral stability curve for the first mode ($n = 1$) and the second mode ($n = 2$). It can be seen in the figure that for Mach numbers beyond Mach 0.3 or 0.37 a higher mode appears (second mode). It is also observed that as the Mach number increases, the modes start to merge and according to (White, F. M. 1991) the modes become indistinguishable at Mach 7. In

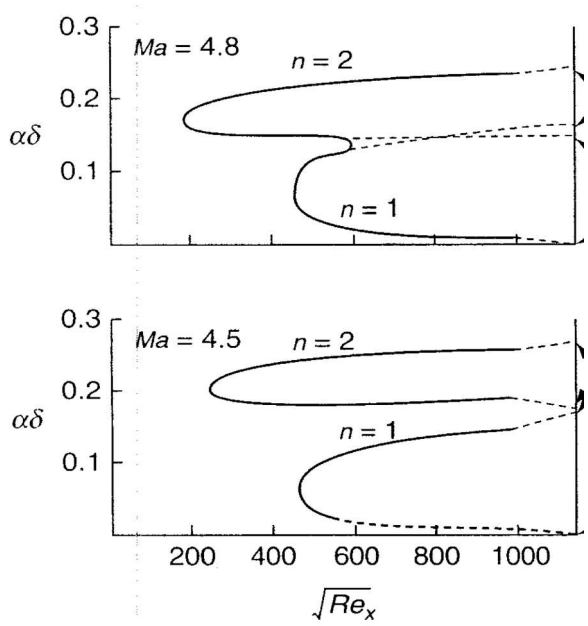

Figure 3.3: Neutral Stability Curves examples for the first n=1 and second n=2 modes. Reproduced faithfully from (White, F. M. 1991).

compressible flows, Squires' theorem is no longer valid because the most unstable wave does not align with the free stream direction. Additionally, at high Mach numbers, while the viscous and conduction terms can be approximated within a two-dimensional system, the dissipation terms cannot be transformed in the same manner. It is important to note, however, that for compressible flow, Squires' theorem remains valid up to Mach 0.7 for the first mode, while the second mode fully satisfies the conditions of the theorem

(White, F. M. 1991).

3.7 Thermal Orr-Sommerfeld Equation with Variable Flow Properties

To derive the Orr-Sommerfeld equation for thermal flow or for flows with variable viscosity, the momentum equations are coupled with the energy equations via the equations of state. The Navier-Stokes (NS) equations are solved simultaneously with the energy equations to account for these coupled effects. Additionally, the same assumptions as in the previous sections are applied, with the key difference that the fluid properties now vary as a function of temperature.

The Navier Stokes equations can be written as (White, F. M. 1991; Cengel, Y. A. and Cimbala, J. M. 2014; Cengel, Y. A. and Ghajar, A. J. 2015; Ozgen, S. 2004; Ozgen, S. and Kircah, S. A. 2008):

•Continuity:

$$\frac{\partial(\rho u)}{\partial x} + \frac{\partial(\rho v)}{\partial y} = 0 \tag{3.55}$$

•X-Momentum:

$$\frac{\partial u}{\partial t} + u\frac{\partial u}{\partial x} + v\frac{\partial u}{\partial y} = \frac{-1}{\rho}\frac{\partial P}{\partial x} + \frac{1}{\rho}\frac{\partial}{\partial x}\left[2\mu\frac{\partial u}{\partial x}\right] + \frac{1}{\rho}\frac{\partial}{\partial y}\left[\mu\left(\frac{\partial u}{\partial y} + \frac{\partial v}{\partial x}\right)\right] \tag{3.56}$$

•Y-Momentum:

$$\frac{\partial v}{\partial t} + u\frac{\partial v}{\partial x} + v\frac{\partial v}{\partial y} = \frac{-1}{\rho}\frac{\partial P}{\partial y} + \frac{1}{\rho}\frac{\partial}{\partial x}\left[\mu\left(\frac{\partial u}{\partial y} + \frac{\partial v}{\partial x}\right)\right] + \frac{1}{\rho}\frac{\partial}{\partial y}\left[2\mu\frac{\partial v}{\partial y}\right] \tag{3.57}$$

•Energy:

$$\rho C_p\left[\frac{\partial T}{\partial t}+u\frac{\partial T}{\partial x}+v\frac{\partial T}{\partial y}\right]=-P\left(\frac{\partial u}{\partial x}+\frac{\partial v}{\partial y}\right)+\frac{\partial}{\partial x}\left(k\frac{\partial T}{\partial x}\right)+\frac{\partial}{\partial y}\left(k\frac{\partial T}{\partial y}\right)+\mu\Phi \tag{3.58}$$

Where Φ is the viscous dissipation term:

$$\Phi=2\left[\left(\frac{\partial u}{\partial x}\right)^2+\left(\frac{\partial v}{\partial y}\right)^2\right]-\frac{2}{3}\left(\frac{\partial u}{\partial x}+\frac{\partial v}{\partial y}\right)^2+\left(\frac{\partial v}{\partial x}+\frac{\partial u}{\partial y}\right)^2 \tag{3.59}$$

•Viscosity Power law:

$$\mu=\mu_{ref}\left(\frac{T}{T_{ref}}\right)^n \tag{3.60}$$

Where n is the Power law parameter. For air, $n=0.76$.

•Density:

$$\rho=\rho_{ref}\frac{T_{ref}}{T} \tag{3.61}$$

Note: Prandtl number remains constant.

According to (Wazzan, A. R., Okamura, T. and Smith, A. M. O. 1968; Ozgen, S. 2004) the Navier Stokes compressible flow equations can be solved in a way in which the effect of temperature on μ, Pr and ρ is accounted for in the stability analysis. This can be done by adding a disturbance to equations 3.55, 3.56, 3.57 and 3.58 based on the u, v, P and T flow parameters and flow properties, which yields a sixth order differential equation. On the other hand, considerable simplifications can be done if the disturbance is added to equations 3.55, 3.56 and 3.57 based on the u, v and P parameters and the flow properties of μ and ρ remain state variables which yields a fourth order differential equation known as the Thermal Orr-Sommerfeld equation for variable flow properties:

$$\begin{aligned}&(U^*-c^*)(\phi''-\alpha_\delta^2\phi)-U^{*''}\phi+\frac{i}{\alpha_\delta Re}[\mu(\phi''''-2\alpha_\delta^2\phi''+\alpha_\delta^4\phi)\\&+2\mu'(\phi'''-\alpha_\delta^2\phi')+\mu''(\phi''+\alpha_\delta^2\phi)]=0\end{aligned} \tag{3.62}$$

Where ϕ, U^*, c^*, α_δ and Re are given by equations 3.31, 3.32, 3.33, 3.34, and 3.35. In this case, μ is given by the Power Law (equation 3.60). It is important to mention that equation 3.62 will not show the secondary modes due to the fact that the fluctuations of temperature are not accounted for, which have an effect on the eigenvalue calculations, but equation 3.62 still can be used to obtain a general idea to what happens to the flow stability (if it increases or not) as the Mach number changes or the wall gets cold or hot.

Equation 3.62 can be obtained by performing a similar procedure to 3.4 by adding a disturbance equation to equations 3.55, 3.56 and 3.57 based on u, v and P flow parameters and by making μ and ρ state variables of the flow properties in the analysis. Rearranging equation 3.62 so the c^* terms are in the right side and the non c^* terms are in the left side yields:

$$a_1\phi^{''''} + a_2\phi^{'''} + a_3\phi^{''} + a_4\phi^{'} + a_5\phi = c^*(b_1\phi^{''} - b_2\phi) \tag{3.63}$$

Where:

$$a_1 = \mu i \tag{3.64}$$

$$a_2 = 2\mu^{'} i \tag{3.65}$$

$$a_3 = \alpha_\delta Re_\delta U^* - 2\mu\alpha_\delta^2 i + \mu^{''} i \tag{3.66}$$

$$a_4 = -2\mu^{'}\alpha_\delta^2 i \tag{3.67}$$

$$a_5 = -\alpha_\delta^3 Re_\delta U^* - \alpha_\delta Re_\delta U^{*''} + \mu\alpha_\delta^4 i + \mu^{''}\alpha_\delta^2 i \tag{3.68}$$

$$b_1 = \alpha_\delta Re_\delta \tag{3.69}$$

$$b_2 = \alpha_\delta^3 Re_\delta \tag{3.70}$$

$$i = \sqrt{-1} \tag{3.71}$$

Applying a finite difference transformation to equation 3.63 yields the following:

$$A_2\phi_{i+2} + A_1\phi_{i+1} + A_0\phi_i + A_{-1}\phi_{i-1} + A_{-2}\phi_{i-2} = c^*[B_1\phi_{i+1} + B_0\phi_i + B_{-1}\phi_{i-1}] \tag{3.72}$$

$$A_2 = 2a_1 + a_2\Delta\xi \tag{3.73}$$

$$A_1 = -8a_1 - 2a_2\Delta\xi + 2a_3\Delta\xi^2 + a_4\Delta\xi^3 \tag{3.74}$$

$$A_0 = 12a_1 - 4a_3\Delta\xi^2 + 2a_5\Delta\xi^4 \tag{3.75}$$

$$A_{-1} = -8a_1 + 2a_2\Delta\xi + 2a_3\Delta\xi^2 - a_4\Delta\xi^3 \tag{3.76}$$

$$A_{-2} = 2a_1 - a_2\Delta\xi \tag{3.77}$$

$$B_1 = 2b_2\Delta\xi^2 \tag{3.78}$$

$$B_0 = (-1)(4b_1\Delta\xi^2 + 2b_2\Delta\xi^4) \tag{3.79}$$

$$B_{-1} = 2b_2\Delta\xi^2 \tag{3.80}$$

Note: In equation 3.72, i is a counter and not the operator $\sqrt{-1}$.

As observed before, it can be seen from equation 3.72 and 3.53 that matrix A is a pentadiagonal matrix and matrix B is a tridiagonal matrix. To obtain the complex value

c^* the equation 3.54 is used. The algorithm used to solve equation 3.72 is the same used in Section 3.4 with the difference that here the variation of viscosity is taken into account in the Orr-Sommerfeld equation with the change in variable ξ.

Chapter 4
Incompressible boundary layers subject to wall curvature and passive scalar transport

4.1 Curved Surface Boundary Layer Theory

As previously mentioned, the Navier-Stokes (NS) equations are fundamental to modern fluid dynamics theory (White, F. M. 1991; Cengel, Y. A. and Cimbala, J. M. 2014). These equations describe the transport phenomena of momentum and the associated velocity-pressure field. When coupled with the energy equation, the NS equations provide a comprehensive framework for modeling flow, including the effects of wall heating and cooling. However, due to their inherent complexity and high nonlinearity, obtaining analytical solutions to the NS equations is often impractical. Nonetheless, several analytical (or quasi-analytical) solutions exist for specific cases, such as the Couette, Poiseuille, and Boundary Layer problems, which are derived under simplifying assumptions typically applied to laminar flows. These assumptions considerably reduce the complexity of the NS equations. The boundary layer theory, for example, assumes that the velocity component parallel to the wall is significantly larger than the wall-normal velocity component. Additionally, it is assumed that the pressure gradient perpendicular to the wall remains constant, and that wall-normal flow gradients dominate over streamwise flow gradients (White, F. M. 1991; Cengel, Y. A. and Cimbala, J. M. 2014; Cengel, Y. A. and Ghajar, A. J. 2015). By applying Prandtl's assumptions, the NS equations are simplified to the boundary layer equations, which can be further solved using similarity analysis techniques. In Boundary Layer theory, a more general solution is that of a curved surface, which in the end can be approximated to a flat plate surface by prescribing an infinite curvature radius. As seen in Figure 4.1, the x coordinate is parallel to the surface and the y coordinate is perpendicular to the local surface. The parameter Λ is defined as $1/R$ (R being the radius of the curvature) and is called the surface curvature. Finally, the

corresponding Boundary Layer equations can be reduced to a one-dimensional problem with a fourth-order ODE via a similarity analysis. In addition, it can be seen in Figure 4.1 the velocity component parallel to the wall, u, and the wall-normal component v (White, F. M. 1991; Murphy, J. S. 1965). For the thermal transport equation (energy equation), the dissipation term must be taken into account in high-speed flows and very high-viscous fluids, as well as the variation of fluid viscosity and density (via the state equation). For moderate and low viscous incompressible flows, the dissipation term can be neglected. In the case of incompressible flows, the energy equation is decoupled from the momentum equation, and buoyancy effects are neglected. Therefore, a similar procedure to that of the momentum equations can be applied to the energy equation to obtain the passive scalar transport equation by applying the Prandtl assumptions, and eventually, a similarity solution can be obtained for laminar thermal boundary layers. As stated before, this similarity solution is a second-order linear ODE which is solved after knowing the similarity stream function parameter distribution (White, F. M. 1991; Cengel, Y. A. and Ghajar, A. J. 2015). The transport of passive scalars is critical in many industrial applications of technological importance, such as in turbine-blade film cooling, heat transfer in electronic/mechanical devices, chemicals dissolved in gases, contaminant/humidity dispersed in atmospheric flow, to name a few. Furthermore, a passive scalar is defined as a diffusive contaminant that exists at such a low concentration in a flow that it has no effect on the dynamics of fluid motion, (Warhaft 2000). However, that low concentration of passive scalar is sufficient to cause a significant impact on energy expenditures, air pollution, and the design of chemical processes.

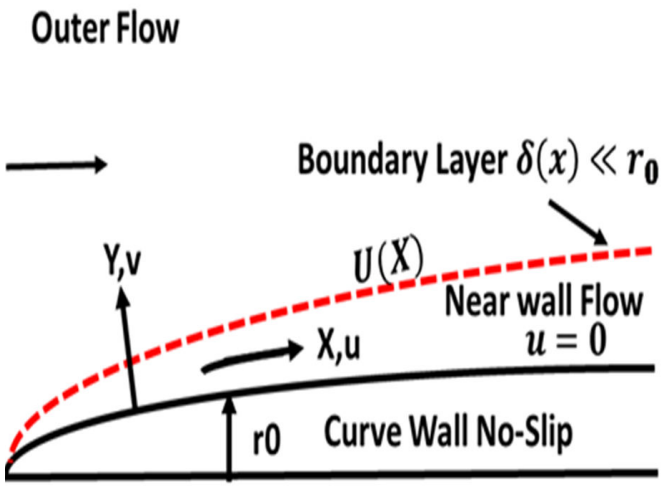

Figure 4.1: Curved surface coordinate setup.

The primary challenge when solving for flow over curved surfaces lies in the need to

account for the curvature of the geometry within the boundary layer. This is because the centrifugal forces induced by the curvature influence the wall-normal pressure gradient. As a result, the curvature of the surface has a significant impact on the boundary layer behavior, unlike the case of a flat plate, where such effects are absent. Thus, the curvature must be incorporated into the analysis to accurately capture the flow dynamics.

4.2 Curved Surface Navier Stokes Equations

According to (Goldstein, S. 1938), the NS governing equations for curved surfaces are as follows:

- Continuity:

$$\frac{\partial u}{\partial x} + \frac{\partial}{\partial y}(1+\Lambda y)v = 0 \tag{4.1}$$

- X-Momentum:

$$\begin{aligned}
&\frac{\partial u}{\partial t} + \frac{u}{1+\Lambda y}\frac{\partial u}{\partial x} + v\frac{\partial u}{\partial y} + \frac{\Lambda uv}{1+\Lambda y} = \frac{-1}{\rho(1+\Lambda y)}\frac{\partial P}{\partial x} \\
&+\nu\left[\frac{1}{(1+\Lambda y)^2}\frac{\partial^2 u}{\partial x^2} + \frac{\partial^2 u}{\partial y^2} - \frac{y}{(1+\Lambda y)^3}\frac{\partial \Lambda}{\partial x}\frac{\partial u}{\partial x} + \frac{\Lambda}{1+\Lambda y}\frac{\partial u}{\partial y}\right. \\
&\left.-\frac{\Lambda^2 u}{(1+\Lambda y)^2} + \frac{2\Lambda}{(1+\Lambda y)^2}\frac{\partial v}{\partial x} + \frac{v}{(1+\Lambda y)^3}\frac{\partial \Lambda}{\partial x}\right]
\end{aligned} \tag{4.2}$$

- Y-Momentum:

$$\begin{aligned}
&\frac{\partial v}{\partial t} + \frac{u}{1+\Lambda y}\frac{\partial v}{\partial x} + v\frac{\partial v}{\partial y} - \frac{\Lambda u^2}{1+\Lambda y} = \frac{-1}{\rho}\frac{\partial P}{\partial y} \\
&+\nu\left[\frac{1}{(1+\Lambda y)^2}\frac{\partial^2 v}{\partial x^2} + \frac{\partial^2 v}{\partial y^2} - \frac{y}{(1+\Lambda y)^3}\frac{\partial \Lambda}{\partial x}\frac{\partial v}{\partial x} + \frac{\Lambda}{1+\Lambda y}\frac{\partial v}{\partial y}\right. \\
&\left.-\frac{\Lambda^2 v}{(1+\Lambda y)^2} - \frac{u}{(1+\Lambda y)^3}\frac{\partial \Lambda}{\partial x} - \frac{2\Lambda}{(1+\Lambda y)^2}\frac{\partial u}{\partial x}\right]
\end{aligned} \tag{4.3}$$

According to (Schlichting, H. and Gersten, K. 2017; Cengel, Y. A. and Ghajar, A. J. 2015), the energy equation for an incompressible flow is given as:

$$\rho C_p\left[\frac{\partial T}{\partial t}+\frac{u}{1+\Lambda y}\frac{\partial T}{\partial x}+v\frac{\partial T}{\partial y}\right]=\frac{1}{1+\Lambda y}\frac{\partial}{\partial x}\left[\frac{K}{1+\Lambda y}\frac{\partial T}{\partial x}\right]+\frac{\partial}{\partial y}\left[K\frac{\partial T}{\partial y}\right] \tag{4.4}$$

4.3 Curved Surface Boundary Layer Equations

Applying the boundary layer assumptions stated in sections 1.1 and 4.1 to equations 4.1, 4.2, 4.3 and 4.4 the NS equations for a curved surface reduces to:

- Continuity:

$$\frac{\partial u}{\partial x}+\frac{\partial v}{\partial y}=0 \tag{4.5}$$

- X-Momentum:

$$u\frac{\partial u}{\partial x}+v\frac{\partial u}{\partial y}+\Lambda uv=\frac{-1}{\rho}\frac{\partial P}{\partial x}+\nu\left[\frac{\partial^2 u}{\partial y^2}+\Lambda\frac{\partial u}{\partial y}\right] \tag{4.6}$$

- Y-Momentum:

$$\Lambda u^2=\frac{1}{\rho}\frac{\partial P}{\partial y} \tag{4.7}$$

- Energy:

$$u\frac{\partial T}{\partial x}+v\frac{\partial T}{\partial y}=\frac{\nu}{Pr}\frac{\partial^2 T}{\partial y^2} \tag{4.8}$$

4.4 Curved Surface Boundary Layer Similarity Equations

According to (Murphy, J. S. 1965), applying a similarity analysis to equations 4.5, 4.6, 4.7 and 4.8 yield the following fourth order similarity solution:

$$f''''+ff'''+\Omega[f'''+ff'']-\gamma[f'f''+\Omega f'f']=0 \tag{4.9}$$

For the Curved surface case the boundary conditions are:

$$\eta = 0; f = f^{'} = 0 \tag{4.10}$$

$$\eta \to \infty; f^{'} = e^{-\Omega\eta}; f^{''} = -\Omega e^{-\Omega\eta} \tag{4.11}$$

It is important to note that, in this analysis, f is associated to the stream function, $f^{'}$ is related to the stream-wise x-velocity (parallel to the surface) and $f^{''}$ is related to the local shear stress inside the boundary layer. The similarity variable used to normalize x and y is given as:

$$\eta = y\sqrt{\frac{(m+1)}{2}\frac{U_0}{\nu x}} \tag{4.12}$$

The power parameter is defined as:

$$m = \frac{\gamma + 1}{3 - \gamma} \tag{4.13}$$

The curvature parameters is:

$$\Lambda = \Omega\sqrt{\frac{(m+1)}{2}\frac{U_0}{\nu x}} \tag{4.14}$$

The potential velocity U_0 at the surface is:

$$U_0 = U_\infty C_2^{(m+1)/2}\left[\frac{2}{m+1}\frac{x}{L}\right]^m \tag{4.15}$$

Were C_2 is a constant.

The pressure gradient is defined as:

$$\gamma = 2\beta - 1 \tag{4.16}$$

Here β is the Falkner Skan pressure gradient parameter. Applying a similar analysis as in (White, F. M. 1991; Cengel, Y. A. and Ghajar, A. J. 2015), now the similarity passive scalar equation is expressed as:

$$g^{''} + Prg^{'}f = 0 \tag{4.17}$$

The boundary conditions of the passive scalar equation read:

$$\eta = 0; g = 1 \tag{4.18}$$

$$\eta \to \infty; g = 0 \tag{4.19}$$

The similarity variable used to normalize the passive scalar (temperature will be considered here as a passive scalar) is given as:

$$g(\eta) = \frac{T - T_e}{T_w - T_e} \tag{4.20}$$

Where T is the local dimensional temperature in the boundary layer, T_w is the prescribed wall temperature, and T_e is the temperature at the edge of the boundary layer (freestream).

The integral boundary layer parameters are defined as follows:

$$\Delta^* = \int_0^\infty \left[1 - \frac{f'}{e^{-\Omega\eta}}\right] d\eta \tag{4.21}$$

$$\theta^* = \int_0^\infty \left[\frac{f'}{e^{-\Omega\eta}}\right]\left[1 - \frac{f'}{e^{-\Omega\eta}}\right] d\eta \tag{4.22}$$

$$H = \frac{\Delta^*}{\theta^*} \tag{4.23}$$

Where Δ^* is the displacement thickness, θ^* is the momentum thickness and H is the shape factor.

Note: The prime indicates differentiation with respect to η. For additional details, readers are referred to (Ramirez, M. A. and Araya, G. 2022).

4.5 Boundary Layer Curved Surface Numerical Solution

The employed method is called the "point and shoot" algorithm. This algorithm works as follows:

• The f'' and f''' are guessed on the curvature surface (i.e., at $\eta = 0$). It is worth mentioning that f'' is proportional to the first derivative of u and consequently to wall shear stress; while f''' is proportional to the second derivative of u. In this case, u is the curvature velocity profile.

• A Runge-Kutta fourth order methodology is applied to numerically compute equation 4.9.

• The resulting outcomes of f' and f'' are compared with the corresponding boundary conditions (equation 4.11) well outside the boundary layer, following an iterative procedure.

In the shooting method algorithm for equation 4.9 the value of $f''(0)$ on the wall was obtained by equation 4.24, 4.25, 4.26, and 4.27. An increment function was made to change the guesses of $f'''(0)$ with an increment of $1 * 10^{-5}$, which was used to solve equation 4.9 via a Runge-Kutta fourth-order Algorithm. Once equation 4.9 was solved, the final value f' was compared to the value of the potential function of f' as η tends to infinity until it reaches a tolerance of $1 * 10^{-8}$. It is important to mention that as the value f' approaches the value of the potential function of f', the increment decreased to $1 * 10^{-11}$. In the case of the energy equation (equation 4.17) a similar procedure was used. For the energy equation, an increment function was used to change the values of $g'(0)$ on the wall with an increment of $1 * 10^{-5}$ and was decreased to a value of $1 * 10^{-11}$ as the last values of g reach zero. Furthermore, the stop condition as $\eta \to \infty$ for g was set with a tolerance of $1 * 10^{-8}$.

The displacement and momentum thickness (Equations 4.21 and 4.22) can be obtained via numerical integration by using a Simpson algorithm.

The following linear approximations were used to estimate $f''(0)$ based on Figure 4.3 and Figure 4 of (Murphy, J. S. 1965) for β equal to 1, 0.2, 0, and -0.1, respectively:

$$f''(0) = -1.6426\Omega + 1.2302 \tag{4.24}$$

$$f''(0) = -1.3003\Omega + 0.6861 \tag{4.25}$$

$$f''(0) = -1.0189\Omega + 0.4693 \tag{4.26}$$

$$f''(0) = -0.7359\Omega + 0.319 \tag{4.27}$$

The energy or passive scalar equation (equation 4.17) can be solved by applying the previously described Runge-Kutta fourth-order algorithm on the passive scalar field and by assuming that the values of f (stream function distribution) are known. In this case, the value of g' must be assumed or guessed in order to satisfy the outer boundary conditions (i.e., for $\eta \to \infty$; g must be zero) which enforces the freestream conditions for the passive scalar and zero normal gradients. Notice that the wall value of g' is proportional to the wall heat flux.

4.6 Curved Surface Boundary Layer Flow Studies

Figure 4.2 shows the grid dependence test carried out on the thermal field g and a comparison with White's results (White, F. M. 1991) by prescribing 1000, 2000 and 4000 nodes in the η direction. The pressure gradient and the curvature parameter were set to 0 (Blasius) with a Prandtl number of 0.1. It can be seen in the figure that all the grid tests are very near or almost coincident with White's results (White, F. M. 1991), which demonstrates a very good precision of the numerical solution for the energy equation. The study shows that all thermal profiles are almost coincident or very near each other, so a number of 1000 can be chosen without impacting numerically the final results, also for the passive scalar field.

Figure 4.3 shows the variation of $f''(0)$ vs Ω for a pressure gradient of 1, 0.2, 0 and -0.1, respectively. The special case at $\beta = 0$ (γ = -1) corresponds to a zero streamline pressure gradient or ZPG, whereas the case at $\beta = 1$ ($\gamma = +1$) represents flow near the nose of a right circular cylinder. The second derivative (f'') of the stream function f is proportional to the local shear stress by friction and consequently to the skin friction coefficient in the boundary layer. It can be seen in Figure 4.3 that as the curvature parameter increases from a negative (concave) to a positive (convex) value, the wall

shear stress decreases linearly. This decreasing linear slope is steepest for the largest pressure gradient parameter, i.e. $\beta = 1$. Therefore, and consistent with (Murphy, J. S. 1965), the wall curvature has almost negligible effects on the wall shear stress in flows with significant APG (note trend at β = -0.1). In contrast, the influence of the curvature is more evident for flows with a very strong FPG (see $\beta = +1$). Notice that when the curvature parameter Ω is zero, the solution is that of the Falkner-Skan flow for a flat plate. For a constant curvature parameter and as the pressure gradient β increases in Figure 4.3, the wall shear stress increases as well. Readers are referred to (Ramirez, M. A. and Araya, G. 2022) for additional details.

Figure 4.4 shows the variation of g (normalized temperature) vs. η for a pressure gradient, $\beta = 0.2$, Ω's values of -0.1, 0 and 0.1 and for a Prandtl number of 0.1. As the curvature decreases from a positive (convex) to a negative (concave) value, the curves tend to move to the left, indicating a shrinking process of the thermal boundary layer thickness. Again, for a zero value of the wall curvature Ω, the solution corresponds to a Falkner-Skan flow for a flat plate in a purely accelerated flow.

Figure 4.5 shows the effects of streamwise pressure gradient (β = 1, 0.2, 0, -0.1) on the normalized temperature g for a fixed wall concave curvature (Ω = -0.1). The effect of the pressure gradient is weak compared to the effect of the wall curvature in Figure 4.4. In the figure a modest thickening process of the thermal boundary layer thickness can be seen as the pressure gradient becomes more adverse (i.e., for APG). It can also be

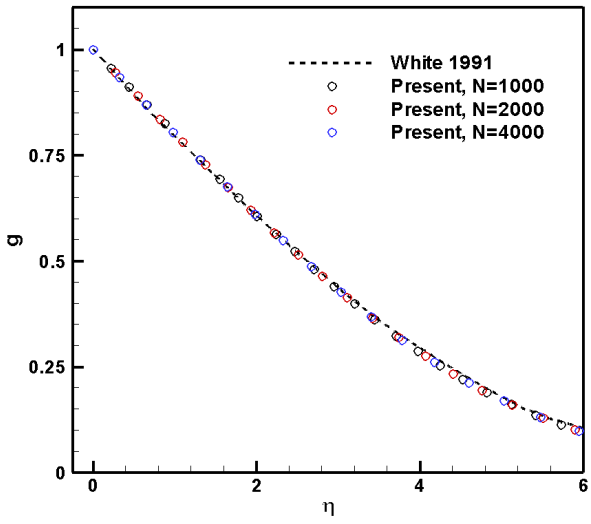

Figure 4.2: g Grid dependence test for 1000, 2000, and 4000 grid points, and comparison with White (White, F. M. 1991). For $\beta = 0$, $\Omega = 0$ and Pr = 0.1.

observed that all the g curves for all pressure gradients tend to zero beyond the boundary layer thickness since the temperature of the free stream is equal to that of the outer flow.

Figure 4.6 shows the variation of $g^{'}(0)$ (normalized wall heat flux) vs. wall curvature (Ω) at different pressure gradients (i.e., β = 1, 0.2, 0 and -0.1). The first derivative ($g^{'}$) is proportional to the local heat flux in the thermal boundary layer. It can be seen in the figure that as the curvature parameter decreases from a positive (convex) to a negative

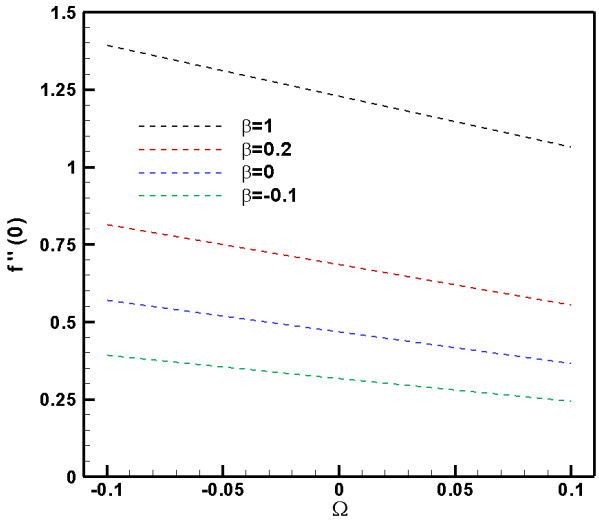

Figure 4.3: f'' (normalized wall shear stress) vs η for β = 1, 0.2, 0 and -0.1.

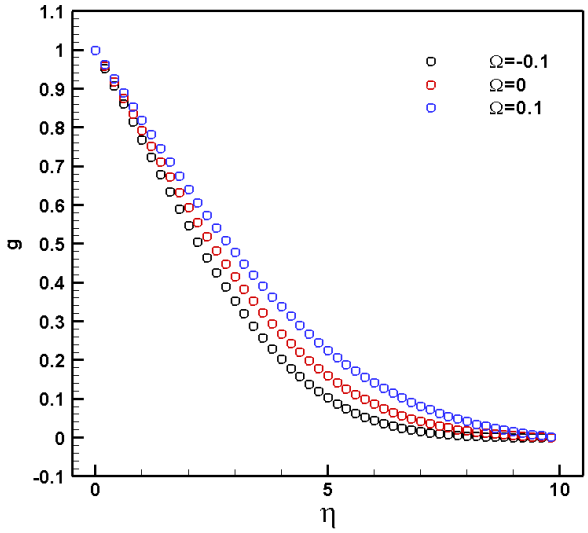

Figure 4.4: g vs η for β = 0.2, Ω = -0.1, 0 and -0.1 and Pr=0.1.

(concave) value, the heat flux at the wall increases in a negative sense. Consequently, the Reynolds analogy is satisfied between the normalized wall shear stress and wall heat flux. For a constant wall curvature, the increase in normalized wall heat flux between a very strong APG flow ($\beta = -0.1$) in contrast to a very strong FPG flow ($\beta = 1$) is of the order of 15%.

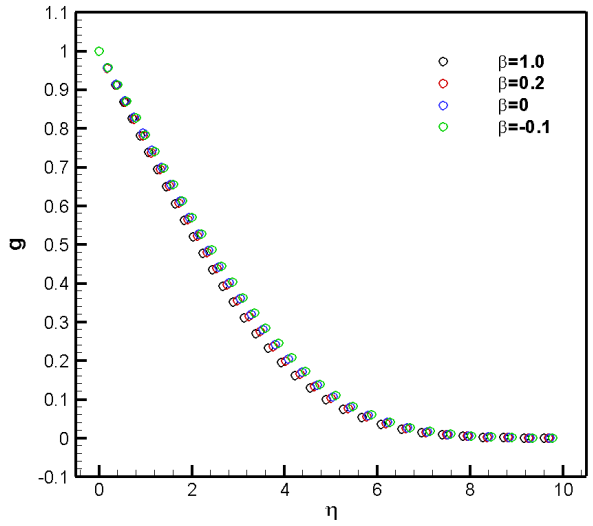

Figure 4.5: g vs. η for β = 1, 0.2, 0 and -0.1, Ω = -0.1 and Pr = 0.1.

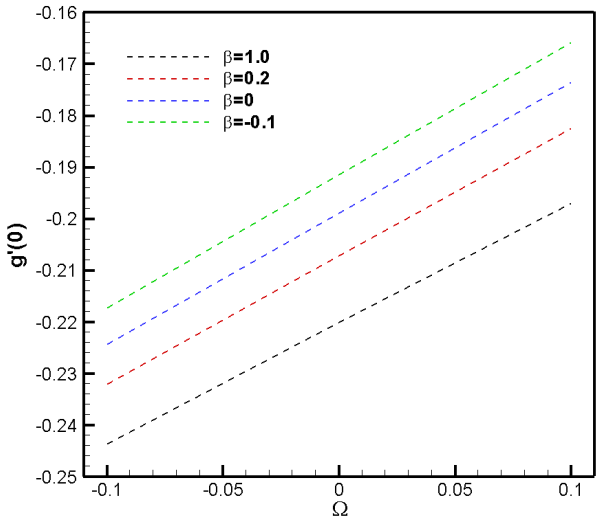

Figure 4.6: $g^{'}(0)$ vs Ω for β = 1, 0.2, 0 and -0.1, Pr = 0.1.

Figure 4.7 shows the influence of different Prandtl numbers(i.e., Pr = 0.1, 0.4, 0.72, 1 and 5) on the thermal boundary layer temperature distribution for a pressure gradient of 0.2 and Ω of -0.1. It can be observed in the figure that larger values of the Prandtl number cause a significant decrease in the thermal boundary thickness. For the considered range of Prandtl numbers, a four-fold variation of the thermal boundary layer thickness was observed.

Figure 4.8 shows the variation of the wall heat flux as the Prandtl number changes for a pressure gradient of 0.2 and Ω of -0.1. It can be seen in the figure that there is an increase on the absolute value of the normalized wall heat flux at larger Prandtl numbers. This is consistent with the shrinking process of the thermal boundary layer thickness as Pr increases, since the thermal variation between the wall and the freestream must occur in a thinner layer and thus the wall thermal gradient must intensify.

4.7 Particular Case: Zero Wall Curvature (Flat Plate)

Figure 4.9 shows the distribution f'', f', and f vs. η comparison between the present result and the one detailed in Whites (White, F. M. 1991) for a flat plate. The figure shows a typical flat plate Blasius result for incompressible flow. It can be seen that f''(related to shear stress) starts with the guess value on the wall (0.4696) and as it gets

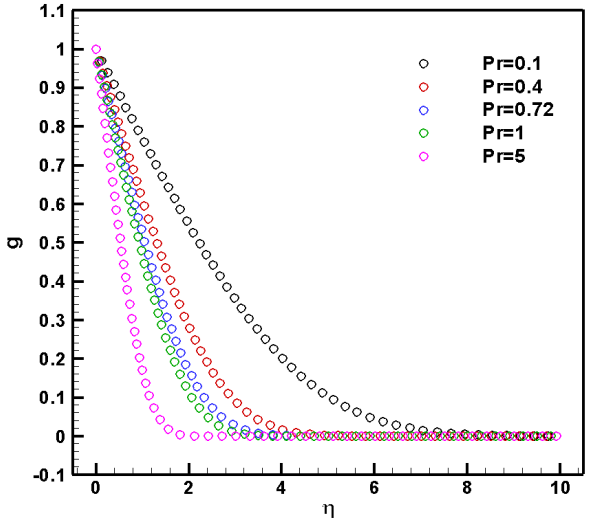

Figure 4.7: g vs η for $\beta = 0.2$, Ω = -0.1 and Pr = 0.1, 0.4, 0.72, 1 and 5.

farther from the wall it decreases until it reaches a value of zero at the free stream. The f' parameter (related to the fluid flow velocity) starts at zero on the wall due to the no-slip condition and as it gets farther from the wall increases until it reaches a value of 1 at the free stream, meaning that the flow velocity is equal to that of the free stream. As can be seen, the f'', f' and the f show to have a very good agreement with White's data, as expected.

Figure 4.10 shows the incompressible f' distribution vs. η comparison between the present result and the one detailed in Whites (White, F. M. 1991) for a β between -0.1988 and 1. The figure shows that as β decreases, the curve tends to become more S-shaped. This happens because as β decreases, the flow enters an expansion and the pressure gradient becomes adverse as it decelerates, leading to a flow separation. In addition, it is observed that as β increases, the flow enters a favorable pressure gradient and accelerates, decreasing the thickness of the boundary layer. It is important to mention that the present data shows to have a very good agreement with White's data.

Figure 4.11 shows the incompressible f'' distribution vs. η of the present result for β between -0.1988 and 1.5. The figure shows that as β decreases, the wall shear stress or $f''(0)$ decreases until it reaches a value of zero. As stated, before this happens because as the β decreases, the flow enters an expansion and the pressure gradient becomes adverse until the point where the flow separates and the shear stress reaches a value of zero.

Figures 4.12 and 4.13 show the incompressible distributions g and g' vs. η of the present

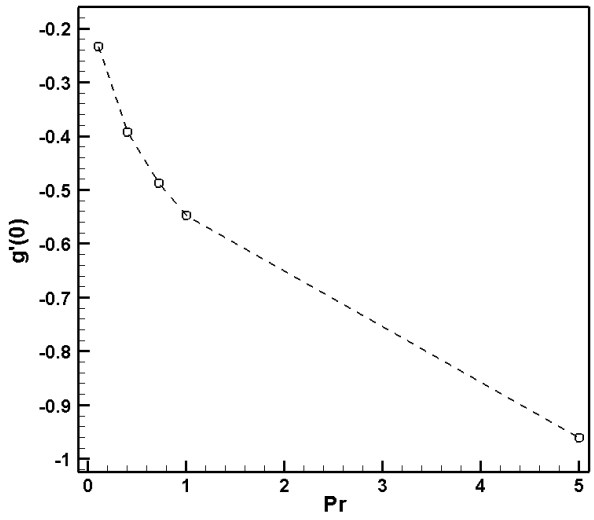

Figure 4.8: $g^{'}(0)$ vs Pr for $\beta = 0.2$ and Ω = -0.1.

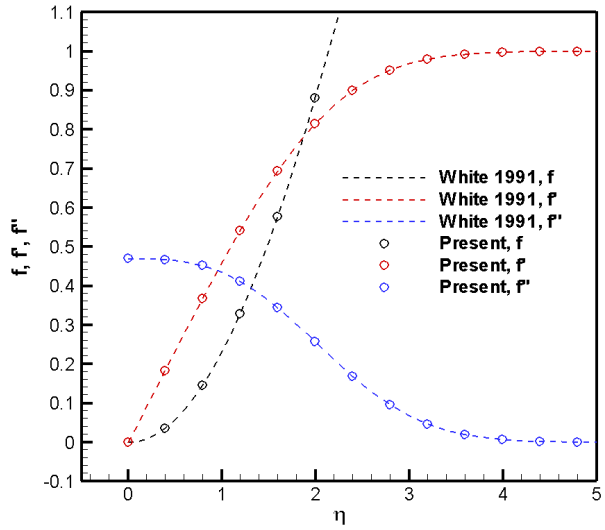

Figure 4.9: f'', f', f vs η comparison with White's data (White, F. M. 1991)

result for a β between -0.1988 and 1.5. It can be seen in the figure that g (related to the temperature) starts at a value of 1 at the wall and decreases until it reaches an infinite value of zero where the local temperature is equal to the free stream temperature; and for g' (related to the heat flux) it is observed that it starts with a high heat flux at the wall, and decreases until it reaches an infinite value of zero where there is no more heat transfer because the local temperature is equal to that of the free stream. It is observed that as β increases, the thickness of the thermal boundary layer decreases. Also, it is important to mention that as the β increases, the heat flux at the wall increases due to the fluid friction at the wall.

Figure 4.14 shows the incompressible distributions $\eta_{99\%}$ and $\eta_{T99\%}$ (Momentum and Thermal boundary layer) vs. β. It can be seen in the figure that as β increases, both boundary layers get closer to the wall.

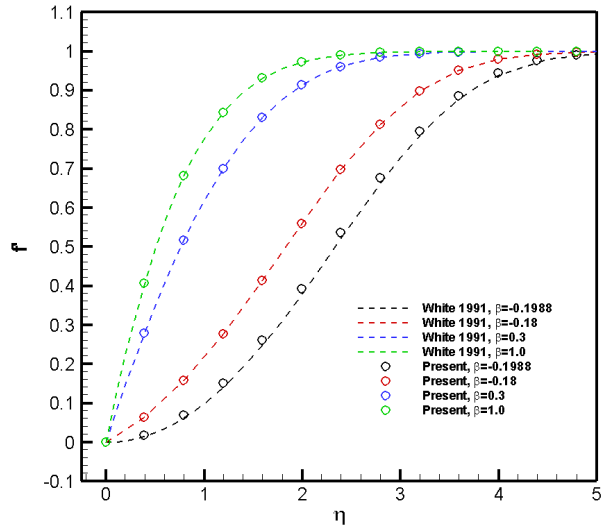

Figure 4.10: f' vs η comparison with White's data (White, F. M. 1991).

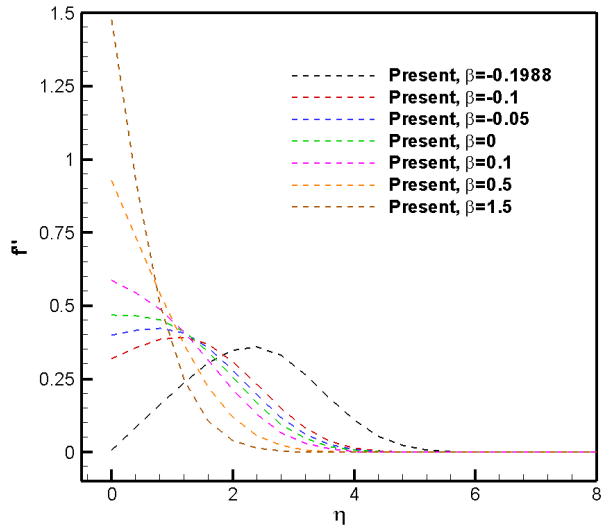

Figure 4.11: f'' vs η for β -0.1988 to 1.5.

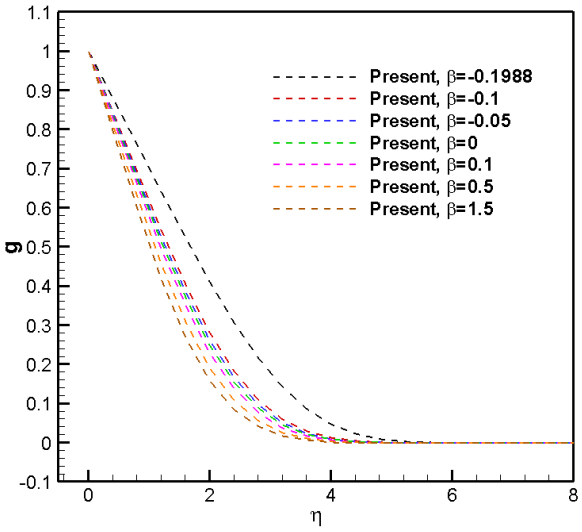

Figure 4.12: g vs η for β -0.1988 to 1.5.

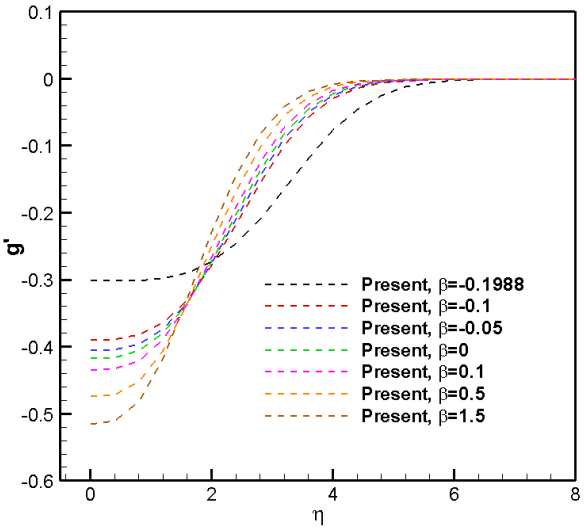

Figure 4.13: g' vs η for β -0.1988 to 1.5.

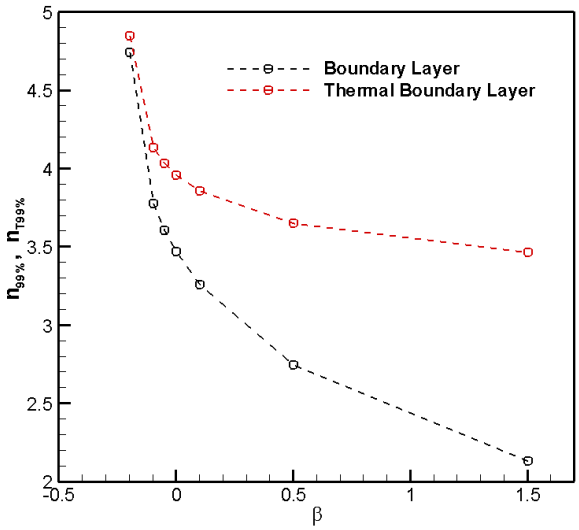

Figure 4.14: Effect of pressure gradient on Momentum and Thermal Boundary Layer thickness

4.8 Chapter 4 Conclusions

The curvilinear similarity solution significantly differs from the flat plate in the sense that the geometry of the wall has to be taken into account, inducing a non-negligible wall normal pressure gradient due to centrifugal forces. For a constant value of the pressure gradient β, it was observed that as the wall curvature parameter (Ω) decreases or becomes negative (i.e., concave) the boundary layer thickness shrinks and the shear stress of the wall increases, consistent with the findings of (Murphy, J. S. 1965). As the pressure gradient β increases from negative (APG) to positive (FPG) values a shrinking process of the boundary layer thickness was observed no matter the curvature type. Normalized wall shear stress (i.e., f'') exhibits a linear decreasing behavior as the wall curvature changes from concave (negative) to convex (positive) at a constant pressure gradient. In terms of the energy equation and temperature regarded as a passive scalar, as the wall curvature decreases from positive (convex) to negative (concave) values, the thermal boundary layer thickness reduces, whereas as the pressure gradient parameter increases, the thermal boundary layer thickness decreases. Furthermore, the influence of β seems to be weaker than that of Ω on passive scalar transport. Since the effects of wall curvature and streamwise pressure gradient on the momentum and thermal boundary layer parameters exhibit similar trends in sign, at least from a qualitative point of view, it can be stated that the Reynolds analogy is somehow satisfied. In terms of the Prandtl number, as the Prandtl number increases, the Thermal Boundary Layer thickness shrinks while the normalized wall heat flux increases. Finally, when the curvature is zero, the solution transforms into the Falkner-Skan equation for a wedge. In this solution, the curvature has a potential function at the free stream equal to unity. It was observed that as the pressure gradient increases, the momentum and thermal boundary layer thickness at the wall decrease. As the pressure gradient increases, the shear stress at the wall increases. The most relevant outcomes of this chapter have been published in (Ramirez, M. A. and Araya, G. 2022).

Chapter 5
Unsteady Incompressible Laminar Boundary Layers

5.1 Unsteady Laminar Boundary Layer

The NS equations are the basis of the fluid mechanics theory. This set of partial differential equations (PDEs) consists of a continuity equation that studies the mass transport, momentum equations that study the flow dynamics, and an energy equation that describes the temporal/spatial evolution of thermal energy. According to the Clay Mathematics Institute (Clay Mathematics Institute), there is not yet an analytical solution to the Navier-Stokes equations, but there are several solutions to this equation based on some assumptions to reduce its complexity. The Prandtl, or boundary layer theory, is the solution of external flow for the Navier-Stokes equation. This solution is achieved by applying the following assumptions to NS (Cengel, Y. A. and Cimbala, J. M. 2014; Cengel, Y. A. and Ghajar, A. J. 2015):

• The velocity component parallel to the wall has a much larger magnitude to that of the wall-normal fluid velocity component.

• The velocity component parallel to the wall has a much larger variation in the direction perpendicular to the wall than the parallel direction.

• The pressure gradients vary in the direction parallel to the wall, and the pressure remains constant (zero pressure gradient) in the direction perpendicular to the wall.

Once these assumptions are applied to the NS equations, the Prandtl or boundary layer equations are obtained. In the present scenario, an unsteady problem is assumed where the effects of time are taken into account. The energy equation for external flow is obtained in a manner similar to the external flow momentum equations by assuming that the variation of temperature in the direction perpendicular to the wall is higher than the

variation parallel to the wall(Cengel, Y. A. and Ghajar, A. J. 2015). It is important to mention that for incompressible flow, buoyancy is neglected, since the variation of the flow properties as the pressure and temperature changes is very small and remains quasi-constant, the energy equation can be decoupled from the momentum equation. This turns the temperature in the energy equation into a passive scalar that does not affect the flow dynamics in the momentum equation (White, F. M. 1991). The Prandtl boundary layer equations can be solved numerically (or semi-analytically) by applying: finite difference, finite volume, and finite element schemes. The unsteady boundary layer equations can be solved via a similarity analysis. This can be done for two cases: flat plate flow, where the changes in pressure are zero (Blasius solution), and a wedge or Falkner-Skan flow, where the changes in pressure can be favorable (FPG) or adverse (APG). Similarity reduces the Prandtl boundary layer theory for these two cases to an unstable third-order differential equation that can be solved by an explicit finite difference scheme (White, F. M. 1991; Cengel, Y. A. and Cimbala, J. M. 2014; Cengel, Y. A. and Ghajar, A. J. 2015). From fluid mechanics theory, the external flow has three phases: laminar, where the flow has an orderly movement, transitional, where the flow changes from laminar to turbulent flow, and turbulent, which is considered a chaotic flow movement. In engineering, it is ideally assumed that the flow changes from laminar to turbulent when the Reynolds number (ratio between inertial to viscous forces) is greater than 500,000 (White, F. M. 1991; Cengel, Y. A. and Cimbala, J. M. 2014). This section involves a surface that is impulsively set in motion at a time of zero. The Prandtl assumptions are applied to the Navier-Stokes equations, which results in an unsteady boundary layer equations. Following the Harris (Harris, S. D., Ingham, D. B. and Pop, I. 2008; Harris, S. D., Ingham, D. B. and Pop, I. 2002) approach for small-time or impulsive flows, a similarity analysis can be applied to the boundary layer equations, resulting in an unsteady Falkner-Skan system. This Falkner-Skan system is obtained by normalizing the stream-wise (x), wall-normal (y) and time (t) coordinates by a variable η and τ. Finally, as time increases, the momentum and thermal boundary layer increase until they reach a steady-state condition. In the present study, the influence of the Prandtl number on the time evolution of the local Nusselt number is analyzed for Pr = 0.1, 0.2, 0.71, 2, 5, and 10.

5.2 Unsteady Boundary Layer Governing Equations

The unsteady boundary layer equations are as follows:

- Continuity:

$$\frac{\partial u}{\partial x} + \frac{\partial v}{\partial y} = 0 \tag{5.1}$$

- Momentum:

$$\frac{\partial u}{\partial t} + u\frac{\partial u}{\partial x} + v\frac{\partial u}{\partial y} = U_e\frac{\partial U_e}{\partial x} + \nu\frac{\partial^2 u}{\partial y^2} \tag{5.2}$$

- Energy:

$$\frac{\partial T}{\partial t} + u\frac{\partial T}{\partial x} + v\frac{\partial T}{\partial y} = \frac{\nu}{Pr}\frac{\partial^2 T}{\partial y^2} \tag{5.3}$$

5.3 Unsteady Boundary Layer Similarity Equations

According to Harris et al. (Harris, S. D., Ingham, D. B. and Pop, I. 2008; Harris, S. D., Ingham, D. B. and Pop, I. 2002), a similarity analysis can be applied to reduce the momentum and energy equations (Equations 5.2 and 5.3) to third and second-order differential equations:

- Momentum:

$$\frac{\partial^3 f}{\partial \eta^3} + \left[\frac{m+1}{2}f + (m-1)\tau\frac{\partial f}{\partial \tau}\right]\frac{\partial^2 f}{\partial \eta^2} + m\left[1 - \left(\frac{\partial f}{\partial \eta}\right)^2\right] = \left[1 + (m-1)\tau\frac{\partial f}{\partial \eta}\right]\frac{\partial^2 f}{\partial \eta \partial \tau} \tag{5.4}$$

- Energy with constant wall temperature:

$$\frac{1}{Pr}\frac{\partial^2 g}{\partial \eta^2} + \left[\frac{m+1}{2}f + (m-1)\tau\frac{\partial f}{\partial \tau}\right]\frac{\partial g}{\partial \eta} = \left[1 + (m-1)\tau\frac{\partial f}{\partial \eta}\right]\frac{\partial g}{\partial \tau} \tag{5.5}$$

- Energy with constant heat flux:

$$\frac{1}{Pr}\frac{\partial^2 g}{\partial \eta^2} + \left[\frac{m+1}{2}f + (m-1)\tau\frac{\partial f}{\partial \tau}\right]\frac{\partial g}{\partial \eta} - \frac{1-m}{2}g\frac{\partial f}{\partial \eta} = \left[1 + (m-1)\tau\frac{\partial f}{\partial \eta}\right]\frac{\partial g}{\partial \tau} \tag{5.6}$$

Where in equation 5.4 m is the power law parameter related to the pressure gradient, f is associated with the stream function, f' is associated with the velocity, and f'' is associated with the shear stress. In the case where equations 5.5 and 5.6 g is related to the temperature and g' to the heat flux. The terms η and τ are related to space and

time, respectively.

The transform space and time variables are:

$$\eta = x^{\frac{m-1}{2}} y \tag{5.7}$$

$$\tau = x^{m-1} t \tag{5.8}$$

Where x and y are the dimensional positions parallel and perpendicular to the flow; and t is the time.

The boundary conditions for τ more than or equal to zero are:

• Momentum:

$$f(0, \tau) = 0 \tag{5.9}$$

$$\frac{\partial f}{\partial \eta}(0, \tau) = 0 \tag{5.10}$$

$$\frac{\partial f}{\partial \eta}(\infty, \tau) \to 1 \tag{5.11}$$

• Energy constant wall temperature:

$$g(0, \tau) = 1 \tag{5.12}$$

$$g(\infty, \tau) \to 0 \tag{5.13}$$

• Energy constant wall heat flux:

$$\frac{\partial g}{\partial \eta}(0, \tau) = -1 \tag{5.14}$$

$$g(\infty, \tau) \rightarrow 0 \tag{5.15}$$

Harris *et al.* (Harris, S. D., Ingham, D. B. and Pop, I. 2008; Harris, S. D., Ingham, D. B. and Pop, I. 2002) stated that for small-time solution, where $\tau << 1$, all impulsive changes in the temperature or heat flux, there is a short period in which the effects are confined to a thin boundary layer adjacent to the surface. So, for a small time solution, the diffusion scale can be set to $\tau^{\frac{1}{2}}$ with the following variables:

- Momentum:

$$f = 2\tau^{\frac{1}{2}} F(\zeta, \tau) \tag{5.16}$$

$$\zeta = \frac{\eta}{2\tau^{\frac{1}{2}}} \tag{5.17}$$

- Energy constant wall temperature:

$$g = G(\zeta, \tau) \tag{5.18}$$

- Energy constant wall heat flux:

$$g = 2\tau^{\frac{1}{2}} G(\zeta, \tau) \tag{5.19}$$

Applying equations 5.16, 5.17, 5.18 and 5.19 to equations 5.4, 5.5 and 5.6 the following equations are obtained:

- Momentum:

$$\frac{\partial^3 F}{\partial \zeta^3} + \left[2\zeta + 4m\tau F + 4(m-1)\tau^2 \frac{\partial F}{\partial \tau}\right] \frac{\partial^2 F}{\partial \zeta^2} + 4m\tau \left[1 - \left(\frac{\partial F}{\partial \zeta}\right)^2\right] = 4\tau \left[1 + (m-1)\tau \frac{\partial F}{\partial \zeta}\right] \frac{\partial^2 F}{\partial \zeta \partial \tau} \tag{5.20}$$

- Energy constant wall temperature:

$$\frac{1}{Pr} \frac{\partial^2 G}{\partial \zeta^2} + \left[2\zeta + 4m\tau F + 4(m-1)\tau^2 \frac{\partial F}{\partial \tau}\right] \frac{\partial G}{\partial \zeta} = 4\tau \left[1 + (m-1)\tau \frac{\partial F}{\partial \zeta}\right] \frac{\partial G}{\partial \tau} \tag{5.21}$$

- Energy constant heat flux:

$$\frac{1}{Pr}\frac{\partial^2 G}{\partial \zeta^2} + \left[2\zeta + 4m\tau F + 4(m-1)\tau^2 \frac{\partial F}{\partial \tau}\right]\frac{\partial G}{\partial \zeta} - 2G = 4\tau\left[1 + (m-1)\tau\frac{\partial F}{\partial \zeta}\right]\frac{\partial G}{\partial \tau} \quad (5.22)$$

Boundary Conditions:

- Momentum:

$$F(0,\tau) = 0 \quad (5.23)$$

$$\frac{\partial F}{\partial \zeta}(0,\tau) = 0 \quad (5.24)$$

$$\frac{\partial F}{\partial \zeta}(\infty,\tau) \to 1 \quad (5.25)$$

- Energy constant wall temperature:

$$G(0,\tau) = 1 \quad (5.26)$$

$$G(\infty,\tau) \to 0 \quad (5.27)$$

- Energy constant wall heat flux:

$$\frac{\partial G}{\partial \zeta}(0,\tau) = -1 \quad (5.28)$$

$$G(\infty,\tau) \to 0 \quad (5.29)$$

It is known that for small time, the solution of equations 5.20, 5.21 and 5.22 have the following form:

- Momentum:

$$F(\zeta,\tau) = F_0(\zeta) + F_1(\zeta)\tau + ... \quad (5.30)$$

• Energy constant wall temperature and heat flux:

$$G(\zeta,\tau) = G_0(\zeta) + G_1(\zeta)\tau + ... \tag{5.31}$$

Applying equations 5.30 and 5.31 to equations 5.20, 5.21 and 5.22 yields the following set of equations for momentum and energy:

• Momentum:

$$F_0^{'''} + 2\zeta F_0^{''} = 0 \tag{5.32}$$

$$F_1^{'''} + 2\zeta F_1^{''} - 4F_1^{'} = -4m(1 - F_0^{'2} + F_0 F_0^{''}) \tag{5.33}$$

• Energy constant wall temperature:

$$\frac{1}{Pr}G_0^{''} + 2\zeta G_0^{'} = 0 \tag{5.34}$$

$$\frac{1}{Pr}G_1^{''} + 2\zeta G_1^{'} - 4G_1 = -4mF_0 G_0^{'} \tag{5.35}$$

• Energy constant wall heat flux:

$$\frac{1}{Pr}G_0^{''} + 2\zeta G_0^{'} - 2G_0 = 0 \tag{5.36}$$

$$\frac{1}{Pr}G_1^{''} + 2\zeta G_1^{'} - 6G_1 = -4mF_0 G_0^{'} \tag{5.37}$$

Boundary Conditions:

• Momentum:

$$F_0(0) = F_0^{'}(0) = 0 \tag{5.38}$$

$$F_0^{'}(\infty) \to 1 \tag{5.39}$$

$$F_1(0) = F_1^{'}(0) = 0 \tag{5.40}$$

$$F_1^{'}(\infty) \to 0 \tag{5.41}$$

- Energy constant wall temperature:

$$G_0(0) = 1 \tag{5.42}$$

$$G_0(\infty) \to 0 \tag{5.43}$$

$$G_1(0) = 0 \tag{5.44}$$

$$G_1(\infty) \to 0 \tag{5.45}$$

- Energy constant wall heat flux:

$$G_0^{'}(0) = -1 \tag{5.46}$$

$$G_0(\infty) \to 0 \tag{5.47}$$

$$G_1^{'}(0) = 0 \tag{5.48}$$

$$G_1(\infty) \to 0 \tag{5.49}$$

Equations 5.32, 5.33, 5.34, 5.35, 5.36, and 5.37 are solved by applying a finite difference algorithm with boundary conditions 5.38, 5.39, 5.40 5.41, 5.42, 5.43, 5.44, 5.45, 5.46, 5.47, 5.48 and 5.49.

In addition, the skin friction can be obtain as:

$$C_f\sqrt{Re_x} = \frac{\partial^2 f}{\partial \eta^2}(0,\tau) \tag{5.50}$$

Skin friction can be obtained analytically as:

$$C_f\sqrt{Re_x} = \frac{1}{\sqrt{\pi}}\tau^{-\frac{1}{2}} + \frac{m}{\sqrt{\pi}}\left(1+\frac{4}{3\pi}\right)\sqrt{\tau} \tag{5.51}$$

The Nusselt number for the constant wall temperature case can be obtained as:

$$\frac{Nu}{Re_x^{\frac{1}{2}}} = -\frac{\partial g}{\partial \eta}(0,\tau) \tag{5.52}$$

The Nusselt number for the constant wall temperature case can be obtained analytically as:

$$\frac{Nu}{Re_x^{\frac{1}{2}}} = \sqrt{\frac{Pr}{\pi}}\tau^{-\frac{1}{2}} + \frac{m}{\pi}\sqrt{\frac{Pr}{\pi}}\left[(1+Pr)^2 tan^{-1}\left(\frac{1}{\sqrt{Pr}}\right) - \frac{1}{3}\sqrt{Pr}(5+3Pr)\right]\tau^{\frac{1}{2}} \tag{5.53}$$

The wall temperature for the constant wall heat flux case for a Pr of one can be obtained as:

$$g_w(\tau) = g(0,\tau) \tag{5.54}$$

The wall temperature for the constant wall heat flux case for a Pr of one can be obtained analytically as:

$$g_w(\tau) = \frac{2}{\sqrt{\pi}}\tau^{\frac{1}{2}} + \frac{4}{3}\frac{m}{\sqrt{\pi}}\left(1-\frac{10}{3\pi}\right)\tau^{\frac{3}{2}} \tag{5.55}$$

5.4 Unsteady Boundary Layer Similarity Equations Finite Difference Solution

As stated in the previous section, equations 5.32, 5.33, 5.34, 5.35, 5.36 and 5.37 are solved via a finite difference algorithm.

These equations can be discretized by finite difference as follows:

• Momentum (equations 5.32 and 5.33):

$$F'_{0(i)} = \frac{(1+\zeta_{(i)}\Delta\zeta)F'_{0(i+1)} + (1-\zeta_{(i)}\Delta\zeta)F'_{0(i-1)}}{2} \tag{5.56}$$

$$F'_{1(i)} = \frac{(1+\zeta_{(i)}\Delta\zeta)F'_{1(i+1)} + (1-\zeta_{(i)}\Delta\zeta)F'_{1(i-1)} + \Delta\zeta^2 * C_M}{2(1+2\Delta\zeta^2)} \tag{5.57}$$

Where:

$$C_M = 4m(1 - F'_{0(i)}F'_{0(i)} + F_{0(i)}F''_{0(i)}) \tag{5.58}$$

The F_0 term can be obtained by applying a modified Forward Euler as:

$$F_{0(i+1)} = F_{0(i)} + \Delta\zeta\frac{F'_{0(i)} + F'_{0(i+1)}}{2} \tag{5.59}$$

The term F''_0 can be found by applying a similar solution found in equations 2.28, 2.29, and 2.30.

Energy constant wall temperature condition equations 5.34 and 5.35:

$$G_{0(i)} = \frac{(1+Pr\zeta_{(i)}\Delta\zeta)G_{0_(i+1)} + (1-Pr\zeta_{(i)}\Delta\zeta)G_{0(i-1)}}{2} \tag{5.60}$$

$$G_{1(i)} = \frac{(1+Pr\zeta_{(i)}\Delta\zeta)G_{1(i+1)} + (1-Pr\zeta_{(i)}\Delta\zeta)G_{1(i-1)} + C_E}{2(1+2Pr\Delta\zeta^2)} \tag{5.61}$$

Where:

$$C_E = 4mPr\Delta\zeta^2 F_{0(i)}G'_{0(i)} \tag{5.62}$$

• Energy constant wall heat flux condition (equations 5.36 and 5.37):

$$G_{0(i)} = \frac{(1 + Pr\zeta_{(i)}\Delta\zeta)G_{0(i+1)} + (1 - Pr\zeta_{(i)}\Delta\zeta)G_{0(i-1)}}{2(1 + Pr\Delta\zeta^2)} \tag{5.63}$$

$$G_{1(i)} = \frac{(1 + Pr\zeta_{(i)}\Delta\zeta)G_{1(i+1)} + (1 - Pr\zeta_{(i)}\Delta\zeta)G_{1(i-1)} + C_E}{2(1 + 3Pr\Delta\zeta^2)} \tag{5.64}$$

Where:

$$C_E = 4mPr\Delta\zeta^2 F_{0(i)} G'_{0(i)} \tag{5.65}$$

The G'_0 term can be found by applying a similar solution found in equations 2.35, 2.36 and 2.37.

Equations 5.56, 5.57, 5.59, 5.60, 5.61, 5.63 and 5.64 are solve by using an explicit finite difference algorithm with boundary conditions 5.38, 5.39, 5.40, 5.41, 5.42, 5.43, 5.44, 5.45, 5.46, 5.47, 5.48 and 5.49.

5.5 Results and Discussion

An explicit finite difference method was employed to perform the transient numerical analysis. The computational performance of the sequential MATLAB code was assessed by discretizing the problem domain into 1000 nodes. The execution time of the code on an MSI laptop (8 CPU-cores and 16 GB of RAM memory) for a transient stability investigation, based on the displacement thickness coordinate under a zero pressure gradient condition at various time instances τ, is depicted in Figure 5.1. The average execution time for this analysis was approximately 8 hours. Furthermore, the stability analysis procedure presents potential avenues for optimization, which could be achieved by enhancing the MATLAB left division operation or by implementing a transformation to the eigenvalue matrix to accelerate the solution process. These solvers are inherently amenable to computational optimizations. Future work could involve optimizing the code for more efficient execution by leveraging parallel computing frameworks such as OpenMP or Open Multiprocessing. OpenMP, for instance, utilizes multiple processor threads (the smallest unit of execution) to parallelize computations, thereby significantly improving performance, especially for large-scale simulations with node counts exceeding 1000.

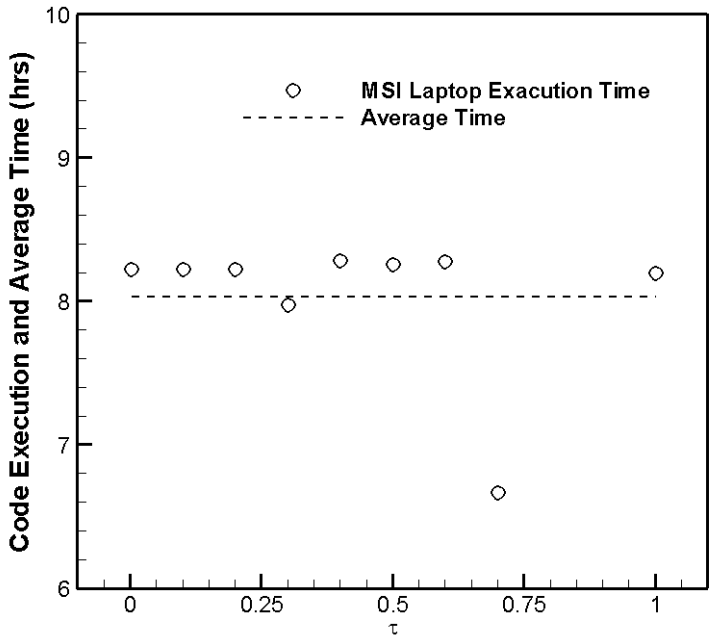

Figure 5.1: Matlab code execution time for a zero pressure gradient case at different time τ

Figure 5.2 presents the results of a grid convergence study, wherein the computed skin friction coefficient, as defined in equation 5.50, is evaluated for discretizations comprising 100, 1000, and 3200 nodes. These numerical results are compared against the analytical expression for the skin friction coefficient provided in equation 5.51, under a pressure gradient condition of 0.5. The data clearly indicate that increasing the nodal resolution yields progressively closer agreement with the analytical solution across a range of non-dimensional time values τ. Notably, the simulation employing 3200 nodes demonstrates the highest fidelity with respect to the analytical benchmark, thereby justifying its selection as the minimum resolution required to ensure numerical accuracy in subsequent computations. Furthermore, the figure illustrates a monotonic decay in the skin friction coefficient with increasing τ, consistent with theoretical expectations. For a comprehensive discussion of the underlying physical and numerical framework, the reader is directed to (Ramirez, M. A. and Araya, G. 2023; Ramirez, M. A. and Araya, G. 2025).

Figure 5.3 shows the variations of the non-dimensional stream function for different values of τ ranging from 0.01 to 1.0 at a pressure gradient of zero. It can be seen in the figure that as time progresses, the slope of the curve decreases (the values of the stream function

at high τ decrease) until it reaches the steady-state condition.

Figure 5.4 shows the variations of the non-dimensional velocity function for different values of τ ranging from 0.01 to 1.0 at a pressure gradient of zero. It can be seen in the

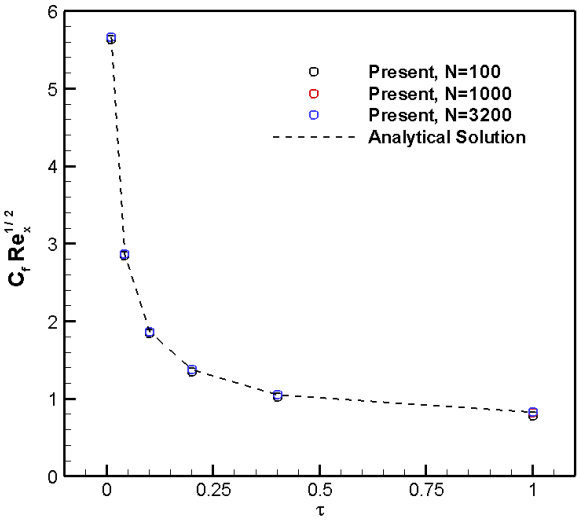

Figure 5.2: Present and Analytical Skin Friction Coefficient grid test at different τ for a pressure gradient of 0.5.

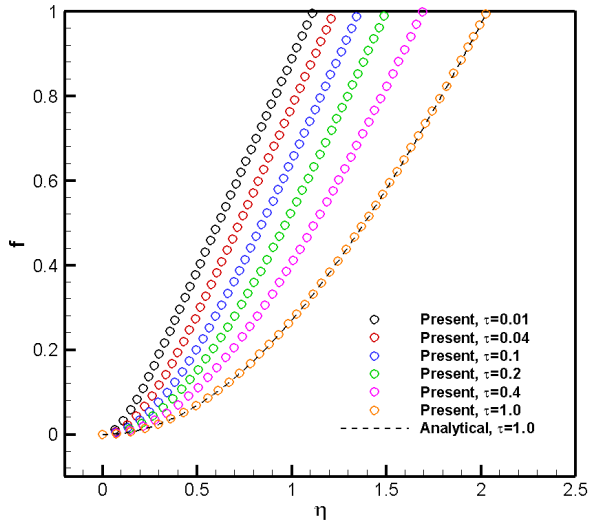

Figure 5.3: Non-dimensional free stream function distribution at various dimensionless time numbers τ for the Blasius solution.

figure that as τ decreases, the curves reach a potential flow solution faster. This means that as time increases, the boundary layer thickness increases until the flow reaches its steady-state solution.

Figure 5.5 shows the dimensionless shear stress function variations for different τ values ranging from 0.01 to 1.0 at a pressure gradient of zero. The figure shows that as the τ term increases, the wall shear stress decreases. It is important to mention that when the dimensionless shear stress reaches a value of zero, a flow separation occurs, and the boundary layer equations can no longer be applied.

Figures 5.6, 5.7 and 5.8 show the dimensionless variations in the flow, velocity, and shear stress function for a pressure gradient of -0.18, 0, 0.3333, and 0.5 at τ of 1. In Figure 5.6 it can be seen that as the pressure gradient decreases, the values of the stream curves decrease. In addition, it can be observed in Figures 5.7 and 5.8 that as the pressure gradient decreases, the thickness of the boundary layer thickness increases and the shear stress at the wall decreases. This means that increasing the pressure gradient decreases the time it takes the flow to reach its steady-state condition.

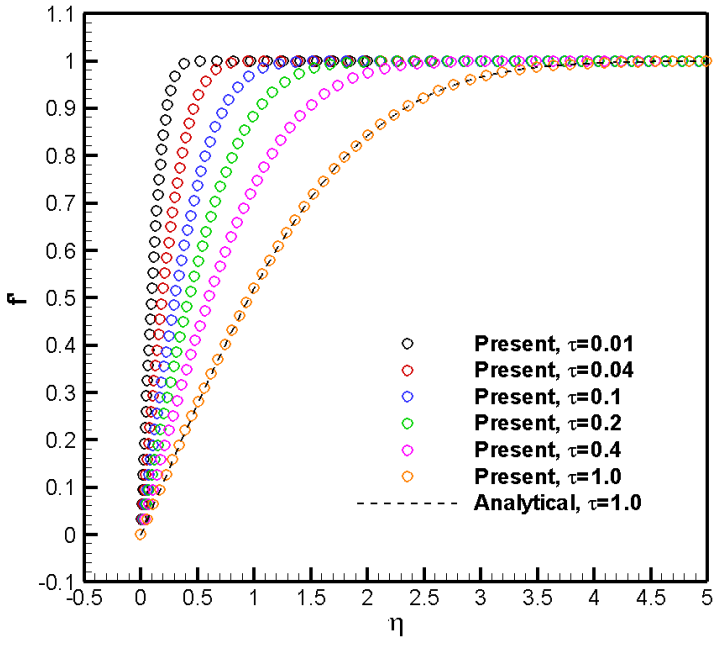

Figure 5.4: Non-dimensional velocity function distribution at various dimensionless time numbers τ for the Blasius solution.

Figure 5.9 illustrates a grid sensitivity analysis in which the numerically computed Nusselt number is compared across spatial discretizations consisting of 100, 1000, and 3200 nodes. These results are benchmarked against the corresponding analytical solution for the Nusselt number under a constant wall temperature condition and a pressure gradient

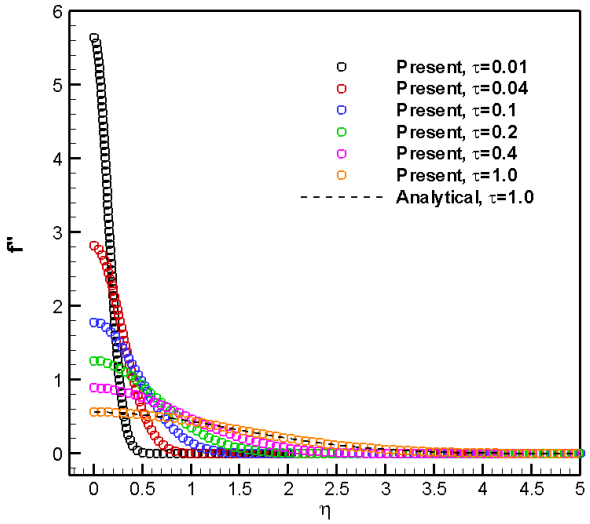

Figure 5.5: Dimensionless shear stress function distribution at various dimensionless time numbers τ for a pressure gradient of zero.

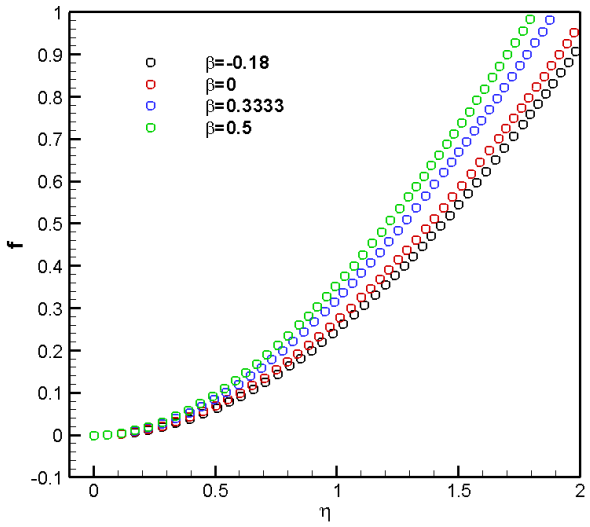

Figure 5.6: Non-dimensional stream function distribution at a pressure gradient of -0.18, 0, 0.3333 and 0.5 for a τ of 1.

of 0.5. As the spatial resolution increases, the numerical predictions demonstrate improved convergence toward the analytical solution over a range of non-dimensional times τ. The highest resolution case, comprising 3200 nodes, yields the closest agreement,

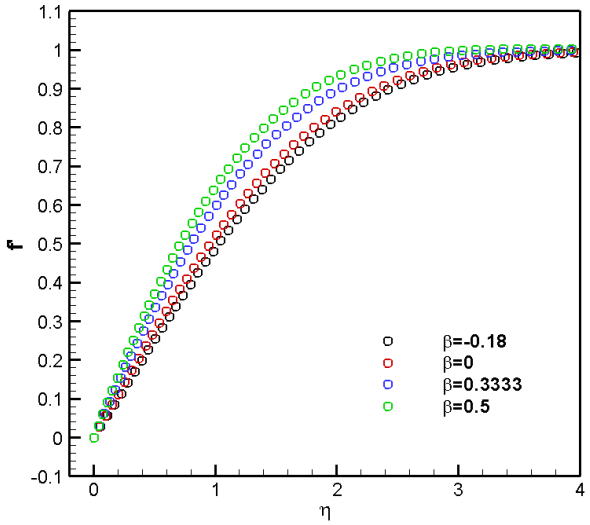

Figure 5.7: Non-dimensional velocity function distribution at a pressure gradient of -0.18, 0, 0.3333 and 0.5 for a τ of 1.

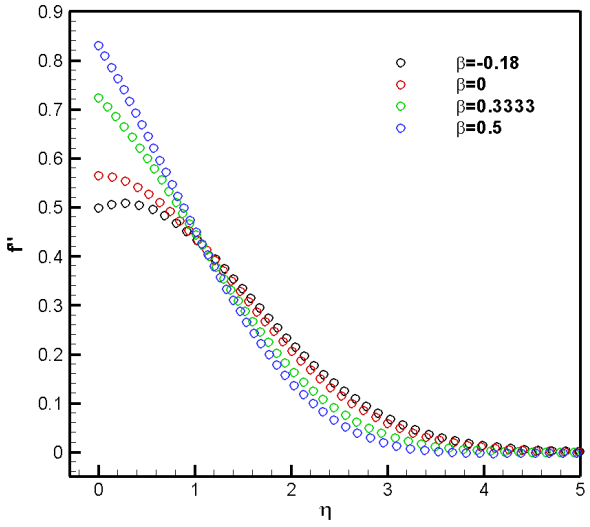

Figure 5.8: Non-dimensional shear stress function distribution at a pressure gradient of -0.18, 0, 0.3333, and 0.5 for a τ of 1.

substantiating its selection as the optimal mesh density to ensure numerical fidelity. Additionally, the figure reveals a decreasing trend in the Nusselt number with increasing τ, which is consistent with the expected thermal boundary layer development under the specified flow conditions.

Figure 5.10 shows the Nusselt number vs. τ variation for different Prandtl numbers of 0.1, 0.2, 0.71, 2, 5, and 10 for a pressure gradient of 0.5 under a constant wall temperature condition. As stated before, the figure shows that as the τ term increases, the Nusselt number decreases. Also, it is observed that as the Prandtl number increases, the Nusselt number increases. Figure 5.11 shows the variations of the dimensionless temperature function for different values of τ ranging from 0.01 to 1.0 at a pressure gradient of zero under a constant temperature condition. It can be seen in the figure that as time progresses, the values of the temperature function increase until it reaches its steady-state condition. The thermal boundary layer is also observed to increase as τ increases.

Figure 5.12 shows the variations of the dimensionless heat flux function for different τ values ranging from 0.01 to 1.0 at a pressure gradient of zero under a constant wall temperature condition. It can be seen in the figure that as the τ term increases, the heat flux at the wall decreases due to the fact that the temperature starts to reach its steady-state condition. Also, it can be said that if the heat flux at the wall is zero, an adiabatic wall condition is reached.

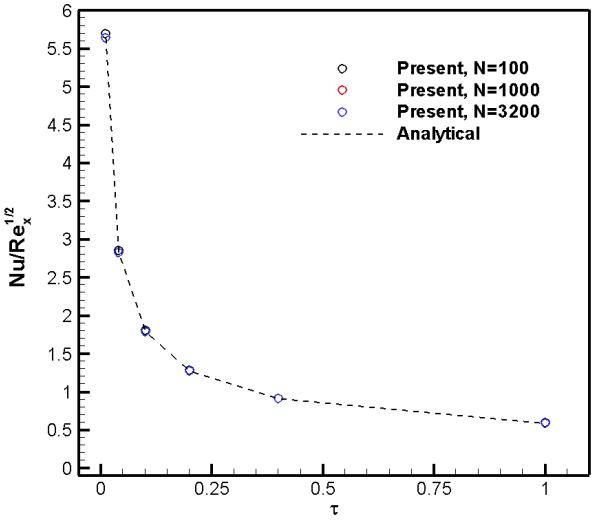

Figure 5.9: Present and Analytical Nusselt number grid test at different τ for a pressure gradient of 0.5 for a constant wall temperature.

Figure 5.13 illustrates the variations of the non-dimensional temperature function for different Prandtl numbers, ranging from 0.01 to 10, under a zero pressure gradient condition with a constant wall temperature at a τ value of 1. As shown in the figure, the temperature decreases with increasing η, eventually reaching zero as it approaches the

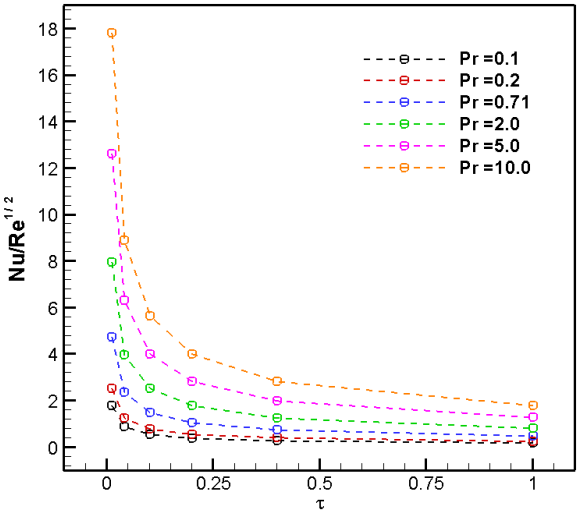

Figure 5.10: Nusselt number vs τ for Prandtl numbers of 0.1, 0.2, 0.71, 2, 5, and 10 for a pressure gradient of 0.5 at a constant wall temperature condition.

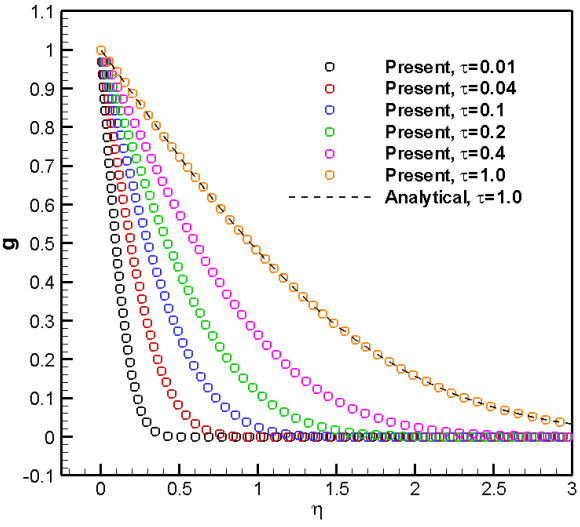

Figure 5.11: Dimensionless temperature function distribution at various dimensionless time numbers τ for the Blasius Solution at a constant wall temperature.

free stream. Regarding the Prandtl numbers, it is evident that as the Prandtl number increases, the thermal boundary layer thickness reduces.

Figure 5.14 shows the variations of the non-dimensional heat flux function for different

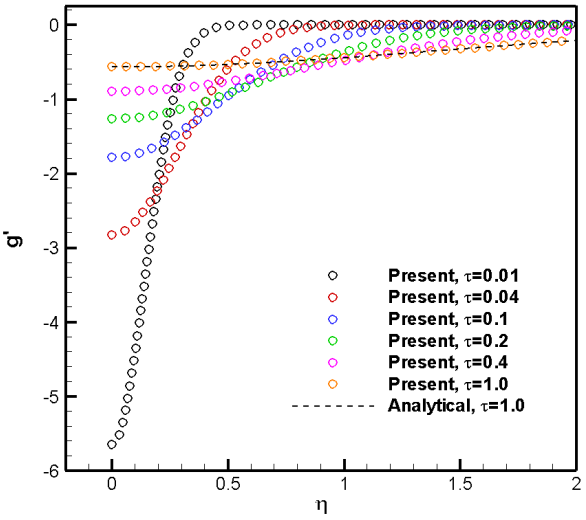

Figure 5.12: Non-dimensional heat flux function distribution at various dimensionless time numbers τ for a pressure gradient of zero for a constant wall temperature.

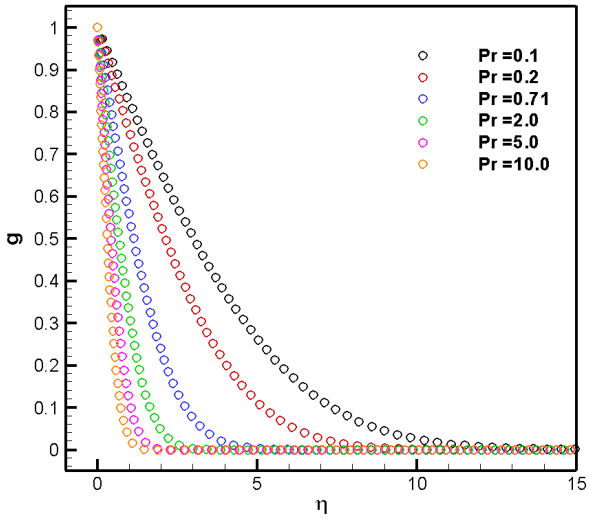

Figure 5.13: Dimensionless temperature function distribution at various Prandtl numbers for the Blasius Solution at a constant wall temperature for a τ of 1.

Prandtl number values ranging from 0.01 to 10 at a pressure gradient of zero under a constant wall temperature condition with a τ of 1. It can be seen in the figure that the heat flux starts with a value at the wall and then decreases to zero when it reaches the free stream. The figure shows that as the Prandtl number increases, the heat flux at the wall increases in the negative direction.

Figures 5.15 and 5.16 show the dimensionless temperature and heat flux function variations for pressure gradients of -0.18, 0, 0.3333 and 0.5 at τ of 1 for a constant wall temperature condition. In Figure 5.15 it can be seen that as the pressure gradient decreases, the thermal boundary layer at $\tau = 1$ increases. In addition, it can be observed in Figure 5.16 that as the pressure gradient decreases, the heat flux at the wall decreases. As stated before, this means that as the pressure gradient increases, the time it takes for the flow to reach its steady state condition decreases.

Figure 5.17 shows the non-dimensional wall temperatures at τ ranging from 0.01 to 1.0 for a pressure gradient of 0.5 at a constant wall heat flux. It can be seen that as the τ increases, the temperature in the wall increases.

Figure 5.18 shows the values of the variations of the non-dimensional wall temperature function versus τ at different Prandtl numbers ranging from 0.01 to 10 at a pressure gradient of 0.5 for a constant wall heat flux condition. As stated before, it can be seen that as time progresses, the values of the wall temperature increase until it reaches the

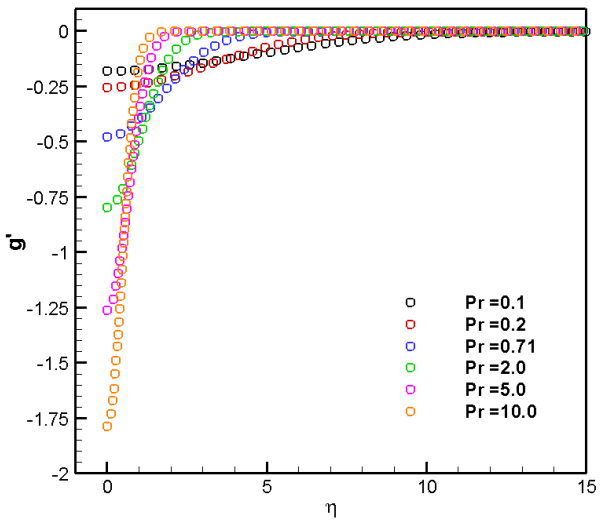

Figure 5.14: Non-dimensional heat flux function distribution at various Prandtl numbers for a pressure gradient of zero at a constant wall temperature with a τ of 1.

steady-state condition. In the case of the Prandtl numbers, it is observed that as the Prandtl number increases, the temperature at the wall decreases.

Figure 5.19 shows the variations of the non-dimensional temperature function for different

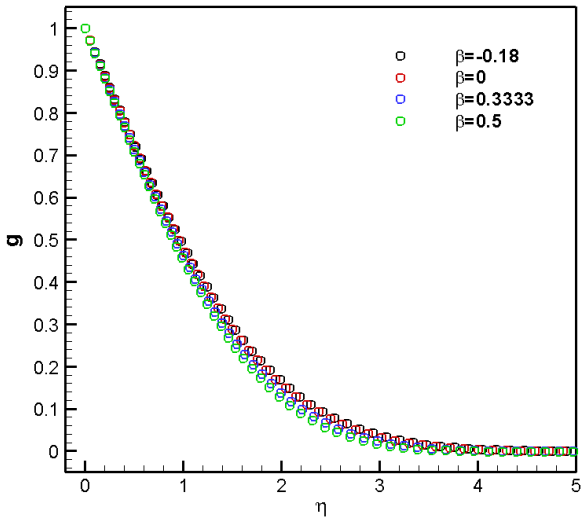

Figure 5.15: Dimensionless temperature distribution at pressure gradient of -0.18, 0, 0.3333 and 0.5 for a τ of 1 for a constant wall temperature.

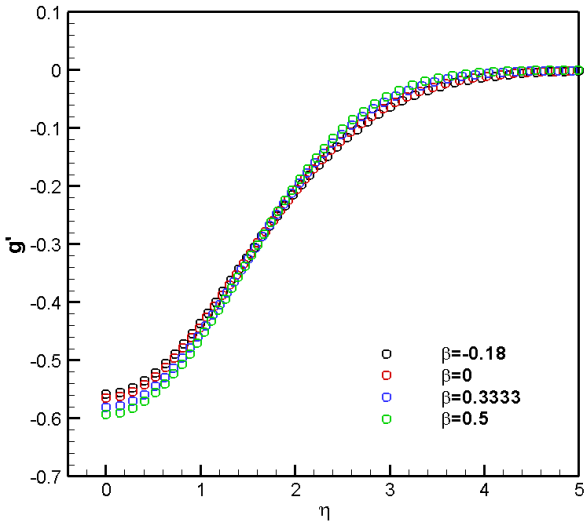

Figure 5.16: Dimensionless heat flux function distribution at pressure gradient of -0.18, 0, 0.3333 and 0.5 for a τ of 1 for a constant wall temperature.

values of τ ranging from 0.01 to 1.0 at a pressure gradient of zero under a constant wall

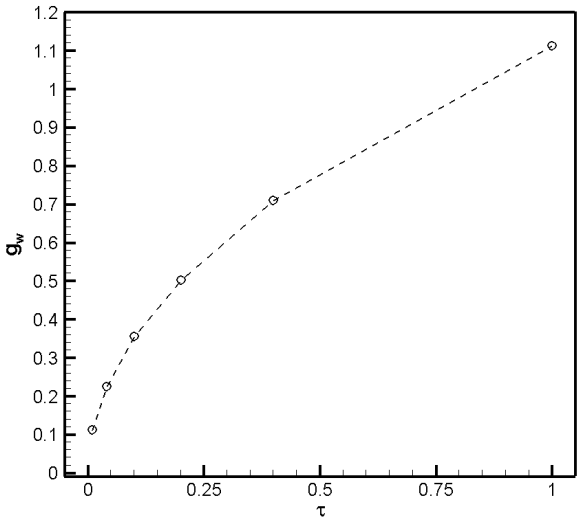

Figure 5.17: Non-dimensional wall temperatures at different τ for a pressure gradient of 0.5 for a constant wall heat flux.

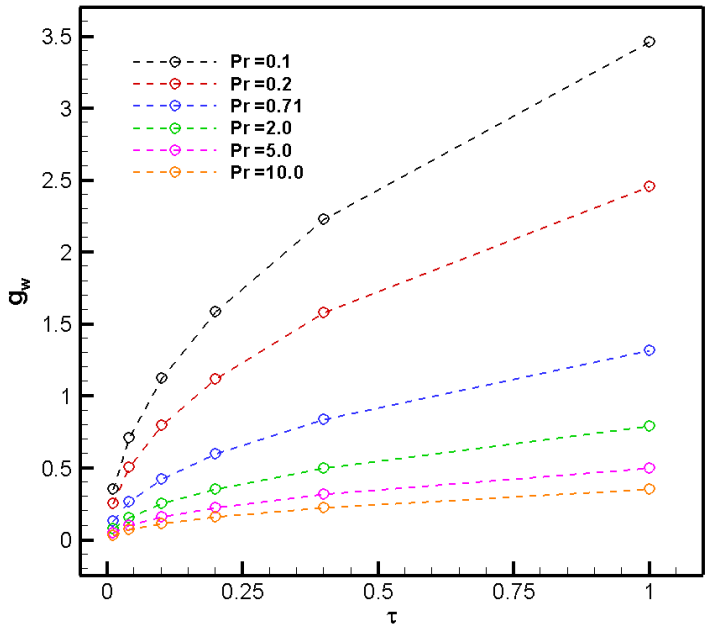

Figure 5.18: Non-dimensional temperature function distribution at various Prandtl numbers for pressure gradient of 0.5 at a constant wall heat flux.

heat flux condition. It can be seen in the figure that as time progresses, the values of the wall temperature increase until it reaches the steady-state condition. It is also observed that the thermal boundary layer increases as the τ increases.

Figure 5.20 shows the variations of the dimensionless heat flux function for different τ values ranging from 0.01 to 1.0 at a pressure gradient of zero under a constant wall heat flux condition. It can be seen in the figure that as the τ term increases, the heat flux increases. Also, the figure shows that the heat flux starts with a value of minus one (heat loss) at the wall and increases until it reaches the freestream condition where there is no more heat transfer. Finally, it can be said that as the dimensionless time decreases, the curves reach the freestream condition faster.

Figure 5.21 shows the dimensionless temperature function variations for different Prandtl numbers ranging from 0.01 to 10 at a pressure gradient of zero at a constant wall heat flux condition for a τ of 1. The figure shows that as the Prandtl number increases, the temperature at the wall decreases and the thermal boundary layer thickness decreases.

Figure 5.22 shows the variations of the non-dimensional heat flux function for different Prandtl numbers ranging from 0.01 to 10 at a pressure gradient of zero at a constant wall heat flux condition for a τ of 1. The figure shows that as the Prandtl number increases, the heat flux reaches a freestream condition faster. Also, as seen before, the heat flux starts at a value of negative one (heat loss) at the wall and increases until it reaches the

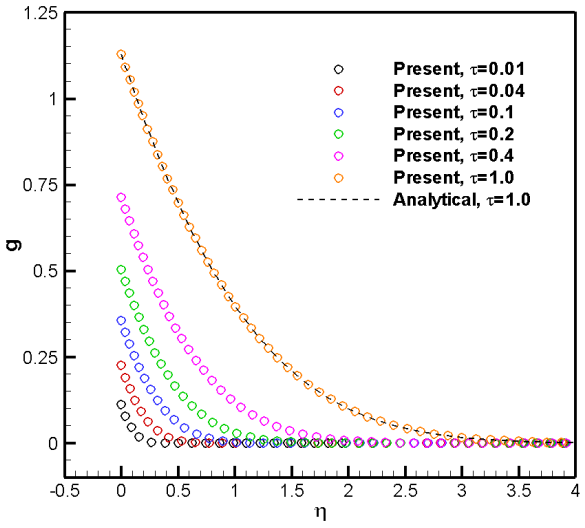

Figure 5.19: Non-dimensional temperature function distribution at various dimensionless time numbers τ for the Blasius solution for a constant wall heat flux.

free stream condition, where there is no more heat transfer.

Figures 5.23 and 5.24 show the dimensionless temperature and heat flux function variations for pressure gradients of -0.18, 0, 0.3333,a and 0.5 at τ of 1 for a constant wall heat flux. It can be observed in Figure 5.23 that as the pressure gradient decreases, the

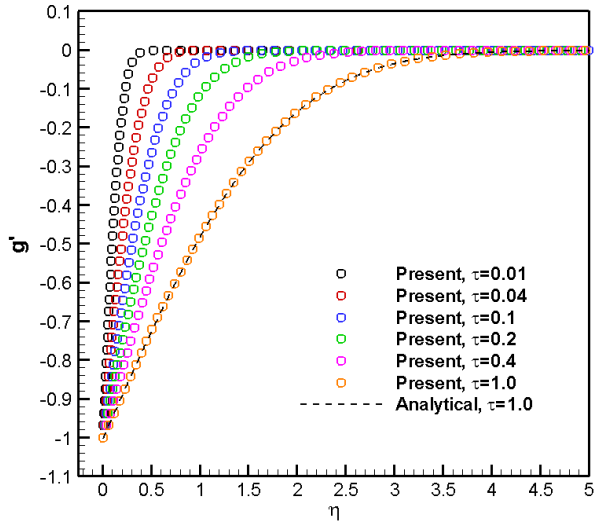

Figure 5.20: Dimensionless heat flux function distribution at various dimensionless time numbers τ for a pressure gradient of zero for a constant wall heat flux.

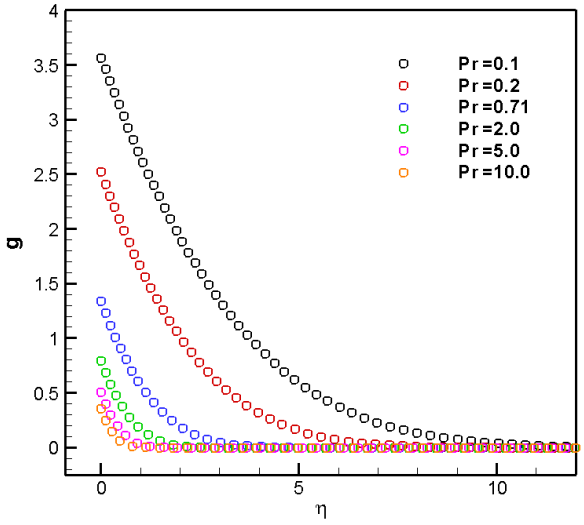

Figure 5.21: Dimensionless temperature function distribution at different Prandlt numbers for the Blasius solution at a constant wall heat flux with a τ of 1.

thermal boundary layer at $\tau = 1$ increases. In addition, it can be observed in Figure 5.24 that as the pressure gradient decreases, the heat flux decreases.

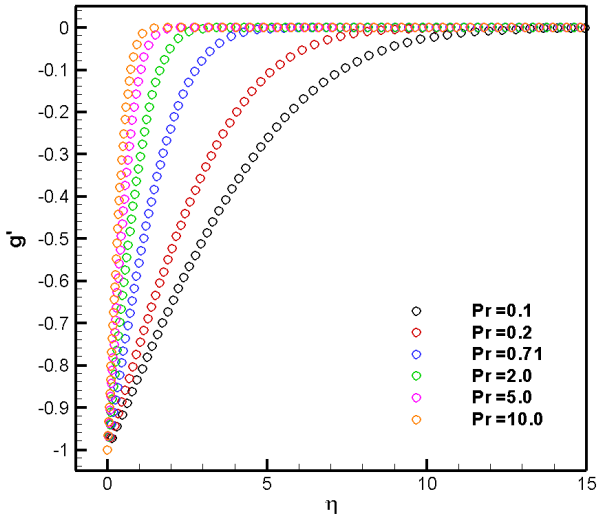

Figure 5.22: Dimensionless heat flux function distribution at different Prandlt numbers for the Blasius Solution at a constant wall heat flux with a τ of 1.

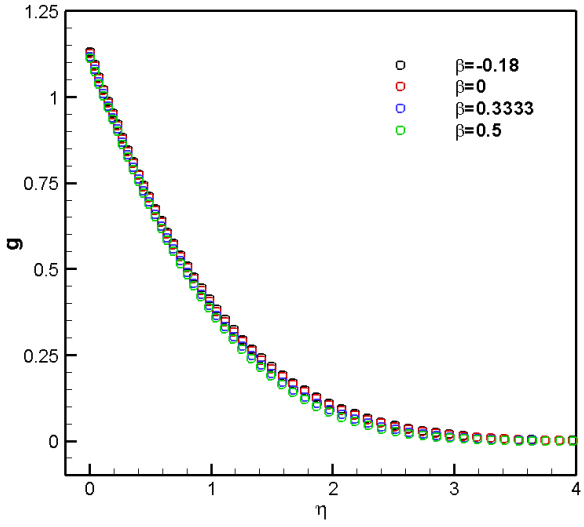

Figure 5.23: Dimensionless temperature distribution at pressure gradient of -0.18, 0, 0.3333 and 0.5 for a τ of 1 for a constant wall heat flux.

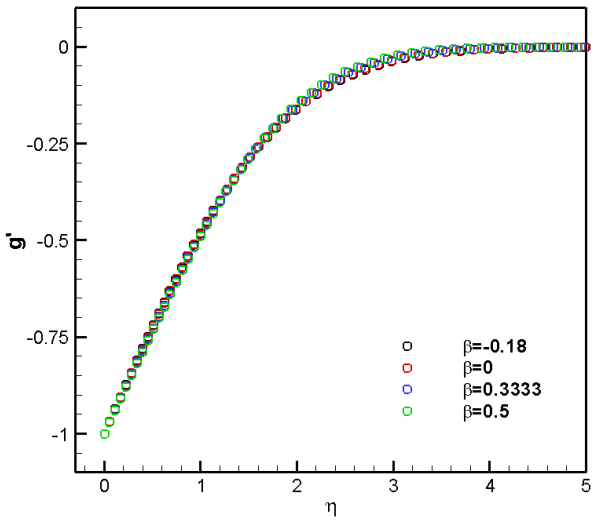

Figure 5.24: Heat Flux Function distribution at a pressure gradient of -0.18, 0, 0.3333 and 0.5 for a τ of 1 for a constant wall temperature.

5.6 Chapter 5 Conclusions

The skin friction coefficient and Nusselt numbers present and analytical values were compared at different node numbers and it was found that the simulation could be run with a number of 3200. Also, the effects of τ in the dimensionless stream, velocity, and shear function were studied. It was found that as time progresses the stream function slope decreases, the boundary layer thickness increases, and the shear stress of the wall decreases. This means that as the flow τ increases, the flow will eventually reach its steady state condition. In the case of the energy equation, for a constant wall temperature condition, the thermal boundary layer increases as the τ increases. In the case of heat flux for the same condition, the heat flux at the wall decreased as τ progressed. In the case of the Prandtl number, as the Prandtl number increases, the thermal boundary layer decreases. Also, for the same condition, it is observed that as the pressure gradient increases, the thermal boundary layer decreases, and the heat flux at the wall increases in the negative direction. Next, for a constant wall heat flux condition, the thermal boundary layer thickness and the wall temperature increase as the τ increases. In the case of heat flux for the same condition, the slope of the curves decreased as τ increased. In the case of the Prandtl number, as the Prandtl number increases, the wall temperature decreases, and the thermal boundary layer decreases. Also, as the pressure gradient increases, there is a very small decrease in the thermal boundary layer, and a small increase in the heat flux is observed. In the end, when the effects of the energy for different pressure gradients of τ are compared to the effects of the momentum equation, it can be observed that the pressure gradient has a more significant effect in the momentum equations than in the energy equations. The most relevant results of this chapter are published in (Ramirez, M. A. and Araya, G. 2023; Ramirez, M. A. and Araya, G. 2025).

Chapter 6
Compressible Boundary Layers Subject to Streamwise Pressure Gradient

6.1 Compressible Boundary Layers Introduction

The compressible external flows are analyzed using the Prandtl boundary layer theory. It is crucial to note that the same Prandtl assumptions established in Section 1.1.2 for incompressible flow must also apply to compressible flows. The boundary layer equations divide the flow into two distinct regions: the near-wall region and the outer flow region. Falkner and Skan (Falkner, V. M. and Skan, S. W. 1930) extended the boundary layer theory by introducing the concept of the streamwise pressure gradient, providing a more general solution for flows over wedges and under constant pressure gradients. These solutions can be categorized as follows: Favorable Pressure Gradient (flow acceleration), Zero Pressure Gradient (Blasius solution), and Adverse Pressure Gradient (flow deceleration). It is important to emphasize that adverse pressure gradients are undesirable, as they can lead to flow separation. As the fluid flow speed increases beyond Mach 0.3 or 5 (hypersonic flows), issues associated with compressibility emerge. In this high-speed flow, thermodynamic variations of density, viscosity, thermal conductivity, pressure, and temperature must be taken into account in the Falkner-Skan solutions. This is done by coupling the momentum (describes flow dynamics) and energy (associated with temperature) equations and adding an equation of state to describe the flow properties. The boundary layer equations for compressible flow are solved via a similarity solution. Similarity reduces the partial differential equations to an ordinary differential equation with a smaller number of independent variables. In addition, for incompressible flow similarity is achieved by grouping the parallel and perpendicular coordinates of the wall into a single similarity variable η. In the case of compressible flow, Illingworth found that

the parallel and perpendicular wall coordinates could be grouped in terms of two similarity variables: ξ, which takes into account the viscosity effects, and η, which takes into account the effects of density. This similarity solution is usually solved by a point and shoot algorithm where the shear stress at the wall is guessed, so that the velocity at the free stream has a value of one. When applying this method, the equations are solved with a Runge-Kutta fourth-order algorithm with an order reduction.

In this work, an explicit finite difference scheme will be employed to solve the similarity differential equation, thereby avoiding the point-and-shoot method. The finite difference method (FDM) is readily applicable for approximating the terms $f^{'}$ and g, while a modified forward Euler method is used to compute the term f.

6.2 Blasius Laminar Compressible Flow Solution

As stated in chapter 2, the Blasius compressible flow momentum and energy equations are given by:

$$Cf^{'''} + f^{''}(C^{'} + f) = 0 \tag{6.1}$$

$$Cg^{''} + g^{'}(C^{'} + Prf) = -BCf^{''}f^{''} \tag{6.2}$$

Where:

$$C^{'} = (n-1)g^{n-2}g^{'} \tag{6.3}$$

C and B are given by equations 2.50 and 2.51.

In this case, g is given as:

$$g = \frac{T}{T_e} \tag{6.4}$$

Where T is the local fluid flow temperature and T_e is the temperature at the boundary layer edge.

This type of problem is solved as a boundary condition value problem.

For the case of C equal to one and the case with variable C at Mach number of zero:

• The boundary conditions near the wall are:

$$f(0) = f^{'}(0) = 0 \tag{6.5}$$

$$g\ (0) = 1\ for\ Adiabatic\ wall \tag{6.6}$$

$$g'\ (0) = 0\ for\ Adiabatic\ wall \tag{6.7}$$

• The boundary conditions far from the wall:

$$f'\ (\infty) = 1 \tag{6.8}$$

$$g(\infty) = 1 \tag{6.9}$$

In the case for the hot and the cold wall for a C equal to one and for a variable C at a Mach number of zero:

• The f and $f^{'}$ boundary conditions at the wall stay the same.

• The g boundary conditions at the wall:

$$g(0) = g_w \tag{6.10}$$

• The $f^{'}$ and g boundary conditions at far from the wall remain the same.

Note: In this case if g_w is more than one, the flow is considered a hot wall flow, and if it is less than one is considered a cold wall flow.

For a C equal to one and a variable C at a Mach number not equal to zero:

• The f and $f^{'}$ boundary conditions at the wall stay the same.

• The $f^{'}$ and g boundary conditions at far from the wall remain the same.

• The adiabatic condition at the wall is found by changing g_w until $g_w^{'}$ is zero for the

corresponding Mach number and pressure gradient. In the case of a hot and cold wall conditions if g_w is higher than this adiabatic g_w the flow has a hot wall condition and if g_w is lower than this adiabatic g_w the flow has a cold wall condition.

Equation 6.1 in term of the $f^{'}$ is written as:

$$C\frac{\partial^2 f^{'}}{\partial \eta^2} + \frac{\partial f^{'}}{\partial \eta}(C^{'} + f) = 0 \tag{6.11}$$

Equation 6.2 in term of the g is written as:

$$C\frac{\partial^2 g}{\partial \eta^2} + \frac{\partial g}{\partial \eta}(C^{'} + Prf) = -BCf^{''}f^{''} \tag{6.12}$$

The f term is solved by applying a Modified Forward Euler to equation 2.20 yielding equation 2.21.

Applying Central difference to equation 6.11 yields the following:

Explicit:

$$f_i^{'} = \frac{(2C_i + \Delta\eta(C_i^{'} + f_i))f_{i+1}^{'} + (2C_i - \Delta\eta(C_i^{'} + f_i))f_{i-1}^{'}}{4C_i} \tag{6.13}$$

Applying Central difference to equation 6.12 yields:

Explicit:

$$g_i = \frac{(2C_i + \Delta\eta(C_i^{'} + Prf_i))g_{i+1} + (2C_i - \Delta\eta(C_i^{'} + Prf_i))g_{i-1} + 2\Delta\eta^2 BC_i f_i^{''}f_i^{''}}{4C_i} \tag{6.14}$$

The algorithm used to solve equations 6.13 and 6.14 is described in Appendix A.0.5.

6.3 Cohen and Reshotko Compressible Flow Similarity Solution

The Cohen and Reshotko (White, F. M. 1991; Cohen, C. B. and Reshotcko, E. 1955)solution for compressible flow based on the stagnation enthalpy by assuming a value of

$C = Pr = 1$, so the variable viscosity effects are only approximate and the Prandlt number effects are absent. This transforms equations 2.48 and 2.49 into:

$$f''' + ff'' + \beta(1 + S - f'f') = 0 \tag{6.15}$$

$$S'' + fS' = 0 \tag{6.16}$$

In this case, the g term is given by equation 6.4. In these equations f'' is related to shear stress, f' is related to velocity, f is related to the stream function, β is the pressure gradient related to the wedge angle and S is the stagnation enthalpy equivalent to $g - 1$, g is related to the temperature, and g' to the heat flux. The boundary layer thickness can be obtained by finding η where the local speed is 99% of the freestream velocity. In addition, the thermal boundary layer can be obtained by finding η where the term g is 1.01 for a hot wall and 0.99 for a cold wall. Applying a finite difference scheme to equations 6.15 and 6.16 yields:

Momentum:

Implicit:

$$(2 + \Delta\eta f_i)f'_{i+1} - (4 + 2\beta\Delta\eta^2 f'_i)f'_i + (2 - \Delta\eta f_i)f'_{i-1} + 2\beta\Delta\eta^2(1 + S_i) = 0 \tag{6.17}$$

Explicit:

$$f'_i = \frac{(2 + \Delta\eta f_i)f'_{i+1} + (2 - \Delta\eta f_i)f'_{i-1} + 2\beta\Delta\eta^2(1 + S_i)}{(4 + 2\beta\Delta\eta^2 f'_i)} \tag{6.18}$$

This work focuses on the explicit solution.

Stagnation enthalpy:

Implicit:

$$(2 + \Delta\eta f_i)S_{i+1} - 4S_i + (2 - \Delta\eta f_i)S_{i-1} = 0 \tag{6.19}$$

Explicit:

$$S_i = \frac{(2 + \Delta\eta f_i)S_{i+1} + (2 - \Delta\eta f_i)S_{i-1}}{4} \tag{6.20}$$

The term f for each iteration can be found using equation 2.21.

The boundary conditions are as follows:

At wall:

$$f = f^{'} = 0 \tag{6.21}$$

$$S = S_w \tag{6.22}$$

At infinity:

$$f^{'} = 1 \tag{6.23}$$

$$S = 0 \tag{6.24}$$

It is important to mention that for a hot wall condition, the stagnation enthalpy on the wall (S_w) is more than zero and for a cold wall condition the S_w is lower than zero. In the case of an adiabatic wall condition, S_w has a value of zero.

Equations 6.18 and 6.20 are solved simultaneously applying a similar algorithm as described in chapter 2 alongside equations 6.21, 6.22, 6.23 and 6.24.

6.4 Compressible Flow Similarity Solution Normalizing Temperature

According to Back (Back, L. H. 1970); and Bae and Emanuel (Bae, Y. Y. and Emanuel, G. 1996) the following Levy-Mangler transformation can be used to achieve similarity:

$$\eta = \frac{r^i \rho_e u_e}{(2\xi)^{1/2}} \int_0^y \frac{\rho}{\rho_e} dy \tag{6.25}$$

$$\xi = \int_0^x \rho_e \mu_e u_e r^{2(i)} dx \tag{6.26}$$

Where: η and ξ the similarity coordinates, r is the radius of curvature, ρ_e is the density at boundary layer edge, μ_e is the viscosity at the boundary layer edge, u_e is the velocity at the boundary layer edge, x is the coordinate parallel to the flow and y is the coordinate perpendicular to the flow.

When the i term in equations 6.27 and 6.28 is zero the flow becomes that of a plane flow:

$$\eta = \frac{\rho_e u_e}{(2\xi)^{1/2}} \int_0^y \frac{\rho}{\rho_e} dy \tag{6.27}$$

$$\xi = \int_0^x \rho_e \mu_e u_e dx \tag{6.28}$$

Applying this transformation to the compressible flow boundary layer equations yields (Back, L. H. 1970; Bae, Y. Y. and Emanuel, G. 1996):

Momentum:

$$(Cf^{''})^{'} + ff^{''} + \overline{\beta}(g - (f^{'})^2) = 0 \tag{6.29}$$

Energy:

$$[(C/Pr)g^{'}]^{'} + fg^{'} + S[2C(1 - 1/Pr)f^{'}f^{''}]^{'} = 0 \tag{6.30}$$

Where: $C = \rho\mu/\rho_e\mu_e$ is the density viscosity product, $\overline{\beta}$ is the acceleration parameter, S (speed parameter) is the ratio of kinetic energy to total enthalpy in the free stream.

Finally, assuming a linear density viscosity product or $C = 1$ and Prandlt (Pr) number of one equations 6.29 and 6.30 become (Back, L. H. 1970; Bae, Y. Y. and Emanuel, G. 1996):

Momentum:

$$f^{'''} + ff^{''} + \overline{\beta}[G(1 - g_w) + g_w - (f^{'})^2] = 0 \tag{6.31}$$

Energy:

$$G^{''} + fG^{'} = 0 \tag{6.32}$$

Where:

$$G = \frac{g - g_w}{1 - g_w} \tag{6.33}$$

In equation 6.31 and 6.32: f, $f^{'}$ and $f^{''}$ are associated to the stream, velocity and shear stress of the flow; and G and $G^{'}$ are associated with the temperature and heat flux. In this case, G is a normalization of g. In addition, g_w is associated with the wall temperature.

Note: Prime ($'$) indicate differentiation with respect to η.

The boundary conditions of equations 6.31 and 6.32 are as follows:

$$f(0) = f^{'}(0) = 0 \tag{6.34}$$

$$G(0) = 0 \tag{6.35}$$

$$f^{'}(\infty) = 1 \tag{6.36}$$

$$G(\infty) = 1 \tag{6.37}$$

Here, the wall is the coordinate $\eta = 0$ and the freestream is at η when it tends to infinity. In addition, it is important to mention that for a hot wall g_w is higher than one, that for an adiabatic case g_w has a value equal to one, and for a cold wall case g_w is lower than one. In order to apply FDM to equations 6.31 and 6.32, they must be written in terms of the variable for the starting and final conditions are known. In this case, the f' and G terms as:

Momentum:

$$\frac{\partial^2 f^{'}}{\partial \eta^2} + f\frac{\partial f^{'}}{\partial \eta} + \overline{\beta}[G(1 - g_w) + g_w - f^{'}f^{'}] = 0 \tag{6.38}$$

Energy:

$$\frac{\partial^2 G}{\partial \eta^2} + f\frac{\partial G}{\partial \eta} = 0 \tag{6.39}$$

Applying FDM to equations 6.38 and 6.39 yields the following:

Momentum:

$$f_i^{'} = \frac{[2 + f_i\Delta\eta]f_{i+1}^{'} + [2 - f_i\Delta\eta]f_{i-1}^{'} + 2\Delta\eta^2\overline{\beta}C_A}{4 + 2\overline{\beta}\Delta\eta^2 f_i^{'}} \tag{6.40}$$

$$C_A = G_w(1 - g_w) + g_w \tag{6.41}$$

Energy:

$$G_i = \frac{[2 + f_i\Delta\eta]G_{i+1} + [2 - f_i\Delta\eta]G_{i-1}}{4} \tag{6.42}$$

In this case, the f term can be obtained by a modified Forward Euler:

$$f_{i+1} = f_i + \Delta\eta\frac{f'_{i+1} + f'_i}{2} \tag{6.43}$$

Equations 6.40, 6.42, and 6.43 are solved simultaneously by applying a similar algorithm as described in chapter 2 alongside boundary conditions 6.34, 6.35, 6.36 and 6.37. Finally, the f'' and G' terms are obtained using an FDM numerical derivative. The $\eta_{f'=99\%}$ can be obtained by finding the coordinate η where f' equals 0.99 and $\eta_{G=99\%}$ were G equal 0.99. Once these values are found the Momentum and Thermal Boundary Layer thicknesses can be found as (Back, L. H. 1970):

$$\frac{\delta}{\overline{x}}\sqrt{Re_{\overline{x}}} = \sqrt{2}\int_0^{\eta_{f'=99\%}} \frac{G(1 - g_w) + g_w - Sf'f'}{1 - S}d\eta \tag{6.44}$$

$$\frac{\delta_t}{\overline{x}}\sqrt{Re_{\overline{x}}} = \sqrt{2}\int_0^{\eta_{G'=99\%}} \frac{G(1 - g_w) + g_w - Sf'f'}{1 - S}d\eta \tag{6.45}$$

Where the S parameter is the flow speed parameter, which is the ratio of the total kinetic energy to the total enthalpy in the freestream. This term takes into account the Mach number effects.

The thermal-to-momentum boundary layer thicknesses ratio can be obtained as:

$$\delta_{ratio} = \frac{\delta_t}{\delta} \tag{6.46}$$

6.5 Compressible Flow with Radiation Similarity Solution

The boundary layer equations for compressible flow (Alao, F. I. and Folarin, S. B. 2013):

Continuity:

$$\frac{\partial \rho u}{\partial x} + \frac{\partial \rho v}{\partial y} = 0 \tag{6.47}$$

X-Momentum:

$$u\frac{\partial u}{\partial x} + v\frac{\partial u}{\partial y} = \frac{-1}{\rho}\frac{\partial P}{\partial x} + \frac{1}{\rho}\frac{\partial}{\partial y}\left(\mu\frac{\partial u}{\partial y}\right) \tag{6.48}$$

Energy:

$$\rho C_p\left[u\frac{\partial T}{\partial x} + v\frac{\partial T}{\partial y}\right] - u\frac{\partial P}{\partial x} = \frac{\partial}{\partial y}\left(k\frac{\partial T}{\partial y}\right) + \mu\left(\frac{\partial u}{\partial y}\right)^2 - \frac{1}{\rho C_p}\left(\frac{\partial q_r}{\partial y}\right) \tag{6.49}$$

Where q_r is considered to be the Roseland approximation for radiation heat flux as (Alao, F. I. and Folarin, S. B. 2013):

$$q_r = \frac{-4\sigma}{3k^*}\frac{\partial T^4}{\partial y} \tag{6.50}$$

Where:

$$T^4 = 4T_\infty^3 T - 3T_\infty^4 \tag{6.51}$$

In this case T is associated with the local temperature, σ is the Stephan-Boltzman constant, k^* is the absorption coefficient and T_∞ is the free stream temperature.

Stewartson transformation can be used to achieve similarity as (Alao, F. I. and Folarin, S. B. 2013):

$$Y = \frac{1}{\sqrt{\nu_0}} \int_0^y \frac{\rho}{\rho_0} dy \tag{6.52}$$

$$\rho u = \rho_0 \sqrt{\nu_0} \frac{\partial \psi}{\partial y} \tag{6.53}$$

Applying this transformation and the Roseland approximation to the Boundary Layer equations (equations 6.47, 6.48, and 6.49) yields the following:

Momentum:

$$\frac{\partial^2 \psi}{\partial x \partial Y} \frac{\partial \psi}{\partial Y} - \frac{\partial^2 \psi}{\partial Y^2} \frac{\partial \psi}{\partial x} = \frac{\partial^3 \psi}{\partial Y^3} + \frac{T}{T_1} U_e \frac{\partial U_e}{\partial x} \tag{6.54}$$

Energy:

$$\frac{\partial \psi}{\partial Y} \frac{\partial \theta}{\partial x} - \frac{\partial \psi}{\partial x} \frac{\partial \theta}{\partial Y} = \frac{\partial^2 \theta}{\partial Y^2} + R_a \frac{\partial^2 \theta}{\partial Y^2} \tag{6.55}$$

Where:

$$\theta = \frac{T - T_\infty}{T_w - T_\infty} \tag{6.56}$$

The term T refers to the local flow temperature, and the term T_1 refers to the flow temperature at the position where the perpendicular coordinate to the wall (y) tends to infinite.

In this case, R_a is called the radiative term, which is expressed as:

$$R_a = \frac{16 \sigma T_\infty^3}{C_p^2 \nu_0 3 k^*} \tag{6.57}$$

The similarity variables and coordinates can be found as:

$$\psi(x, Y) = x^\alpha f(\eta) \tag{6.58}$$

$$\theta(x, Y) = g(\eta) \tag{6.59}$$

$$\eta = \frac{Y}{x^{\gamma}} \tag{6.60}$$

According to (Mukhopadhyay, S. 2009), the term α is given as $1 - \gamma$. In this case $\gamma = (1 - m)/2$.

Applying these similarity variables to the equations 6.54 and 6.55 yields the following similarity equations ((Alao, F. I. and Folarin, S. B. 2013):

Momentum:

$$f''' + \frac{T}{T_1}m - mf'f' + \left(\frac{1+m}{2}\right)ff'' = 0 \tag{6.61}$$

Energy:

$$2(3Pr + 4Q)g'' + 3Pr(1 + m)fg' = 0 \tag{6.62}$$

Where f is associated with the stream function, f' is related to the velocity profile, f'' is related to the flow shear stress, g is related to temperature and g' to heat flux. In this case m is the power la parameter related to the pressure gradient as:

$$\beta = \frac{2m}{m+1} \tag{6.63}$$

In this case, the thermal radiation Q term is related to R_a as:

$$1 + R_a = \frac{3Pr + 4Q}{3Pr} \tag{6.64}$$

According to (Alao, F. I. and Folarin, S. B. 2013) due to the presence of temperature T, a function S that defines the relationship between temperature and Mach number M is defined as:

$$\frac{T}{T_1} = (1+S)(1+A) - Af^{'}f^{'} \tag{6.65}$$

$$A = \frac{\gamma - 1}{2}M^2 \tag{6.66}$$

Applying equation 6.65 to equation 6.61 yields:

$$f^{'''} + m(1+A)[(1+S) - f^{'}f^{'}] + \left(\frac{1+m}{2}\right)ff^{''} = 0 \tag{6.67}$$

According to (Alao, F. I. and Folarin, S. B. 2013), $(1+S)$ can be approximated as:

$$(1+S) = 0.2g + 0.1 \tag{6.68}$$

Applying this approximation to equation 6.67 gives:

$$f^{'''} + m(1+A)[0.2g + 0.1 - f^{'}f^{'}] + \left(\frac{1+m}{2}\right)ff^{''} = 0 \tag{6.69}$$

Boundary Conditions:

$$f(0) = f^{'}(0) = 0 \tag{6.70}$$

$$g(0) = 1 \tag{6.71}$$

$$f^{'}(\infty) = 1 \tag{6.72}$$

$$g(\infty) = 0 \tag{6.73}$$

In order to apply FDM to equations 6.69 and 6.62, they must be written in terms of

the variables that the starting and final conditions are known. In this case, the $f^{'}$ and g terms:

$$\frac{\partial^2 f^{'}}{\partial \eta^2} + m(1+A)[(0.2g+0.1) - f^{'}f^{'}] + \left(\frac{1+m}{2}\right) f \frac{\partial f^{'}}{\partial \eta} = 0 \tag{6.74}$$

$$(3Pr+4Q)\frac{\partial^2 g}{\partial \eta^2} + 3Pr\left(\frac{1+m}{2}\right) f \frac{\partial g}{\partial \eta} = 0 \tag{6.75}$$

Applying FDM to equations 6.74 and 6.75 yields:

$$f_i^{'} = \frac{[4+(1+m)\Delta\eta f_i]f_{i+1}^{'} + [4-(1+m)\Delta\eta f_i]f_{i-1}^{'} + B}{8+4\Delta\eta^2 m(1+A)f_i^{'}} \tag{6.76}$$

$$B = 4\Delta\eta^2 m(1+A)[0.2g+0.1] \tag{6.77}$$

$$g_i = \frac{[4D+3Pr(1+m)\Delta\eta f_i]g_{i+1} + [4D-3Pr(1+m)\Delta\eta f_i]g_{i-1}}{8D} \tag{6.78}$$

$$D = 3Pr+4Q \tag{6.79}$$

The f term can be obtained by a modified forward Euler as:

$$f_{i+1} = f_i + \Delta\eta \frac{f_{i+1}^{'} + f_i^{'}}{2} \tag{6.80}$$

Equations 6.76, 6.78, and 6.80 can be solved by applying a similar algorithm as described in chapter 2 alongside boundary conditions 6.70, 6.71, 6.72 and 6.73. Finally, the terms $f^{''}$ and $g^{'}$ are obtained using a FDM numerical derivative.

6.6 Compressible Boundary Layers Studies

Figure 6.1 show the compressible $f^{'}$ distributions vs. η grid tests of the present result for a number of node N of 100, 1000 and 5000 compared with White's (White, F. M. 1991) Blasius solution at a Mach number of 5 based on equation 6.1. It can be observed that when the C term is 1 in equation 6.1 the compressible flat plate solution is coincident with the Blasius solution for incompressible flow. Furthermore, the grid sensitivity analysis reveals that the computed $f^{'}$ profiles for all considered mesh densities (100, 1000, and 5000 nodes) closely overlap with one another, as well as with the Blasius solution. This convergence behavior confirms that a resolution of 5000 nodes yields results that are effectively indistinguishable from those obtained with coarser grids. For optimal computational resource utilization, a grid resolution of 1000 nodes is selected for subsequent analyses.

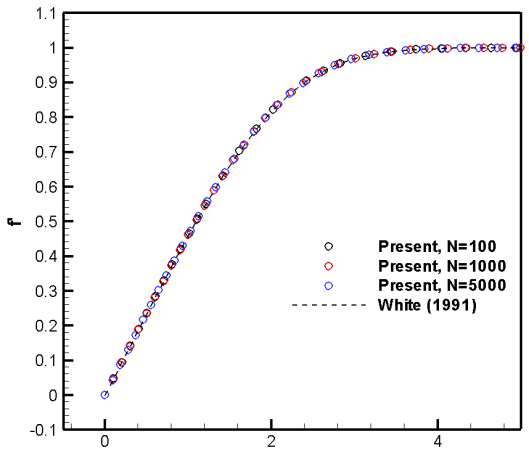

Figure 6.1: $f^{'}$ vs η comparison with White data (White, F. M. 1991) for a number of nodes N of 100, 1000, and 5000 at a Mach number of 5.

Figures 6.2 and 6.3 show the compressible distributions $f^{'}$ and $f^{''}$ vs η for Mach numbers of 2, 4, 6, 8, 10 and 12 based on equation 6.1. Figure 6.2 shows that all the $f^{'}$ curves start at a value of zero on the wall (due to the non-slip condition) and increase until they reach a value of one at the freestream. Also, it can be observed in the figure that as the Mach number increases, the curves tend to reach an infinite value of one faster or move leftwards, meaning that the boundary layer thickness decreases. Figure 6.3 shows that the $f^{''}$ curves start at the shear stress value on the wall and decrease until they reach a value of zero on the free stream. In the figure, it is seen that as the Mach number increases, the shear stress at the wall ($f^{''}(0)$) increases.

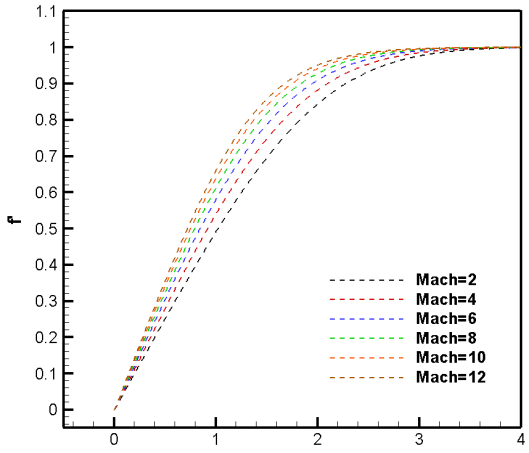

Figure 6.2: $f^{'}$ vs η for Mach 2 to 12

Figures 6.4 and 6.5 show the distribution of g and $g^{'}$ versus η for a Mach number of 2 to 12 based on equation 6.2. Figure 6.4 shows that as the Mach number increases, the temperature of the adiabatic wall increases. Figure 6.5 shows that the heat flux starts with a value of zero at the wall (adiabatic wall condition). Also, it can be seen from the figure that as the Mach number increases, the minimum absolute value of the heat flux increases. Finally, as η increases, the temperature term g reaches an infinite value of one, meaning that the flow has the same temperature as the freestream and the heat flux term $g^{'}$ reaches a value of zero due to the fact that the flow outside the boundary layer is inviscid and there is no thermal transport in that region.

Figure 6.6 shows the boundary layer $\eta_{99\%}$ and the thermal boundary layer η_T thicknesses distribution as the Mach number changes from 2 to 12 based on equations 6.1 and 6.2. It can be seen that as the Mach number increases, the $\eta_{99\%}$ decreases, meaning that the boundary layer gets closer to the wall, but opposite to incompressible flow, for compressible flow the η_T increases meaning that the thermal boundary layer thickness gets farther from the wall. It is also observed that both curves tend to have an asymptotic behavior as the Mach number increases.

Figure 6.7 shows the $f^{''}$ at Mach 12 vs η for different Power Law n at 1, 0.76 and 0.666. The shear stress term profile is based on equation 6.1. As n increases, the $f^{''}$ on the wall decreases. It is also observed that for the values of n for 0.76 and 0.666 the curves are near each other, except for $n = 1$. The Power Law with n of 0.666 produces the most conservative results, because it has the highest $f^{''}$ on the wall. But in this work, a Power Law n of 0.76 is going to be used.

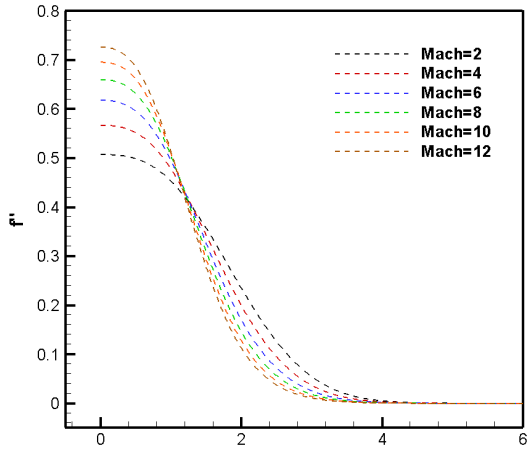

Figure 6.3: f'' vs η for Mach 2 to 12

Figure 6.8 shows the f'' at the wall vs Mach number for different Power Law n. As n decreases, the shear stress on the wall increases. It is also observed that for values of n equal to 0.76 and 0.666 the curves are near each other but as they get farther away to high Mach numbers the curves start to diverge. For n equal to one, the solution decouples from the energy equation and the Blasius wall shear stress always remains constant at 0.4696. Also, it is important to mention that the wall shear stress value is always highest at $n = 0.666$, followed by $n = 0.76$ and $n = 1$.

Figures 6.9 and 6.10 show f' and f'' vs η for a Mach number of 5 and a Pr number of 2, 1, 0.7 and 0.2 based on equations 6.1 and 6.2. In Figure 6.9, it is observed that as the Pr number decreases, the curves move to the right, meaning that the Boundary Layer thickness increases. When comparing Figure 6.9 to 6.2, it can be seen that the Mach number has a greater effect on the flow than the Pr number. In addition, it is observed in Figure 6.10 that as the Pr number decreases, the shear stress on the wall decreases.

Figures 6.11 and 6.12 show the temperature g and the heat flux g' vs. η for a Mach number of 5 and a Pr number of 2, 1, 0.7 and 0.2 based on equations 6.1 and 6.2. It is observed in Figure 6.11 that as the Pr number increases, the thermal boundary layer thickness decreases. When comparing Figure 6.11 to 6.4, it can be seen that the Mach number has a greater effect on the flow than the Pr number. Also, in Figure 6.12, it is observed that as the Pr number increases, the minimum value of the heat flux g' increases in a negative direction. Finally, it is worth mentioning that the heat flux is zero at the wall, meaning that there is no heat transfer, and zero at the freestream due to the fact that the temperature of the fluid is equal to the freestream temperature.

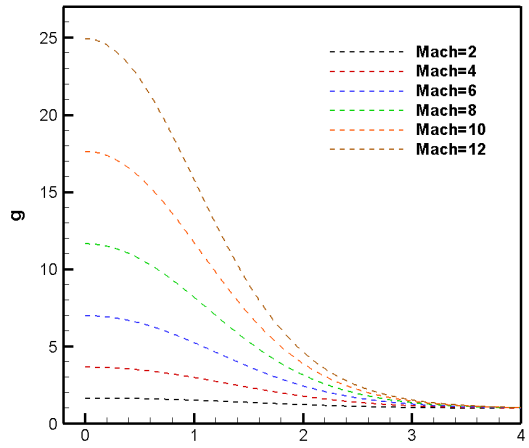

Figure 6.4: g vs. η from Mach 2 to 12

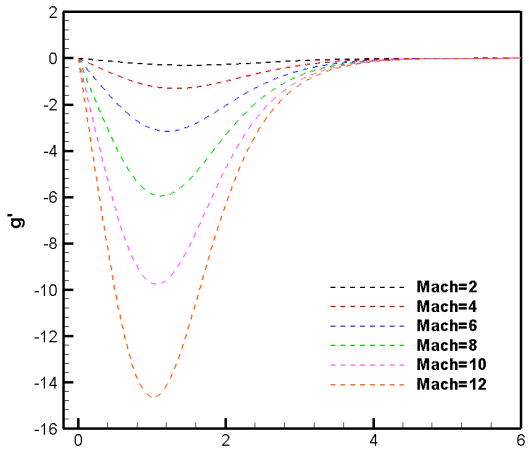

Figure 6.5: $g^{'}$ vs. η from Mach 2 to 12

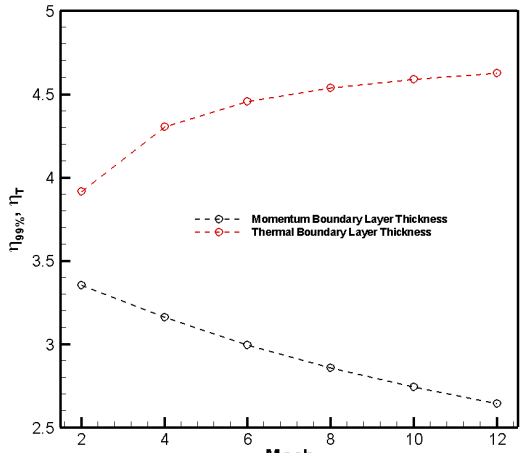

Figure 6.6: $\eta_{99\%}$ and η_T vs. Mach.

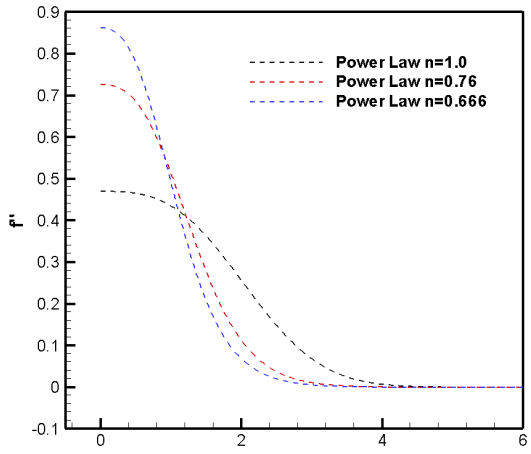

Figure 6.7: f'' vs. η at Mach number at 12 for a Power Law n of 1, 0.76, 0.666.

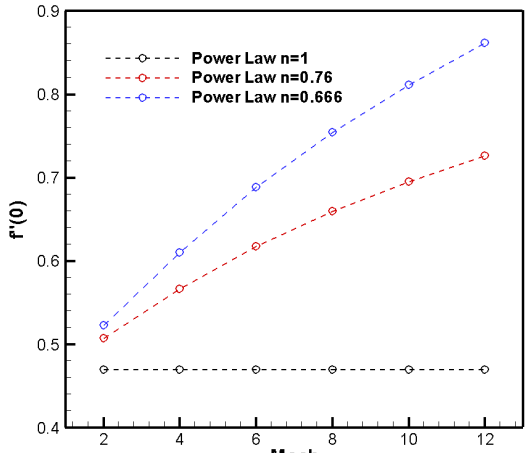

Figure 6.8: $f''(0)$ vs. Mach 12 for Power Law $n = 1, 0.76, 0.666$.

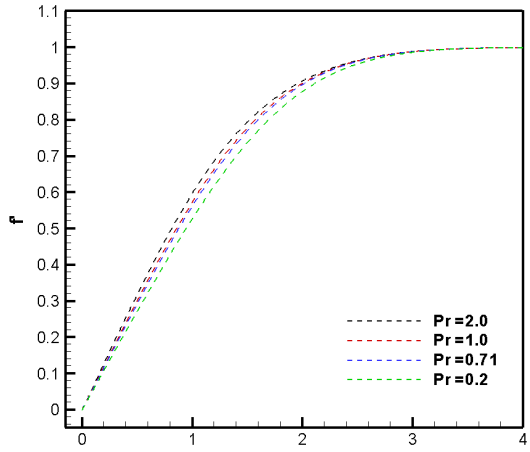

Figure 6.9: f' vs η for Pr numbers of 2, 1, 0.7, 0.2

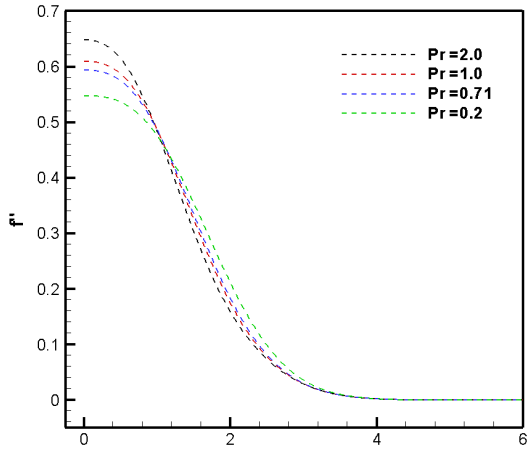

Figure 6.10: f'' vs η for Pr numbers of 2, 1, 0.7, 0.2

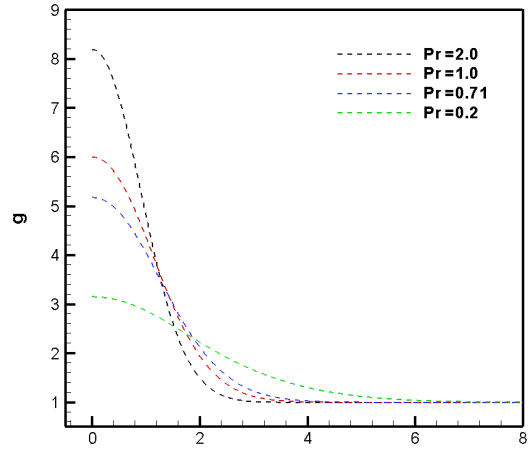

Figure 6.11: g vs η for Pr numbers of 2, 1, 0.7, 0.2.

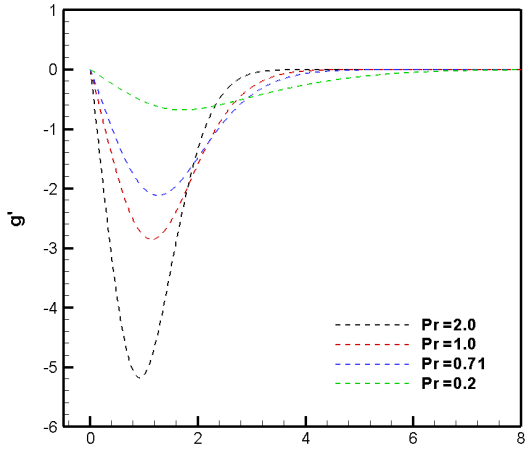

Figure 6.12: $g^{'}$ vs η for Pr numbers of 2, 1, 0.7, 0.2.

6.7 Cohen and Reshotko Compressible Flow Studies

Figures 6.13, 6.14, 6.15 and 6.16 show the compressible $f^{'}$, $f^{''}$, g and $g^{'}$ distributions vs η grid tests of the present result for a wall temperature $g(0)$ of 2 or a wall stagnation enthalpy $S(0)$ of 1 at a pressure gradient of 2 for a number of nodes N of 100, 1000 and 5000 compared to the Cohen and Reshotko (Cohen, C. B. and Reshotcko, E. 1955) solution. The figures show that the present solution for different numbers of nodes N is almost coincident with each other and with the Cohen-Reshotko solution, meaning that for this number of nodes, their results are almost the same, as expected. Thus, a number of N nodes of 1000 will be chosen for the subsequent studies.

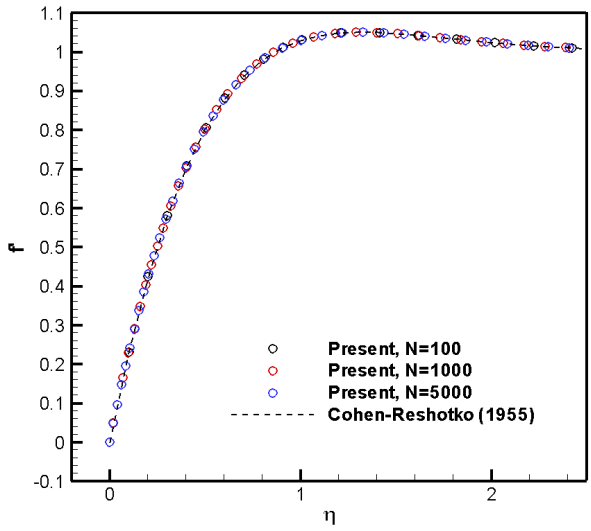

Figure 6.13: $f^{'}$ vs η comparison with Cohen-Reshotko data (Cohen, C. B. and Reshotcko, E. 1955) a number of nodes N of 100, 1000 and 5000

Figure 6.17 shows the Cohen-Reshotko compressible f' distribution vs. η for a wall temperature g_w of 2 or a wall stagnation enthalpy S_w of 1; and β from -0.1295 to 2. The figure shows, as seen in the incompressible case, that as β decreases the curve tends to become more S-shaped. As stated before, this happens because as the β decreases, the flow enters an expansion and the pressure gradient becomes adverse as it decelerates, leading to a flow separation; and as the β increases, the flow enters a favorable pressure gradient and accelerates decreasing the thickness of the Boundary Layer. The overshoot at a pressure gradient of 2 for a g_w of 2 is due to the fact that when the flow is heated, the density within the boundary layer is lowered so that the flow is accelerated more than the external flow by the external pressure forces (Cohen, C. B. and Reshotcko, E. 1955).

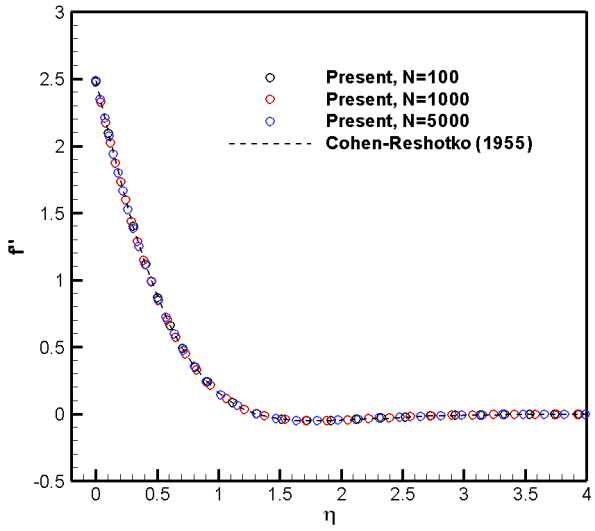

Figure 6.14: f'' vs η comparison with Cohen-Reshotko (Cohen, C. B. and Reshotcko, E. 1955) data for a number of nodes N of 100, 1000 and 5000

Figure 6.18 shows the Cohen and Reshotko compressible f'' distribution vs. η of the present result for β between -0.1295 and 2. As in the incompressible case, the figure shows that as β decreases the wall shear stress or $f''(0)$ decreases until it reaches a value of zero. As stated, before this happens because as the β decreases, the flow enters an expansion and the pressure gradient becomes adverse until the point where the flow separates and the shear stress reaches a value of zero.

Figures 6.19 and 6.20 show the Cohen-Reshotko compressible g and $g^{'}$ distributions vs η of the present result for a β from -0.1295 to 2 at a wall temperature g_w of 2 or a wall stagnation enthalpy S_w of 1. It can be seen in Figure 6.19 that g (related to temperature) starts at a value of g_w on the wall and decreases until it reaches an infinite value of one where the local temperature is equal to the freestream temperature. Figure 6.20 shows the $g^{'}$ (related to the heat flux). It is observed that $g^{'}$ starts with a high value on the wall and decreases until it reaches an infinite value of zero where there is no more heat transfer due to the fact that the local temperature is equal to that of the freestream. In addition, as β increases, the thickness of the thermal boundary layer decreases. It is important to mention that as the β increases, the heat flux in the wall increases in the negative direction. This behavior is quite similar to an incompressible flow.

Figure 6.21 shows the Cohen-Reshotko compressible distribution $\eta_{99\%}$ and η_T (momentum and thermal boundary layer thicknesses) vs. β at g_w of 2 or S_w of 1. As stated before, it can be seen in the figure that as β increases, the thicknesses of the momentum boundary

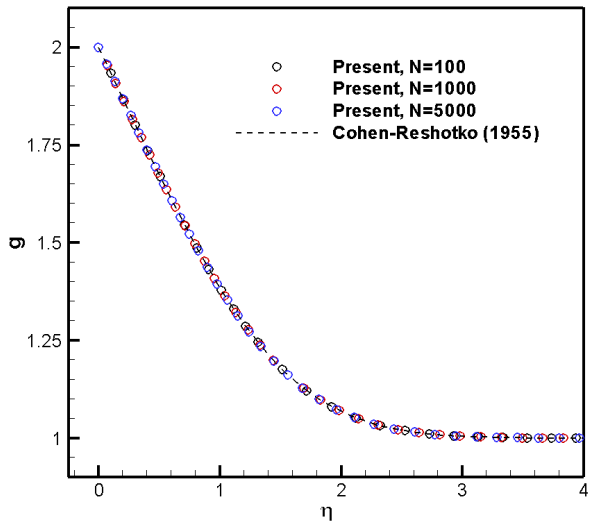

Figure 6.15: g vs η comparison with Cohen-Reshotko (Cohen, C. B. and Reshotcko, E. 1955) data for a number of nodes N of 100, 1000 and 5000

layer and the thermal boundary layer become closer to the wall and tend to reach an asymptotic condition.

Figures 6.22 and 6.23 show the Cohen-Reshotko compressible $f^{'}$ and $f^{''}$ distributions vs η for g_w from 0 to 2 or S_w from -1 to 1 at a β of -0.1295. Figure 6.22 shows that as g_w increases, the curve resembles a $'S'$ shape and the boundary layer thickens. Next, in Figure 6.23, it is seen that as the g_w increases, the shear stress on the wall decreases until it reaches a value of zero where flow separation occurs. This means that decreasing g_w (associated with fluid temperature) delays flow separation.

Figures 6.24 and 6.25 show the Cohen-Reshotko compressible g and $g^{'}$ distributions vs η for a g_w from 0 to 2 or S_w from -1 to 1 at a β of -0.1295. It can be observed in Figure 6.24 that as η increases: for the cold wall ($g_w < 1$) condition, there is an increase in temperature; for the adiabatic ($g_w = 1$) case, the temperature remains constant; and for the hot wall ($g > 1$) case the temperature decreases. It can be seen that all the curves start with a value at the wall and then increase (cold wall), decrease (hot wall), or remain constant (adiabatic wall) until they reach the freestream condition. Next, in Figure 6.25 it is seen that as the g_w decreases the heat flux at the wall increases in the positive direction; when g_w equals zero there is no heat flux at the wall; and as the g_w increases the heat flux at the wall increases in the negative direction. This means that when the heat flux is positive (cold wall case) there is a heat gain at the wall; when the heat flux is zero there is no heat transfer so an adiabatic wall condition is reached; and

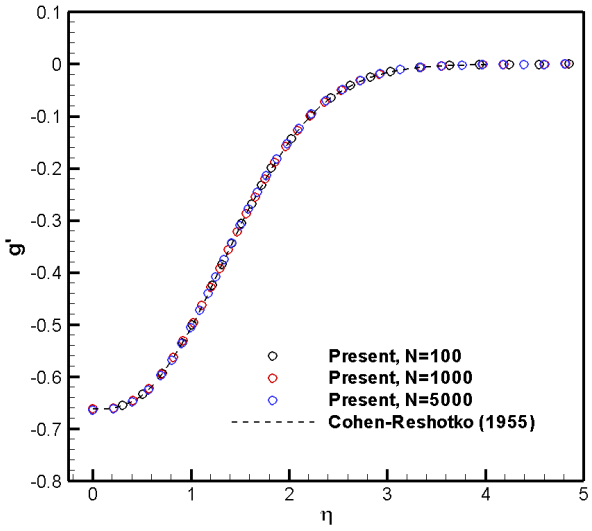

Figure 6.16: $g^{'}$ vs η comparison with Cohen-Reshotko (Cohen, C. B. and Reshotcko, E. 1955) data for a number of nodes N of 100, 1000 and 5000

finally, when the heat flux is negative (hot wall) there is a heat loss at the wall.

Figures 6.26 and 6.27 show the present and Cohen-Reshotko compressible $f^{''}$ at the wall vs β for a g_w from 0 to 2 or a S_w from -1 to 1. It can be seen in the figure that as the g_w increases for positive pressure gradients, the shear stress on the wall increases, and for negative pressure gradients, as the g_w decreases, the shear stress at the wall increases. This means that as the flow gets colder, the boundary layer thickness decreases and the pressure gradient where the flow separation occurs increases. Also, the present data has a very good agreement with the Cohen-Reshotko data (Cohen, C. B. and Reshotcko, E. 1955).

Figure 6.28 shows the present and Cohen-Reshotko compressible $g_w^{'}$ on the wall versus β for a g_w from 0 to 2 or S_w from -1 to 1. It can be observed in the figure that for an g_w more than one (hot wall), as the pressure gradients increase in the positive direction the heat flux at the wall increases in a negative direction, and as the pressure gradients increase in the negative direction the heat flux at the wall increases in the positive direction. This means that for a hot wall, as the pressure gradient increases from negative to positive, more heat is transferred or lost from the wall to the environment. In the case for g_w less than one (cold wall), it can be observed that as the pressure gradient decreases, the heat flux at the wall decreases and as the pressure gradient increases, the heat flux at the wall increases. This means that for a cold wall, as the pressure gradient increases from negative to positive, the heat moves from the ambient to the wall, or there is a heat gain

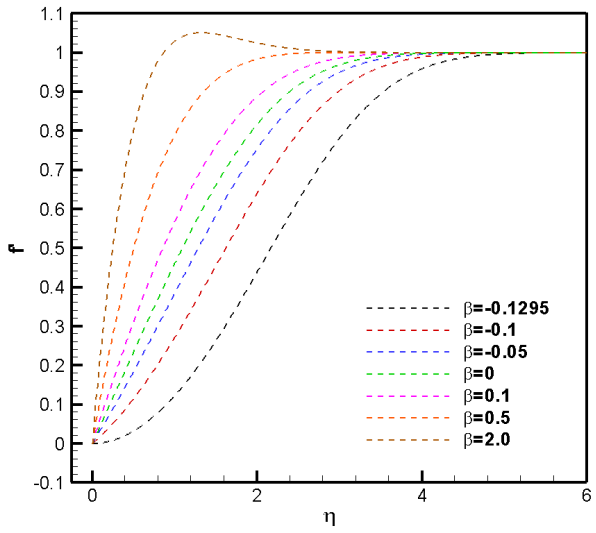

Figure 6.17: $f^{'}$ vs. η for β of -0.1295 to 2 at g_w of 2 or S_w of 1.

at the wall. In addition, it is seen that the present data are in very good agreement with the Cohen-Reshotko data (Cohen, C. B. and Reshotcko, E. 1955).

Figure 6.29 shows the present and Cohen-Reshotko compressible $\eta_{99\%}$ vs. β for a g_w from 0 to 2 or S_w from -1 to 1. It can be seen in the figure that as the g_w increases for a positive pressure gradient the boundary layer thickness decreases and for a negative pressure gradient the boundary layer thickness increases. Also, it is important to mention that as the flow gets colder the separation pressure gradient increases.

Figures 6.30 and 6.31 show the compressible η_T vs. β for a g_w for a hot and cold wall condition. It can be observed in Figure 6.30, the hot wall condition, that as the wall temperature g_w increases the thermal boundary layer thickness increases. Figure 6.31, cold wall condition, shows that as wall temperature g_w increases, the thickness of the thermal boundary layer decreases. In both studies, as the pressure gradient increases from negative to positive, the thermal boundary layer thickness decreases.

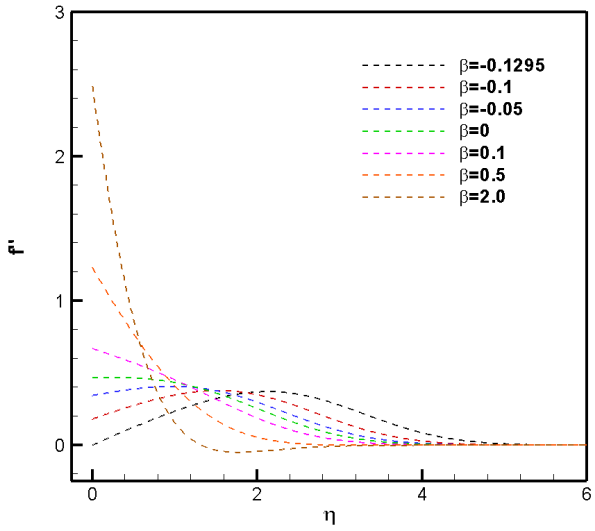

Figure 6.18: f'' vs. η for β -0.1295 to 2 at a g_w for 2 or S_w of 1

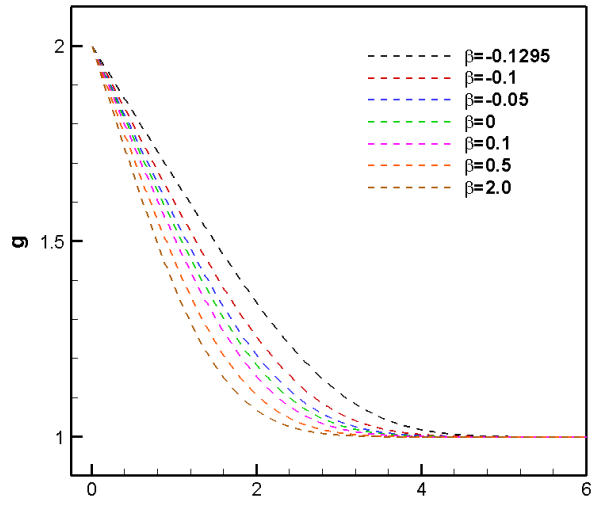

Figure 6.19: g vs. η for β -0.1295 to 2 at a g_w of 2 or S_w of 1 .

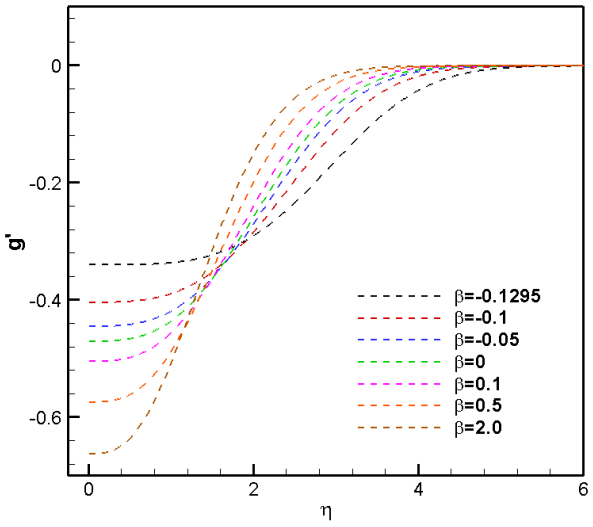

Figure 6.20: $g^{'}$ vs. η for β -0.1295 to 2 at g_w of 2 or S_w of 1.

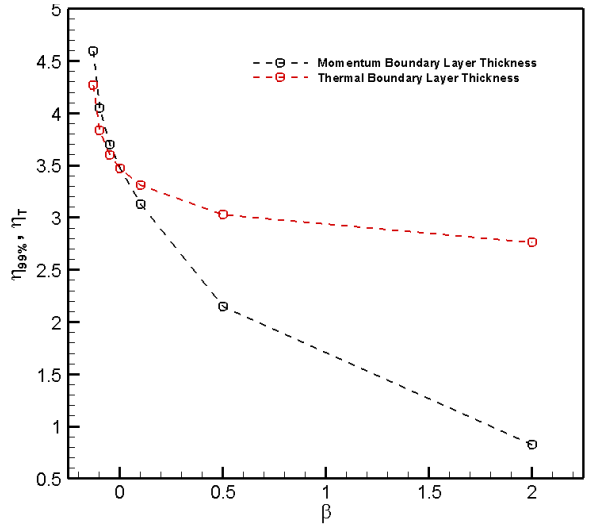

Figure 6.21: Effect of pressure gradient on Momentum and Thermal Boundary Layer thicknesses.

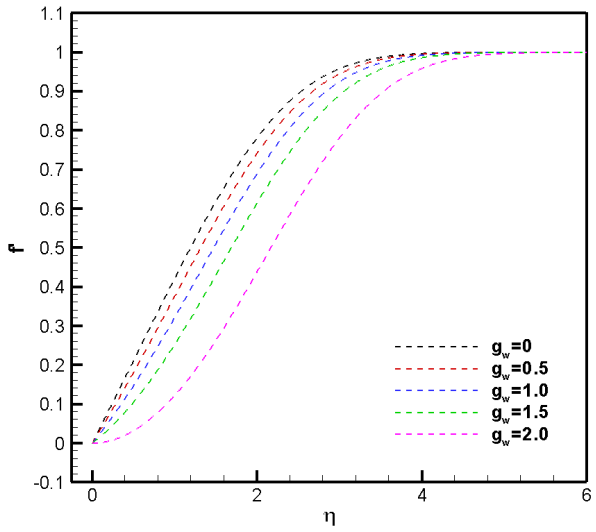

Figure 6.22: $f^{'}$ vs. η at β of -0.1295 for g_w 0 to 2 or S_w from -1 to 1.

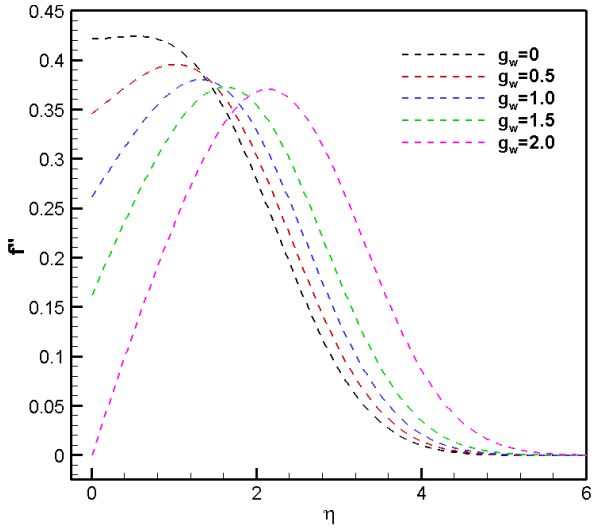

Figure 6.23: $f^{''}$ vs. η at β of -0.1295 for g_w from 0 to 2 or S_w from -1 to 1.

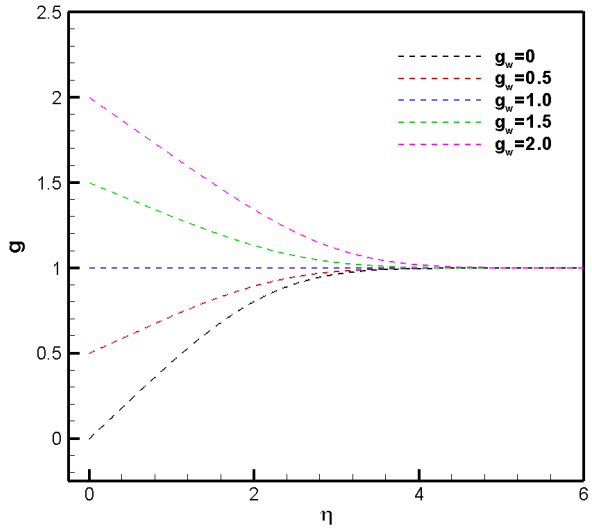

Figure 6.24: g vs. η at β of -0.1295 for g_w from 0 to 2 or S_w from -1 to 1.

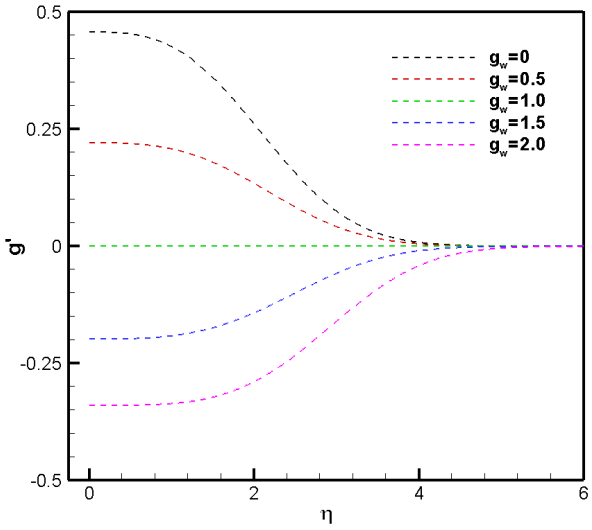

Figure 6.25: $g^{'}$ vs. η at β of -0.1295 for g_w from 0 to 2 or S_w from -1 to 1.

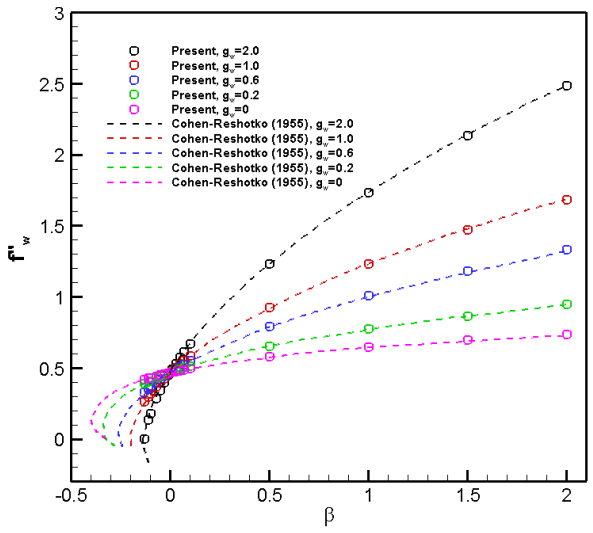

Figure 6.26: f''_w vs. β for g_w from 2 to 0 or S_w from 1 to -1.

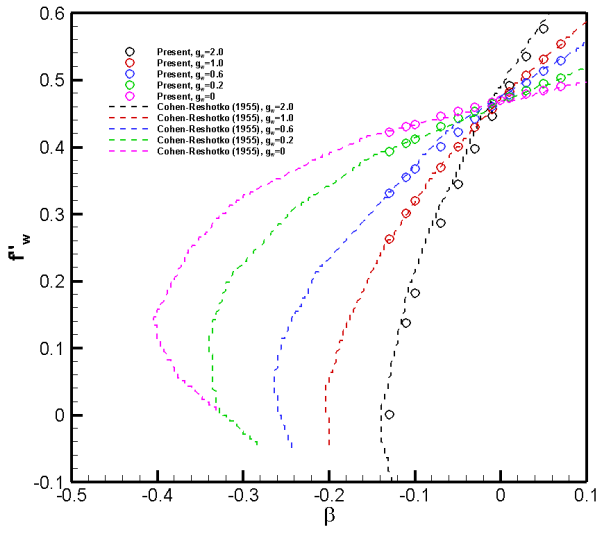

Figure 6.27: f''_w vs. β from -0.5 to 0.1 for g_w from 2 to 0 or S_w from 1 to -1.

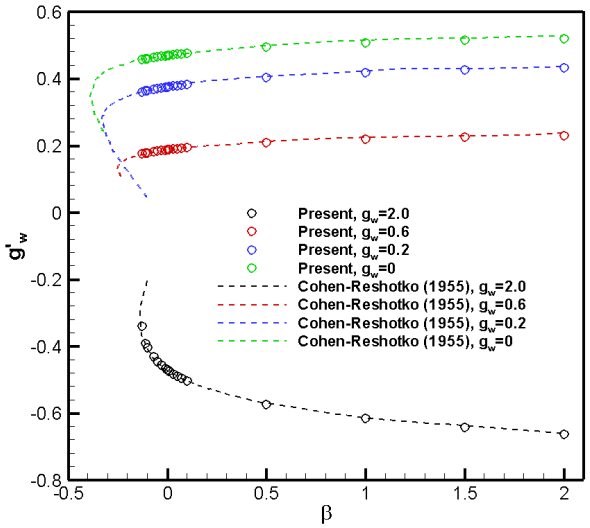

Figure 6.28: $g_w^{'}$ vs. β for g_w from 2 to 0 or S_w from 1 to -1.

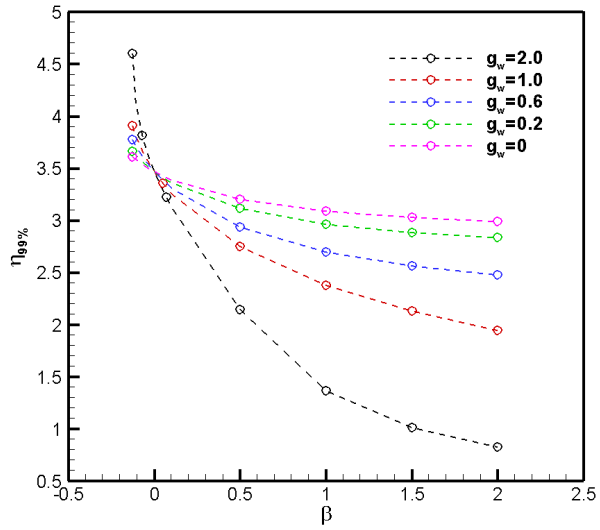

Figure 6.29: $\eta_{99\%}$ vs. β for g_w from 2 to 0 or S_w from 1 to -1.

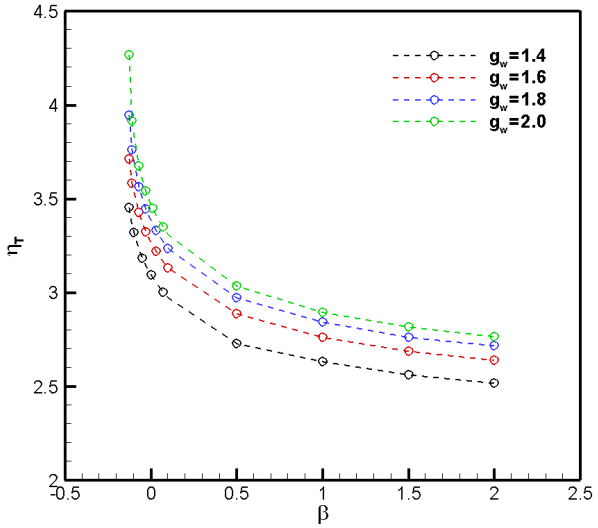

Figure 6.30: η_T vs. β for a hot wall condition

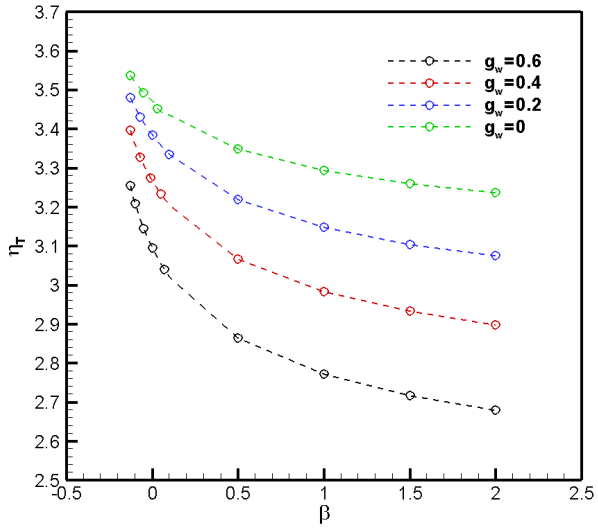

Figure 6.31: η_T vs. β for a cold wall condition

Table 6.1: Thermal to momentum boundary layer thicknesses ratio (δ_t/δ) present results

β	g_w	$S=0$	$S=0.25$	$S=0.5$	$S=0.75$	$S=0.9$
0.5	0	1.065	1.062	1.057	1.046	1.030
0.5	0.6	1.112	1.102	1.087	1.062	1.036
0.5	0.8	1.130	1.117	1.099	1.069	1.040
0.5	1.0	1.151	1.135	1.112	1.077	1.046
5.0	0	1.128	1.126	1.121	1.109	1.083
5.0	0.6	1.311	1.294	1.264	1.202	1.119
5.0	0.8	1.496	1.461	1.403	1.292	1.161
5.0	1.0	2.041	1.936	1.779	1.522	1.270

Table 6.2: Thermal to momentum boundary layer thicknesses ratio (δ_t/δ) Back (Back, L. H. 1970) results

β	g_w	$S=0$	$S=0.25$	$S=0.5$	$S=0.75$	$S=0.9$
0.5	0	1.07	1.066	1.061	1.048	1.03
0.5	0.6	1.116	1.104	1.088	1.059	1.031
0.5	0.8	1.138	1.123	1.101	1.067	1.034
0.5	1.0	1.151	1.133	1.108	1.069	1.035
5.0	0	1.14	1.138	1.133	1.12	1.093
5.0	0.6	1.326	1.307	1.276	1.211	1.124
5.0	0.8	1.512	1.474	1.414	1.3	1.164
5.0	1.0	2.042	1.934	1.773	1.512	1.258

6.8 Compressible Flow Similarity Solution Normalizing Temperature Study

Tables 6.1 and 6.2 show the thermal to momentum boundary layer thickness ratio of the present and Back (Back, L. H. 1970) results. It can be seen in both tables that as the wall temperature increases from a cold wall to an adiabatic wall and the pressure gradient increases this ratio increases. Also, it is important to mention that, according to these results, the thermal boundary layer thickness has a higher value than the momentum boundary layer thickness. The opposite effect was observed as the S parameter increased. Also, the present results are very near Back (Back, L. H. 1970) results with a minimum percent difference of 0.009% and a maximum percent difference of 1.120%.

6.9 Compressible Flow with Radiation Similarity Solution Study

Figures 6.32 and 6.33 show the compressible $f^{'}$ and g vs. η grid test comparison with Alao and Folarin results (Alao, F. I. and Folarin, S. B. 2013) for number of nodes N of 1000, 1500, 2000 at pressure gradient of 0.02, a thermal radiation parameter Q of 0.1, and a Mach number of zero for a Prandtl number of 0.5. It can be observed that the $f^{'}$ term starts with a value of zero at the wall (no-slip condition) and increases until it reaches a value of one at the free stream; and the g term starts with a value of one at the wall and decreases until it reaches a value of zero where the local temperature is equal to the temperature of the free stream. In addition, it can be seen that the curves for the different number of nodes are coincident and very near the results of Alao and Folarin (Alao, F. I. and Folarin, S. B. 2013), so a number of 1000 can be used without changing the precision of the studies.

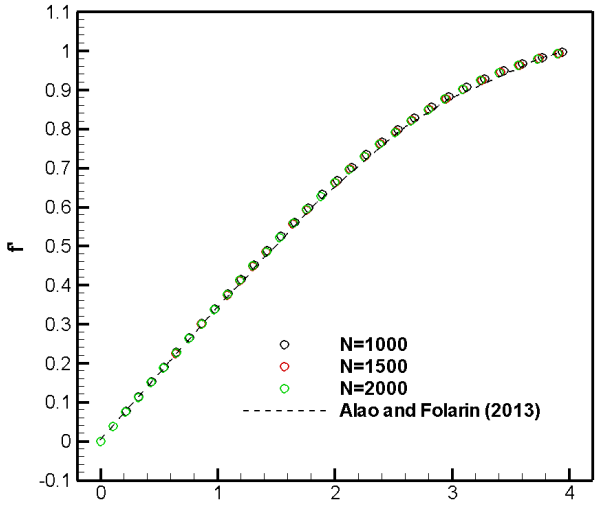

Figure 6.32: $f^{'}$ vs. η grid test comparison with Alao and Folarin (Alao, F. I. and Folarin, S. B. 2013)

Figures 6.34, 6.35 and 6.36 show the compressible $f^{'}$ vs. η for a radiation parameter Q of 0, 0.1, 0.2, 0.3, 0.4 and 0.5 for Mach number of 0.3 and adverse pressure gradient of -0.02, a zero pressure gradient and favorable pressure gradient of 0.02 at a Prandlt number of 0.71. It can be seen in the figures that the f' term starts from a value of zero at the wall and increases until it reaches a value of one, where the local velocity is equal to the free stream velocity. Finally, it is observed in Figures 6.34, 6.35, and 6.36 that

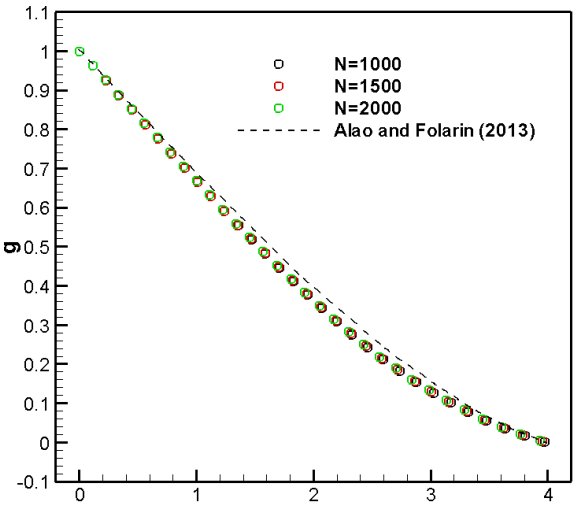

Figure 6.33: g vs. η grid test comparison with Alao and Folarin (Alao, F. I. and Folarin, S. B. 2013)

the curves coincide with each other, meaning that radiation has a negligible effect on the non-dimensional velocity profiles.

Figures 6.37, 6.38 and 6.39 show the compressible f'' vs. η for a radiation parameter Q of 0, 0.1, 0.2, 0.3, 0.4 and 0.5 for a Mach number of 0.3 for an adverse pressure gradient of -0.02, a zero pressure gradient and a favorable pressure gradient of 0.02 at a Prandtl number of 0.71. It can be observed in the figures that the radiation parameter has almost no effect on the shear stress at the wall. Also, it can be seen that the figures start with a high value at the wall and decrease to a value of zero at the free stream.

Figures 6.40, 6.41 and 6.42 show the compressible g vs. η for a radiation parameter Q of 0, 0.1, 0.2, 0.3, 0.4 and 0.5 at a Mach number of 0.3 for an adverse pressure gradient -0.02, a zero pressure gradient, and a favorable pressure gradient of 0.2 with a Prandtl number of 0.71. It can be seen in the figures that the temperature term g starts with a value of one on the wall where the local temperature is equal to the wall temperature and decreases until it reaches a value of zero on the free stream. Figures 6.40, 6.41, and 6.42 show that as the thermal radiative term Q increases, the thickness of the thermal or temperature boundary layer increases. Finally, it is observed that thermal radiation Q has a greater effect on the energy equation than on the momentum equation.

Figures 6.43, 6.44 and 6.45 show the compressible g' vs. η for a radiation parameter Q of 0, 0.1, 0.2, 0.3, 0.4 and 0.5 at a Mach number of 0.3 for an adverse pressure gradient

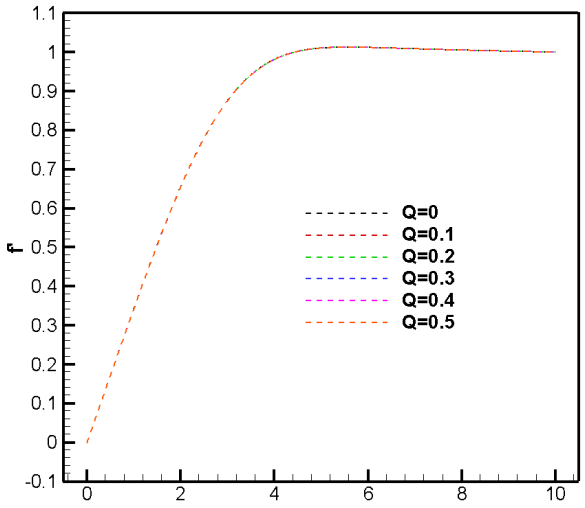

Figure 6.34: f' vs. η for different radiation parameters Q at Mach 0.3 for an adverse pressure gradient of -0.02

of -0.02, a zero pressure gradient and a favorable pressure gradient of 0.02 for a Prandlt number of 0.71. The figures indicate that the flow initiates with a nonzero heat flux at the wall, which subsequently diminishes to zero as the local temperature approaches the free-stream temperature, resulting in the cessation of heat transfer (inviscid flow region). It can be observed that as the radiation parameter increases in Figures 6.43, 6.44, and 6.45, the heat flux at the wall decreases toward zero. Compared to f'', it can be seen that the radiation parameter has a strong effect on g'.

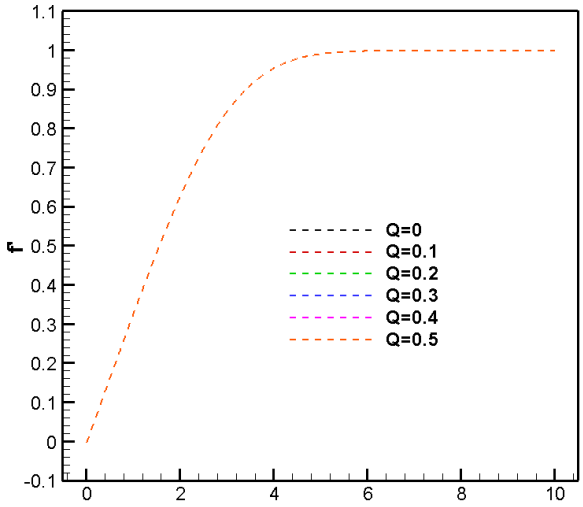

Figure 6.35: $f^{'}$ vs. η for different radiation parameters Q at Mach 0.3 for a zero pressure gradient

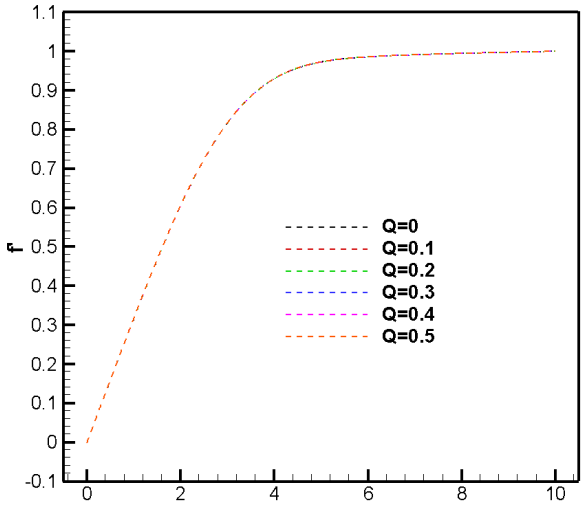

Figure 6.36: $f^{'}$ vs. η for different radiation parameters Q at Mach 0.3 for a favorable pressure gradient of one

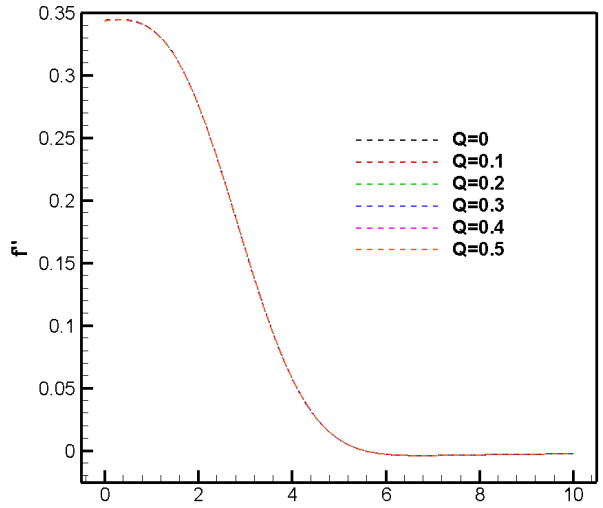

Figure 6.37: f'' vs. η for different radiation parameters Q at Mach 0.3 for an adverse pressure gradient of -0.02

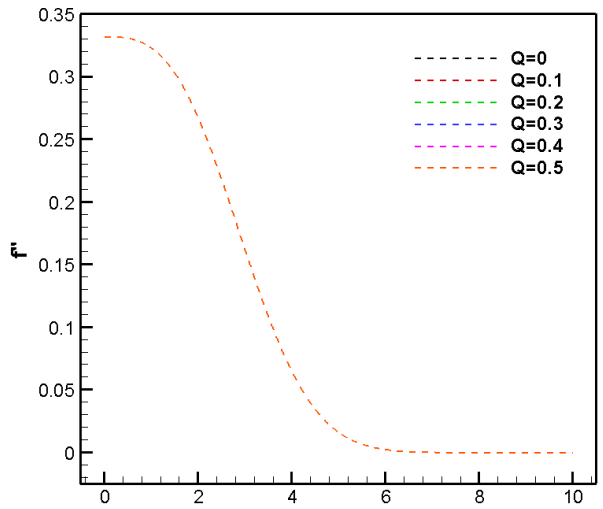

Figure 6.38: f'' vs. η for different radiation parameters Q at Mach 0.3 for a zero pressure gradient

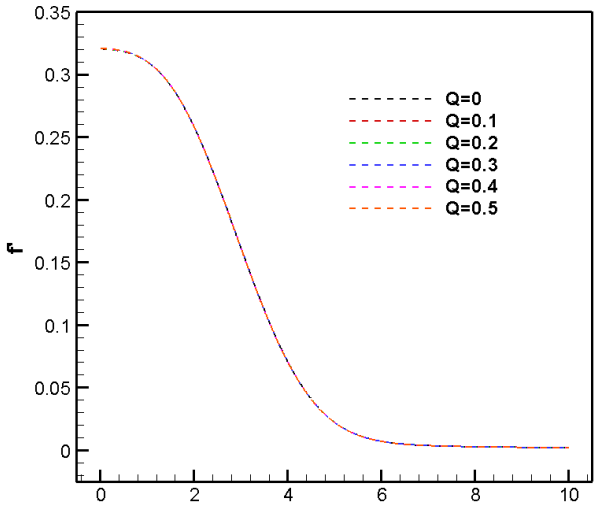

Figure 6.39: f'' vs. η for different radiation parameters Q at Mach 0.3 for a favorable pressure gradient of 0.2

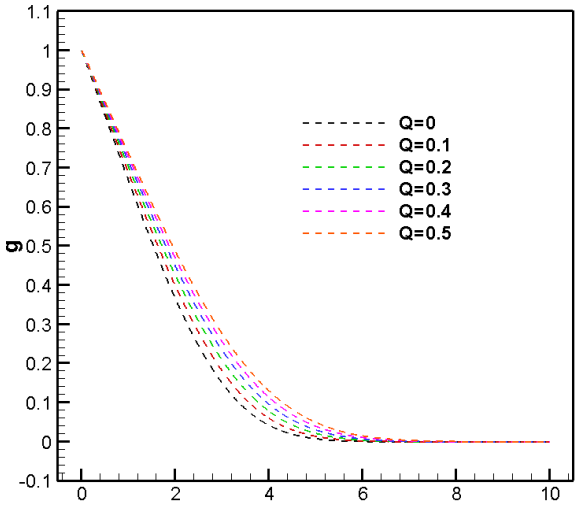

Figure 6.40: g vs. η for different radiation parameters Q at Mach 0.3 for an adverse pressure gradient of -0.02

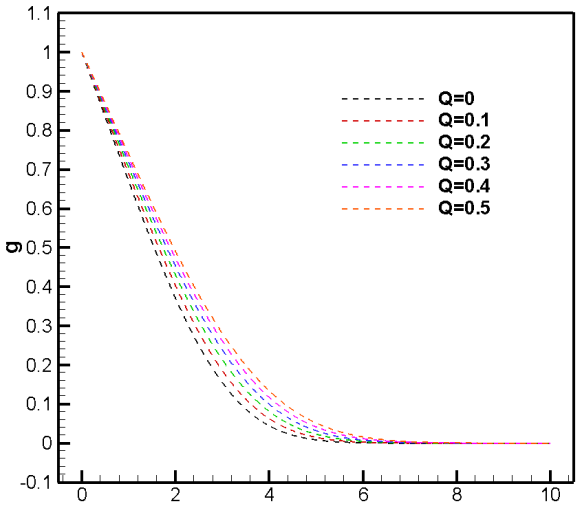

Figure 6.41: g vs. η for different radiation parameters Q at Mach 0.3 for a zero pressure gradient

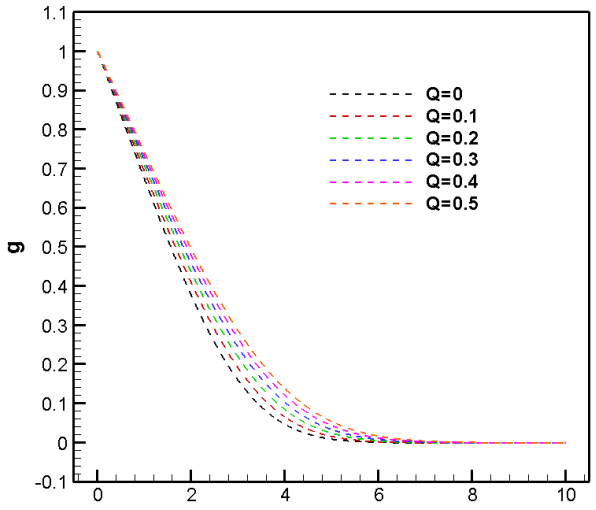

Figure 6.42: g vs. η for different radiation parameters Q at Mach 0.3 for a favorable pressure gradient of 0.02

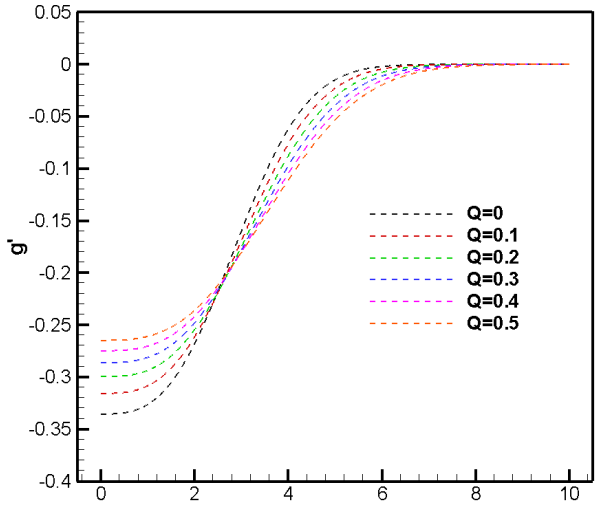

Figure 6.43: $g^{'}$ vs. η for different radiation parameters Q at Mach 0.3 for an adverse pressure gradient of -0.02

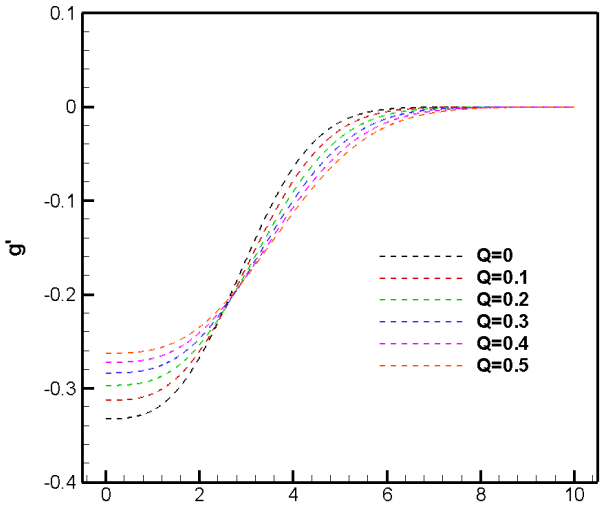

Figure 6.44: $g^{'}$ vs. η for different radiation parameters Q at Mach 0.3 for a zero pressure gradient

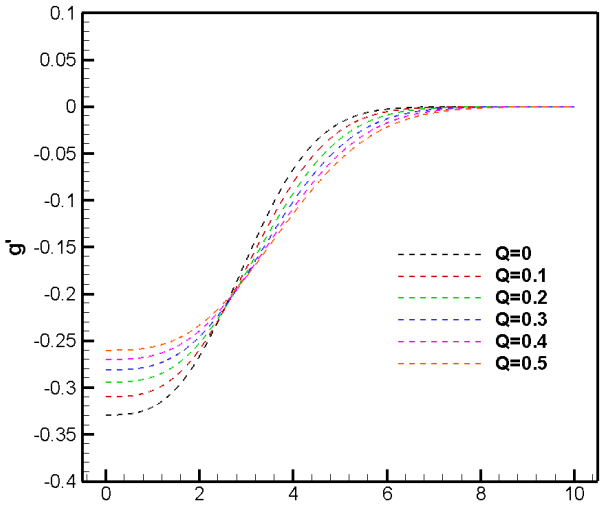

Figure 6.45: $g^{'}$ vs. η for different radiation parameters Q at Mach 0.3 for a favorable pressure gradient of 0.02

6.10 Chapter 6 Conclusions

The compressible flow solution for the case $C = 1$ was effectively validated and a number of nodes of 1000 was chosen. It was observed that as the Mach number increased, the shear stress at the wall increased, the boundary layer thickness decreased,, and the thermal boundary layer thickness increased. In the case of viscosity for a Power Law parameter of 1, 0.76 and 0.666 it was seen that the highest value of the shear stress at the wall was obtained with the Power Law parameter of 0.666, followed by 0.76 and 1. The Cohen and Reshotko solution was effectively validated for the g_w of 2 or S_w of 1 at a β of 2. A number of nodes of 1000 was chosen to have good precision. As stated before, it was observed that as the pressure gradient increases, the f' curves tend to move to the left and for a pressure gradient of 2 the result was an f' velocity profile overshoot for the g_w of 2 or S_w of 1 case. In the case of f'', it was observed that as the pressure gradient increases, the shear stress on the wall increases. In terms of temperature, for favorable pressure gradients as the wall temperature increases, the wall shear stress increases; and for adverse pressure gradients, the opposite effect can be seen. It was observed that as the temperature decreases, the momentum boundary layer thickness decreases for adverse pressure gradients and increases for favorable pressure gradients. It is also noteworthy that for a heated wall scenario, an increase in wall temperature leads to an expansion of the thermal boundary layer thickness. Conversely, for a cooled wall scenario, elevating the wall temperature results in a reduction of the thermal boundary layer thickness. The similarity equations governing compressible flow, with temperature normalization, were solved utilizing an explicit finite difference scheme. The ratio of thermal to momentum boundary layer thicknesses was computed using equation 6.46. It was observed that as the pressure gradient and wall temperature increase, the thermal-to-momentum boundary layer thickness ratio exhibits a corresponding increase. Conversely, an increase in the S parameter leads to a reduction in this ratio. Finally, upon comparing the present results with those of Back (Back, L. H. 1970), it is evident that both sets of results are in close agreement, with a minimum percent difference of 0.009% and a maximum percent difference of 1.120%. In terms of thermal radiation, it was observed that an increase in the thermal radiation parameter does not significantly affect the boundary layer thickness under adverse, zero, or favorable pressure gradients, with no discernible changes in the velocity profiles or wall shear stress. This indicates that the thermal radiation parameter has a minimal or negligible impact on these quantities. However, when considering the energy equation, it was found that an increase in thermal radiation leads to a thickening of the thermal boundary layer across all pressure gradient conditions—adverse, zero, and favorable. Additionally, the wall shear stress was seen to decrease, trending towards zero with increasing thermal radiation.

Chapter 7
Stability of Incompressible/Compressible Laminar Boundary Layers

7.1 Background

As the speed of fluid flow increases, compressibility-related issues arise. A comprehensive understanding of high-speed flow behavior is essential for developing more effective control techniques to mitigate fluid flow drag and manage aerodynamic heating effects on vehicle designs. The Navier-Stokes (NS) equations, which govern fluid dynamics, are solved numerically as a boundary value problem. These equations can be solved by applying certain assumptions to derive solutions for specific cases. One such solution is the boundary layer equations, or Prandtl theory, for external flow (Cengel, Y. A. and Cimbala, J. M. 2014; Cengel, Y. A. and Ghajar, A. J. 2015; White, F. M. 1991). The Prandtl boundary layer theory divides the external flow into two distinct regions separated by a boundary layer (see Figure 1.2): i) a near-wall region, where viscosity effects are significant (the viscous region); and ii) a far-field region, where viscosity effects are negligible (the inviscid region). The flow state is determined by the critical Reynolds number. This number sets the limit where the flow changes from laminar to transitional and transitional to turbulent (see Figure 1.3).

Transitional flow represents a mixture of laminar and turbulent flow, making it inherently difficult to study and not fully understood. Transitional flow is typically analyzed through a stability analysis of the Navier-Stokes (NS) equations to assess their response to small disturbances and determine the stability of the system. As outlined in Section 3.1, stability analysis examines whether a physical system can return to its original state or position after being disturbed. There are four types of stability conditions (White, F. M. 1991): unconditionally stable, unstable, neutral stability, and partial stability (a

combination of stable and unstable states). When a disturbance is introduced into the NS equations, it evolves into a traveling wave.

A stability analysis involves the following steps: 1) add a disturbance to a selected basic flow solution; 2) isolate the disturbance governing equations; 3) linearize the equations by assuming small disturbances (higher-order terms can be neglected); 4) model disturbances as a traveling wave; 5) solve the eigenvalues. After simplifying the disturbance and applying Squire's theorem (for any two-dimensional parallel flow, the minimum critical unstable Reynolds number is obtained for the case of a two-dimensional disturbance propagating along the same direction (White, F. M. 1991)), the Orr-Sommerfeld incompressible flow equation is obtained (White, F. M. 1991). For compressible flows after Mach 0.7 Squire's theorem no longer holds for the first mode, and the second mode satisfies this theorem throughout. This behavior is due to the fact that the dissipation term in the energy equations cannot be transformed into a two-dimensional system. In this study, a thermal flow version of the OSE is used to account for the changes in density and viscosity properties due to temperature changes in the compressible flow. The equations are solved numerically via a finite difference scheme to obtain the neutrality curves. These curves can be used to predict the starting point of the transition by finding the critical Reynolds number located on the leftmost side of the stability-neutral curve. Finally, stability can predict the end of the laminar flow section (the onset of the Tollmien-Schlichting waves) but not the beginning of turbulence.

To perform the stability analysis, a velocity profile of the flow must first be obtained. In this section, the velocity profiles derived from the Blasius and Falkner-Skan equations will be used in the Orr-Sommerfeld equation for incompressible flow. For flows with variable properties, the velocity profiles from the Blasius compressible and Cohen-Reshotko equations will be used in the thermal Orr-Sommerfeld equation. The Blasius compressible and Cohen-Reshotko equations must be solved simultaneously with the energy equation and an equation of state to determine the values of density and viscosity. The viscosity can be modeled using the Power Law, while the density can be approximated using the ideal gas law. These similarity flow equations can be solved using an explicit finite difference scheme. The incompressible flow equation 3.30 is solved, and in the case of the compressible flow equation 3.62 is solved for a variable property flow. Both Orr-Sommerfeld equations are solved via a finite difference scheme. For more details, see Sections: 3.3 and 3.7

In this chapter, the momentum boundary layer thickness is obtained at the coordinate η where f' is 0.999 to keep consistency with Wazzan *et al.* (Wazzan, A. R., Okamura, T. T. and Smith, A. M. O. 1968) and Simpson (Simpson, C. 2015a; Simpson, C. 2015b)

7.2 Incompressible Flow Stability Studies

Figure 7.1 shows a comparison of the present neutral stability curve result with the one obtained by Simpson (Simpson, C. 2015a; Simpson, C. 2015b) based on the momentum boundary layer thickness coordinate, by forcing a momentum boundary layer thickness of 4.2411, and Figure 7.2 shows a comparison of the present result compared to Wazzan *et al.* (Wazzan, A. R., Okamura, T. T. and Smith, A. M. O. 1968) using the displacement thickness coordinate. Its important to mention that the Blasius incompressible flat plate velocity profile was used to perform these studies. The results in Figure 7.1 show that both curves coincide with each other, which means that there is a very good agreement with the present solution and Simpson (Simpson, C. 2015a; Simpson, C. 2015b). However, in Figure 7.2 it can be observed that the present curve is very near Wazzan *et al.* (Wazzan, A. R., Okamura, T. T. and Smith, A. M. O. 1968) data at the section where the critical Reynolds is located but is not near the edges; this is due to the fact that a forward and backward Euler of order one was applied at the first and last nodes of the stability problem to find the values of the second node and the node N-1 (N is the total number of nodes), in order to apply the finite difference method. It can be said that the disadvantage of this method is the precision at the corners of the stability problem, but this method still gives a critical Reynolds number very close to that obtained by Wazzan *et al.* (Wazzan, A. R., Okamura, T. T. and Smith, A. M. O. 1968).

Figures 7.3 and 7.4 show the neutral stability curves and a comparison of the critical Reynolds number with a trendline whose equation is given in Table 7.1 for different pressure gradients based on the momentum boundary layer thickness coordinate; and Figures 7.5 and 7.6 show the stability curves and a comparison of the critical Reynolds number for the present, trendline (Table 7.1) and Wazzan *et. al.* (Wazzan, A. R., Okamura, T. T. and Smith, A. M. O. 1968) data for different pressure gradients based on the displacement thickness coordinate. It is important to mention that the Falkner Skan incompressible velocity profiles were used to perform these studies. It can be observed in Figures 7.3 and 7.5 that as the pressure gradient becomes more adverse, the unstable area enclosed by the curve increases and as the pressure gradient becomes more favorable, the unstable area decreases. Then Figures 7.4 and 7.6 show that as the pressure gradient becomes more favorable, the critical Reynolds number increases. In terms of the curve trendline, Figure 7.4 shows that there is a very good agreement between the present and the approximate solution, and Figure 7.6 shows that there is also a very good agreement with the present and Wazzan *et al.* (Wazzan, A. R., Okamura, T. T. and Smith, A. M. O. 1968) data. It can be said that the equations of these trendlines (Table 7.1) could be used to give a rough estimate of the critical Reynolds number based on the

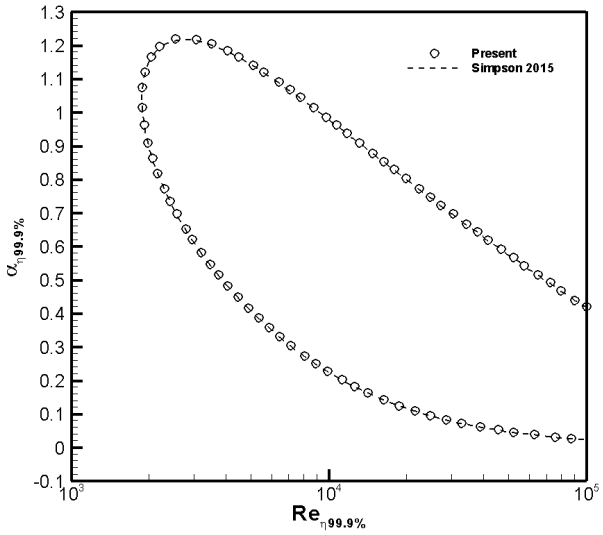

Figure 7.1: Blaisus incompressible flow stability verification using the momentum boundary layer thickness coordinate

Table 7.1: Trendline equation: $Re_{cr} = A(e^{B\beta})$

Coordinates	A	B
$\eta_{99.9\%}$	1770.7	10.961
η^*	523.58	9.7676

pressure gradient value, based on the coordinates of the momentum boundary layer and displacement thicknesses. Finally, it is important to mention that increasing the pressure gradient in a favorable pressure direction is an effective way to increase flow stability and the critical Reynolds number which increases the laminar flow section.

7.3 Blasius Compressible Flow Stability Studies

Figures 7.7 and 7.8 show the neutral stability curves and the critical Reynolds number distribution for different Mach numbers based on the momentum boundary layer coordinate. It can be observed in Figure 7.7 that as the Mach number increases, the stability curves move to the right. Also, Figure 7.8 shows that as the Mach number increases, the critical Reynolds number increases. This means that increasing the Mach number

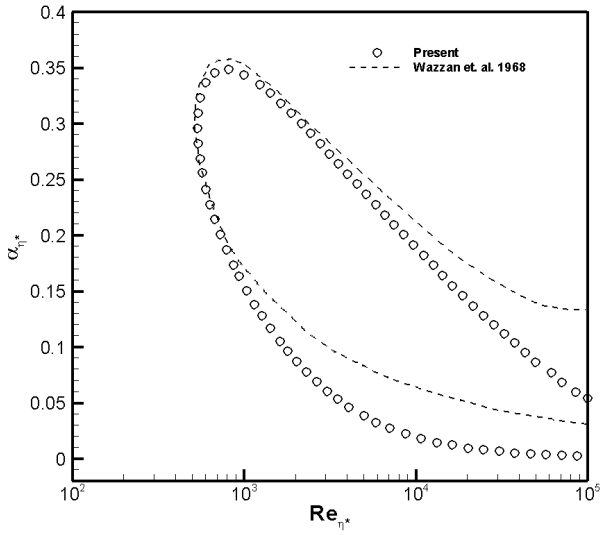

Figure 7.2: Blaisus incompressible flow stability verification using the displacement thickness coordinate

Table 7.2: Trendline equation: $Re = A(Mach^5) + B(Mach^4) + C(Mach^3) + D(Mach^2) + E(Mach) + F$

Parameters	Values
A	0.0243
B	-0.4081
C	-5.5698
D	303.09
E	341.94
F	1508.6

moves the stability curves to the right, increasing the critical Reynolds number, which in the end increases the position where the fluid changes from laminar to transitional flow. In terms of the trendline whose equation is given in Table 7.2, it can be observed that the present result is in good agreement with this approximation. So, this trendline approximation can be used as a rough estimate for the critical Reynolds number based on the Mach number.

Figures 7.9 and 7.10 show the neutral stability curves and the critical Reynolds number distribution for different Prandtl numbers based on the momentum boundary layer

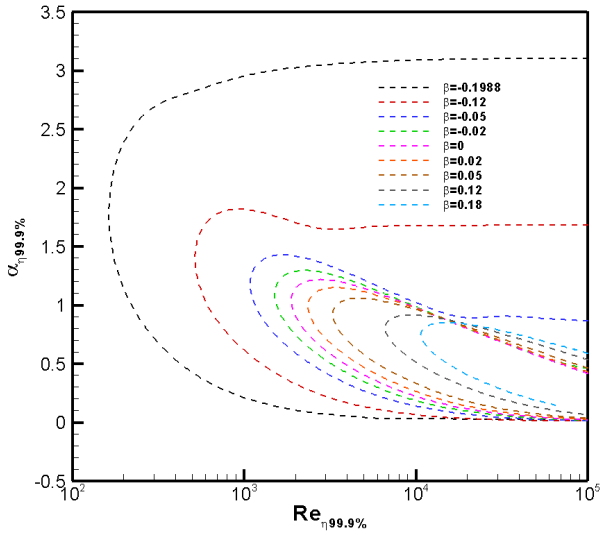

Figure 7.3: Falkner-Skan incompressible flow stability for different pressure gradients using the momentum boundary layer thickness coordinate

Table 7.3: Trendline equation: $Re = A(Pr^3) + B(Pr^2) + C(Pr) + D$

Parameters	**Values**
A	323.76
B	-1729.6
C	10192
D	3392.5

coordinate for Mach number 5. It can be observed in Figure 7.9 that as the Prandtl number increases, the stability increases. Also, Figure 7.10 shows that as the Prandtl number increases, the critical Reynolds number increases. This means that increasing the Prandtl number increases flow stability, increasing the critical Reynolds number, increases the position where the fluid changes from laminar to transitional flow. In terms of the trendline whose equation is given in Table 7.3, it can be observed that the present result is in good agreement with this approximation. So, this trendline approximation can be used as a rough estimate for the critical Reynolds based on the Prandtl number for Mach 5.

Figures 7.11 and 7.12 show the neutral stability curves and the critical Reynolds number distribution for different Power Law n based on the momentum boundary layer thickness

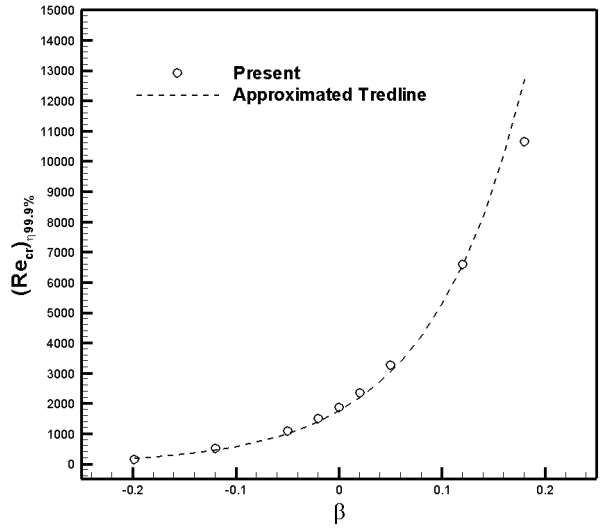

Figure 7.4: Falkner-Skan incompressible flow $(Re_{cr})_{\eta_{99.9\%}}$ vs β comparison with trendline using the momentum boundary layer thickness coordinate

Table 7.4: Trendline equation: $Re = A(n^2) + B(n) + C$

Parameters	**Values**
A	-703.2
B	-2692.3
C	12382

coordinate for a Mach number of 5. It can be observed in Figure 7.11 that as the Power Law n increases the stability decreases. Also, Figure 7.12 shows that as the Power law n increases, the critical Reynolds number decreases. This means that decreasing the Power Law n increases the flow stability, increasing the critical Reynolds number, which in the end, as stated before, increases the position where the flow changes from laminar to transitional flow. In terms of the trendline whose equation is given in Table 7.4, it can be observed that the present result is in good agreement with this approximation. So, this trendline approximation can be used as a rough estimate for the critical Reynolds based on the Power Law n number for Mach 5.

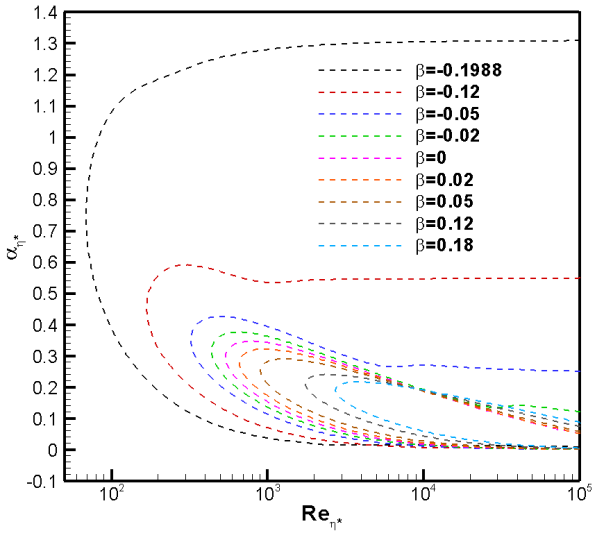

Figure 7.5: Falkner-Skan incompressible flow stability for different pressure gradients using the displacement thickness coordinate

7.4 Cohen-Reshotko Flow Stability Studies

Figures 7.13 and 7.14 show the neutral stability curves and the distribution of the critical Reynolds number for several pressure gradients based on the momentum boundary layer thickness coordinate for a wall temperature of 2. It can be seen in Figure 7.13, that, similarly to the incompressible flow stability, as the pressure gradient becomes more adverse, the unstable area enclosed by the curve increases, and as the pressure gradient becomes more favorable, the unstable area decreases. Also, Figure 7.14 shows that as the pressure gradient increases from negative (APG) to positive (FPG), the critical Reynolds number increases. This means that increasing the pressure gradient increases the flow stability and the position where the fluid changes from laminar to transitional flow. Finally, Table 7.5 show the trendline equation of Figure 7.14. It can be observed in Figure 7.14 that the trendline is almost coincident with the present values. So, this trendline could be used to give a rough estimate of the critical Reynolds number based on the pressure gradient value.

Figures 7.15 and 7.16 show the neutral stability curves and the distribution of the critical Reynolds number as the wall temperature changes based on the momentum boundary layer thickness coordinate for a pressure gradient of -0.1305. It can be observed in Figure

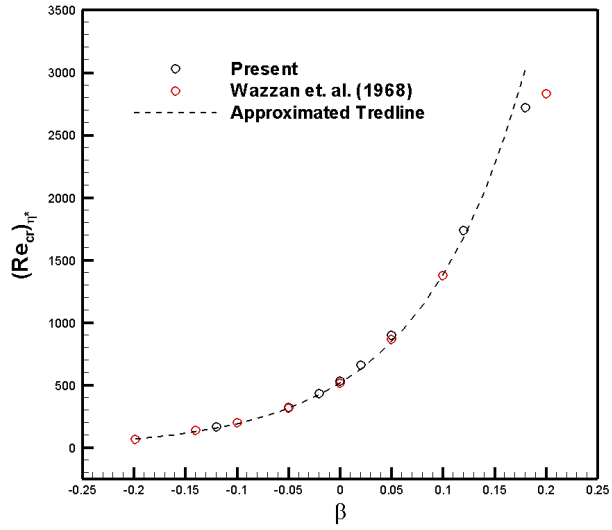

Figure 7.6: Falkner-Skan incompressible flow $(Re_{cr})_{\eta^*}$ vs β comparison with trend-line and Wazzan *et. al.* (Wazzan, A. R., Okamura, T. T. and Smith, A. M. O. 1968) data using the displacement thickness coordinate

Table 7.5: Trendline equation: $Re = A(e^{B\beta})$

Parameters	**Values**
A	3165.1
B	18.763

7.15 that as the wall temperature decreases from hot to cold, the flow stability increases due to the fact that lowering the wall temperature decreases the flow viscosity. Next, Figure 7.16 shows that as the wall temperature decreases, the critical Reynolds number increases until it reaches an inflection point and decreases again. This inflection for the momentum boundary layer thickness coordinate has a wall temperature around 0.4 at a pressure gradient of -0.1305. This means that lowering the temperature is an effective way of increasing flow stability, but in terms of the critical Reynolds number, decreasing the wall temperature will increase the laminar flow section to a certain maximum critical Reynolds number (inflection point), then beyond that point the critical Reynolds lowers and the laminar flow section decreases again. This behavior is due to the fact that the stability curves become more flat as the wall temperature lowers. Finally, Table 7.6 shows the trendline equation used in Figure 7.16. It can be seen that the trend line is in very good agreement with the present values. So, it can be used as a rough estimate to

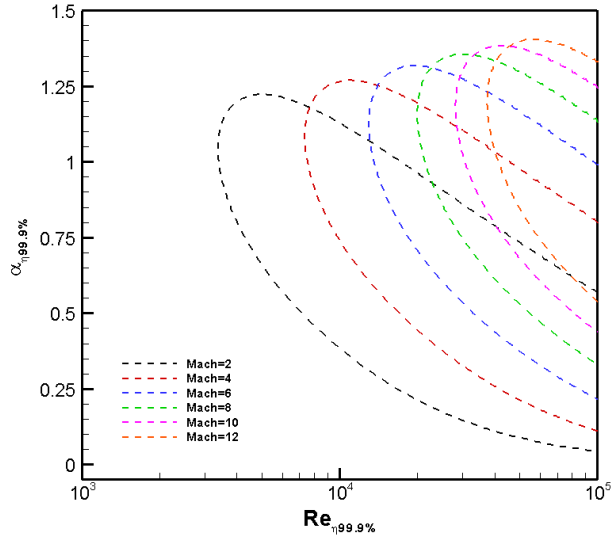

Figure 7.7: Blasius stability for compressible flow at different Mach numbers based on the momentum boundary layer thickness coordinate

Table 7.6: Trendline equation: $(Re_{cr})_{\eta_{99.9\%}} = A(g_w^5)+B(g_w^4)+C(g_w^3)+D(g_w^2)+E(g_w)+F$

Parameters	**Values**
A	-15.104
B	2.7833
C	188.37
D	-478.31
E	325.3
F	440.29

obtain the critical Reynolds number at a pressure gradient of -0.1305 based on the wall temperature (g_w).

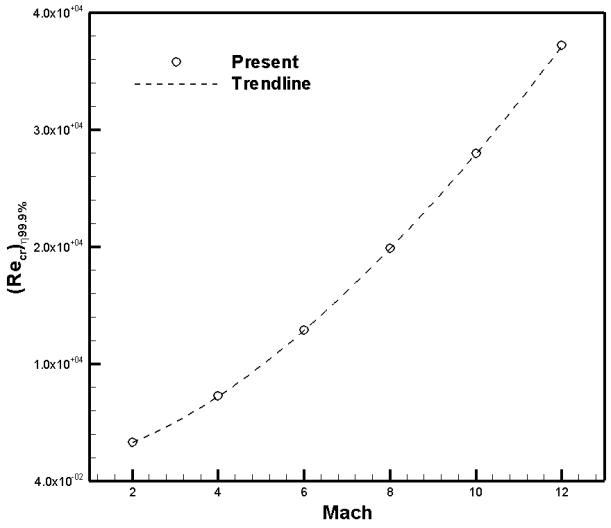

Figure 7.8: Blasius stability compressible flow $(Re_{cr})_{\eta_{99.9\%}}$ vs Mach comparison with trendline based on the momentum boundary layer thickness coordinate

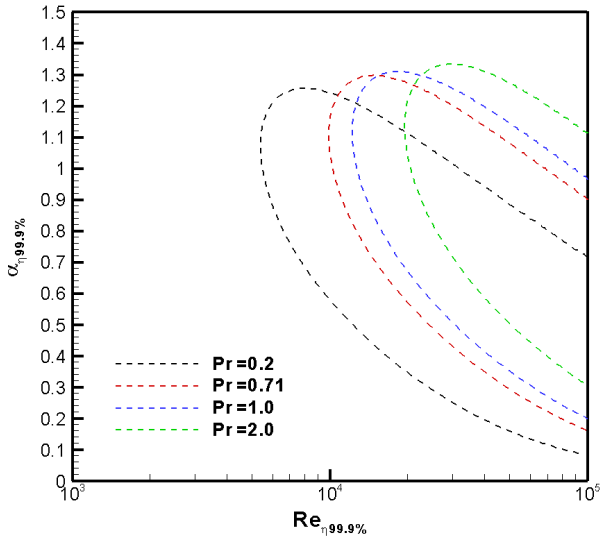

Figure 7.9: Blaisus stability for compressible flow for different Prandlt numbers at Mach 5 based on the momentum boundary layer thickness coordinate

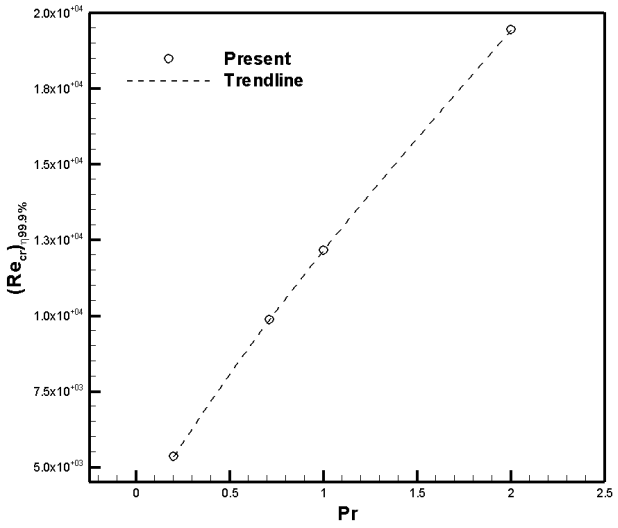

Figure 7.10: Blaisus Stability compressible flow $(Re_{cr})_{\eta_{99.9\%}}$ vs Prandlt number at Mach 5 present result comparison with trendline approximation based on the momentum boundary layer thickness coordinate

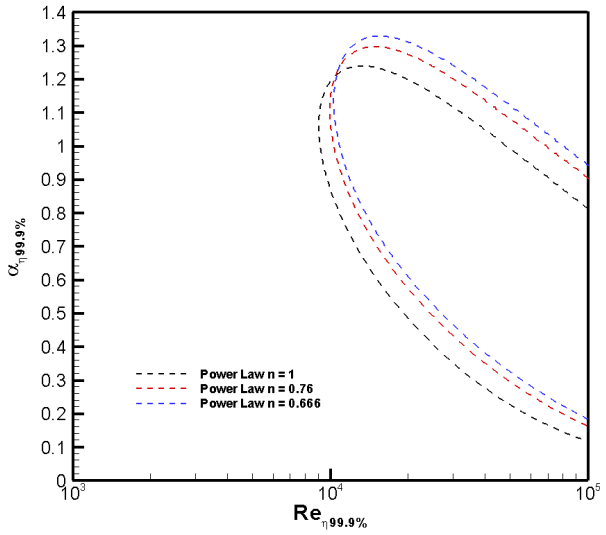

Figure 7.11: Blasius stability for compressible flow for different Power Law n at Mach 5 using the momentum boundary layer thickness coordinate

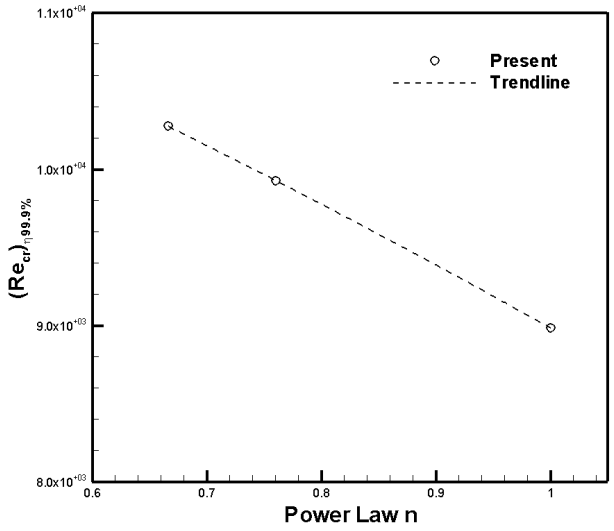

Figure 7.12: Blasius Stability compressible flow $(Re_{cr})_{\eta_{99.9\%}}$ vs Power Law n at Mach 5 present result comparison with trendline approximation based on the momentum boundary layer thickness coordinate

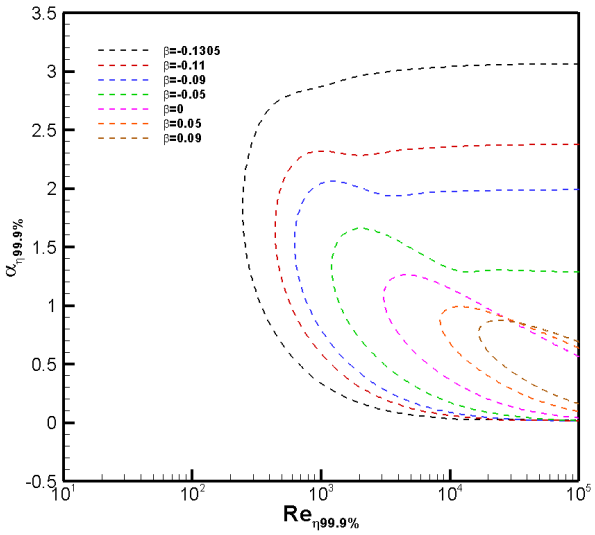

Figure 7.13: Cohen-Reshotko flow stability for different pressure gradients using the momentum boundary layer thickness coordinate

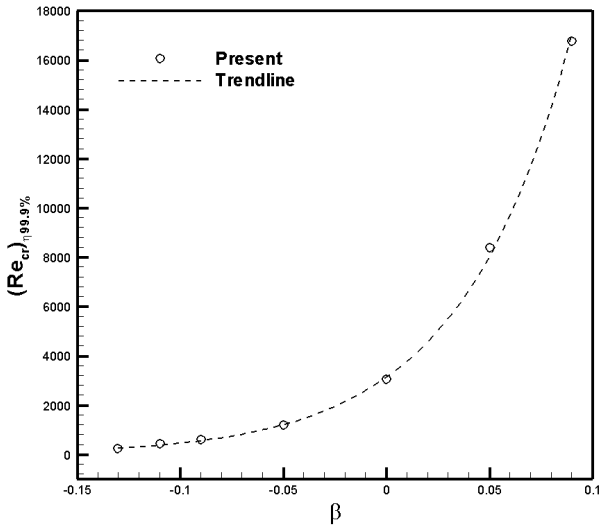

Figure 7.14: Cohen-Reshotko flow $(Re_{cr})_{\eta_{99.9\%}}$ vs β comparison with trendline using the momentum boundary layer thickness coordinate

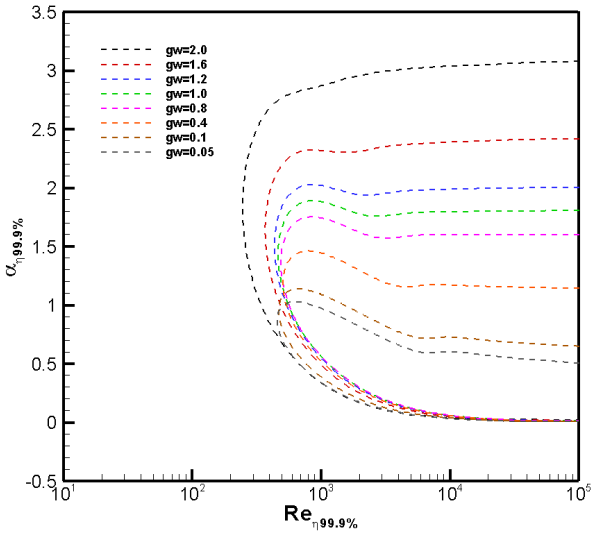

Figure 7.15: Cohen-Reshotko flow stability for different wall temperatures using the momentum boundary layer thickness coordinate

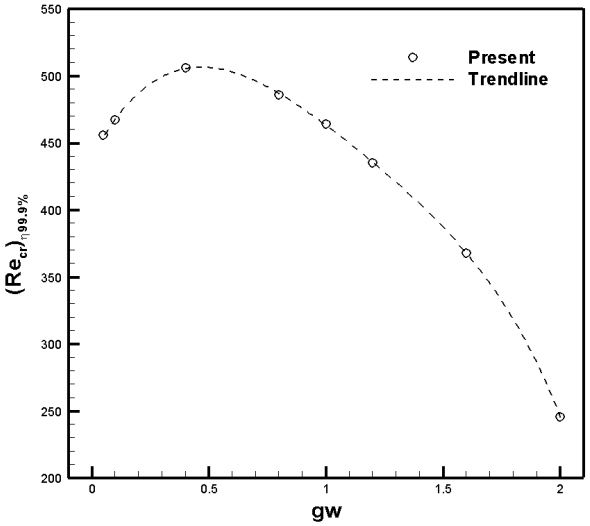

Figure 7.16: Cohen-Reshotko flow stability $(Re_{cr})_{\eta_{99.9\%}}$ vs wall temperature comparison with trendline using the momentum boundary layer thickness coordinate

7.5 Chapter 7 Conclusions

In conclusion, the Orr-Somerfeld equation for incompressible and compressible flow was solved by a finite difference scheme. The Orr-Somerfeld is a fourth-order differential equation that is solved as an eigenvalue problem. In this work, the equation was solved by using the 'eig()' function in Matlab.

It was observed that for the stability of incompressible flows the neutral curves have a good match with Simpson (Simpson, C. 2015a; Simpson, C. 2015b) solution based on the momentum boundary layer thickness coordinate and are very close to the data of Wazzan *et al.* (Wazzan, A. R., Okamura, T. T. and Smith, A. M. O. 1968) based on the displacement thickness coordinate. The discrepancies observed in Figure 7.2 can be attributed to the error in the corners in the finite difference solution assumptions. However, it was observed that for both cases (for the momentum boundary layer and displacement thickness coordinates) the critical Reynolds number is very close to the Simpson solution (Simpson, C. 2015a; Simpson, C. 2015b) and the data of Wazzan *et al.* (Wazzan, A. R., Okamura, T. T. and Smith, A. M. O. 1968). In addition, it was observed that as the pressure gradient increases from negative (adverse pressure gradient) to positive (favorable pressure gradient), the stability increases and the critical Reynolds number increases, increasing the laminar flow section.

It was observed that for the Blasius compressible flow solution, increasing the Mach and Prandtl numbers moves the stability curves to the right increasing the critical Reynolds and the laminar flow section. Also, it was observed that as the Power Law n increases, the critical Reynolds number and the laminar flow section decrease.

Finally, in the case of Cohen-Reshotko compressible flow, it was observed that as the pressure gradient increases, both the flow stability and the critical Reynolds number exhibit an increase. Furthermore, under an adverse pressure gradient, a decrease in wall temperature was found to enhance the stability of the flow. However, the critical Reynolds number initially increases with decreasing wall temperature, reaching a peak at a certain value, before subsequently decreasing. Therefore, while reducing the wall temperature proves to be an effective means of enhancing flow stability (up to $gw = 0.4$), it results in an increase in the laminar flow region up to a maximum critical Reynolds number, beyond which the critical Reynolds number decreases.

Chapter 8
Conclusions and Future Work

8.1 Final Remarks

The current research aimed to: 1) solve the Blasius and Falkner Skan incompressible flow equations; and the Blasius and Cohen-Reshotcko compressible flow equations using an explicit finite difference scheme to avoid the shooting method used in the Runge-Kutta solvers; 2) study the compressibility effects on the flow dynamics; and 3) study the compressibility effect on transition by performing a stability analysis using a finite difference scheme. The numerical simulations were performed using an in-house MATLAB code.

This study demonstrated that for the Falkner-Skan incompressible flow solution, reducing the pressure gradient, which results in an adverse pressure gradient scenario, ultimately leads to flow separation. In such cases, the wall shear stress becomes zero, and the boundary layer equations break down. It is crucial to note that when flow separation occurs, the full Navier-Stokes equations must be employed to accurately describe the flow. A practical approach to mitigate flow separation is to increase the pressure gradient (related to the wedge angle), as this induces a favorable pressure gradient that accelerates the flow, driving it closer to the wall and effectively reducing the boundary layer thickness. However, while this approach prevents flow separation, it comes at the cost of increasing the wall shear stress. One distinctive feature of incompressible flow is that it can be decoupled from the energy equation, allowing the buoyancy effects due to temperature variations to be neglected. In terms of the energy equation, it was observed that a decrease in the pressure gradient leads to an increase in the thermal boundary layer thickness. According to White (White, F. M. 1991), the energy similarity equation holds for both Blasius and Falkner-Skan similarity solutions, provided that the viscous dissipation term is neglected and the wall and stream temperatures remain constant. With this in mind, it was found that decreasing the pressure gradient while maintaining the wall temperature at unity results in a heat loss at the wall, which gradually approaches zero as the pressure gradient becomes more adverse.

An additional important solution is the curvature boundary layer, which yields a fourth-order similarity solution. According to Murphy (Murphy, J. S. 1965), this fourth-order solution represents a more general similarity solution for the flow, as it accounts for the surface geometry or curvature, which induces a non-negligible normal pressure gradient at the wall due to centrifugal forces. It is noteworthy that, for flat plate or wedge flows, the dimensionless velocity, $f^{'}$, equals one in the free-stream. However, in the presence of a curved surface, the free-stream velocity corresponds to that of a potential flow solution. In such a configuration, with respect to the pressure gradient, the flow behaves similarly to a flat plate or wedge flow. In contrast, the introduction of surface curvature leads to changes in the boundary layer characteristics: a decrease in curvature (e.g., a concave geometry) reduces the momentum boundary layer thickness while increasing the wall shear stress. Conversely, a convex curvature can eventually induce flow separation. As with flat plate or wedge flows, the energy equation in the curvature-boundary layer scenario is decoupled from the momentum equations, making the energy a passive scalar. This implies that the energy equation is unaffected directly by the flow, but the flow itself influences the temperature distribution. When the curvature parameter is zero, the flow behaves similarly to Blasius or Falkner-Skan flow. However, the influence of curvature on the temperature distribution is more pronounced than its effect on the pressure gradient. Specifically, it was observed that as the curvature decreases, the thermal boundary layer thickness diminishes. Additionally, an increase in the Prandtl number results in a reduction in thermal boundary layer thickness, accompanied by an increase in the normalized wall heat flux.

Several rough approximations were developed to estimate the wall shear stress based on Murphy's (Murphy, J. S. 1965) data based on the surface curvature for a pressure gradient of 1, 0.2, 0 and -0.1:

$$f^{''}(0) = -1.6426\Omega + 1.2302 \tag{8.1}$$

$$f^{''}(0) = -1.3003\Omega + 0.6861 \tag{8.2}$$

$$f^{''}(0) = -1.0189\Omega + 0.4693 \tag{8.3}$$

$$f''(0) = -0.7359\Omega + 0.319 \tag{8.4}$$

These equations can be used as a starting point in the point and shoot method alongside Figure 4.6. As stated before the $f''(0)$ is associated with the wall shear stress and Ω with the wall curvature.

In engineering practice, many flows are analyzed under the steady-state assumption; however, there are instances, such as start-up processes, where the fluid flow is inherently unsteady. During start-up processes, the flow begins from a zero velocity state, and as time progresses, a momentum boundary layer gradually develops until the system reaches its steady-state condition. The primary distinction in unsteady cases is that time-dependent effects must be incorporated into similarity solutions. Harris *et al.* (Harris, S. D., Ingham, D. B. and Pop, I. 2008; Harris, S. D., Ingham, D. B. and Pop, I. 2002) developed a solution for an unsteady Falkner-Skan flow assuming a constant wall temperature and heat flux case. In this research equations 5.32, 5.33, 5.34 and 5.35 were solved using an explicit finite difference scheme and the results were compared with Harris *et al.* (Harris, S. D., Ingham, D. B. and Pop, I. 2008; Harris, S. D., Ingham, D. B. and Pop, I. 2002) analytical solutions for a dimensionless time τ of one for 3200 nodes. As time progresses, the boundary layer gradually forms, causing an increase in the momentum boundary layer at the wall, while the wall shear stress decreases. Since the flow remains incompressible, the energy equation is decoupled from the momentum equations, and buoyancy effects are neglected. When the wall temperature was held constant, it was observed that, over time, the thermal boundary layer thickened, while the heat flux at the wall diminished, eventually stabilizing once the flow reached its steady-state condition. Under constant wall temperature conditions, an increase in the Prandtl number was found to decrease the thermal boundary layer thickness. For the constant heat flux case, as time progressed, the wall temperature increased, and the slope of the heat flux curve diminished until steady-state was achieved. With respect to the pressure gradient, under constant temperature conditions, an increase in the pressure gradient led to a reduction in the thermal boundary layer thickness and an increase in heat loss at the wall. In the constant heat flux scenario, increasing the pressure gradient slightly reduced the thermal boundary layer thickness and enhanced the heat flux at the wall. Finally, it is important to emphasize that, for the unsteady case, the pressure gradient has a more pronounced impact on the momentum equations than on the energy equations.

In compressible flow, the energy equation is coupled with the momentum equation, necessitating the simultaneous solution of both equations to capture the effects of energy within

the boundary layer. The compressible flow Blasius solution was successfully validated using a grid of 1000 nodes for the case where the linear viscosity-density to viscosity-density edge ratio is constant, i.e., $C = 1$. For compressible flow with a variable $C \neq 1$, an increase in the Mach number results in an increase in wall shear stress, a reduction in the momentum boundary layer thickness, an expansion of the thermal boundary layer, and an increase in the minimum heat flux. Furthermore, in this case, increasing the Power Law exponent n leads to a reduction in the shear stress at the wall, with a value of $n = 0.76$ being chosen as optimal. Another relevant compressible flow solution is the Cohen-Reshotko flow, which was validated for a non-dimensional temperature of 2 and a pressure gradient of 2 using a grid of 1000 nodes. Similar to incompressible flow, increasing the pressure gradient results in a decrease in the momentum boundary layer thickness and an increase in the shear stress at the wall. In the specific case of a wall temperature of 2 and a pressure gradient of 2, a velocity overshoot phenomenon was observed. For favorable pressure gradients, an increase in the wall temperature leads to an increase in shear stress at the wall, whereas for adverse pressure gradients, the same increase in wall temperature results in a decrease in wall shear stress. Given the coupling between the energy and momentum equations, changes in wall temperature influence the momentum boundary layer thickness. Specifically, in the presence of adverse pressure gradients, a decrease in wall temperature leads to a reduction in the momentum boundary layer thickness, while in the case of favorable pressure gradients, the opposite effect is observed. It can be concluded that for the Cohen-Reshotko flow, reducing the wall temperature is an effective strategy for delaying flow separation. Additionally, for a hot wall, increasing the wall temperature increases the thermal boundary layer thickness, whereas for a cold wall, increasing the wall temperature decreases the thermal boundary layer thickness. The compressible flow similarity equations for normalized temperature were solved using an explicit finite difference scheme. The thermal-to-momentum boundary layer thickness ratio was computed and validated against data from Back (Back, L. H. 1970), with a minimum percent difference of 0.009% and a maximum percent difference of 1.120%. Finally, it was observed that increasing the pressure gradient and the wall temperature both lead to an increase in the thermal-to-momentum boundary layer thickness ratio, whereas an increase in the speed parameter S results in a reduction of this ratio. Moreover, while the thermal radiation parameter has negligible or no impact on the momentum equations, in the energy equations, an increase in the thermal radiation parameter causes the thermal boundary layer thickness to expand and the heat flux at the wall to decrease.

Flow stability is analyzed by performing a stability analysis on the Navier-Stokes equations. In the present study, both the Orr-Sommerfeld and thermal Orr-Sommerfeld equations were solved using a finite difference scheme, with eigenvalues computed via

the MATLAB eig() function. The incompressible Orr-Sommerfeld equations were validated against Simpson's solution (Simpson, C. 2015a; Simpson, C. 2015b), based on the momentum boundary layer thickness coordinate, and also with data from Wazzan *et al.*(Wazzan, A. R., Okamura, T. T. and Smith, A. M. O. 1968), using the displacement thickness coordinates. Minor discrepancies were observed with the Wazzan *et al.*(Wazzan, A. R., Okamura, T. T. and Smith, A. M. O. 1968) data, likely due to errors introduced at the corners of the domain, which stem from the assumptions in the Forward and Backward Euler solution method applied at the second node and the last node, $N-1$. Nonetheless, in terms of the critical Reynolds number, the present finite difference solution closely matched the results of Wazzan *et al.* (Wazzan, A. R., Okamura, T. T. and Smith, A. M. O. 1968). For incompressible flows, a notable method to enhance flow stability is to increase the pressure gradient. This has the effect of elevating the critical Reynolds number, thereby extending the laminar flow regime or delaying transition to turbulence. In the case of compressible Blasius flow, increasing the Prandtl number and Mach number, while simultaneously decreasing the Power Law exponent n, results in an increase in the critical Reynolds number, which, as previously noted, delays transition. For Cohen-Reshotko flow, increasing the pressure gradient similarly enhances stability by increasing the critical Reynolds number, which in turn delays transition. In adverse pressure gradient conditions, a decrease in wall temperature increases flow stability, causing an initial rise in the critical Reynolds number until it reaches a maximum value, after which it begins to decrease. Despite this, lowering the wall temperature remains an effective strategy for stabilizing the flow and delaying transition to turbulence.

In this work a rough approximation was developed to find the critical Reynolds for incompressible flow as the pressure gradient (β) changes.

Critical Reynolds (Re_{cr}) based on the momentum boundary layer thickness ($\eta_{99.9\%}$:

$$Re_{cr} = 1770.7e^{10.961\beta} \tag{8.5}$$

Critical Reynolds based on the displacement boundary layer thickness:

$$Re_{cr} = 523.58e^{9.7676\beta} \tag{8.6}$$

A rough critical Reynolds number estimate for a Blasius compressible flow was also developed based on the Mach number (M), Prandtl number (Pr), and Power Law n (n) based on the momentum boundary layer thickness ($\eta_{99.9\%}$):

$$Re_{cr} = 0.0243M^5 - 0.4081M^4 + -5.5698M^3 + 303.09M^2 + 341.94M + 1508.6 \quad (8.7)$$

$$Re_{cr} = 323.76Pr^3 - 1729.6Pr^2 + 10192Pr + 3392.5 \quad (8.8)$$

$$Re_{cr} = -703.2n^2 - 2692.3n + 12382 \quad (8.9)$$

Finally, a rough estimate of the critical Reynolds (Re_{cr}) number for the Cohen and Reshotko compressible flow was developed based on the pressure gradient (β) and the wall temperature (g_w):

$$Re_{cr} = 3165.1e^{18.763\beta} \quad (8.10)$$

$$Re_{cr} = -15.104g_w^5 + 2.7833g_w^4 + 188.37g_w^3 - 478.31g_w^2 + 325.3g_w + 440.29 \quad (8.11)$$

These approximations can be used to estimate the critical Reynolds number. The critical Reynolds number can be used to obtain the length of the laminar flow section.

In summary, the key findings of this study are as follows:

• The Blasius and Falkner-Skan incompressible flow equations, along with the Blasius and Cohen-Reshotko compressible flow equations, were successfully solved using a finite difference algorithm, with the solutions subsequently validated against established benchmarks.

• An increase in the pressure gradient for incompressible flow results in a corresponding rise in wall shear stress and heat flux, while simultaneously reducing the thicknesses of both the momentum and thermal boundary layers.

• With regard to curvature effects, an increase in surface curvature (convex curvature) leads to an increase in both momentum and thermal boundary layer thicknesses, while concurrently causing a reduction in wall shear stress and heat flux.

• In unsteady flow, as the dimensionless time τ progresses, the momentum boundary layer thickness increases while the shear stress at the wall decreases. Under constant wall temperature conditions, the heat flux at the wall diminishes, whereas under constant heat flux conditions, the wall temperature increases.

• In terms of compressible flow, as the Mach number increases, the shear stress at the wall increases, the minimum heat flux increases, the momentum boundary layer thickness decreases and the thermal boundary layer thickness increases.

• A key conclusion for high-speed flow is that reducing the wall temperature can effectively delay the onset of flow separation.

• In terms of flow stability for incompressible flows, an increase in the pressure gradient enhances flow stability and delays the transition to turbulence.

• In compressible flow stability, an increase in the Mach number and pressure gradient contributes to enhanced flow stability and delays transition to turbulence. In the case of adverse pressure gradient (APG) flow, reducing the wall temperature increases flow stability, causing the critical Reynolds number to rise to a maximum value before eventually decreasing. Nevertheless, lowering the wall temperature remains an effective method for delaying transition in APG flows.

This thesis makes several key contributions to the field, including: 1) the development of an explicit finite difference solver for both incompressible and compressible similarity flows, providing a foundational step towards more efficient algorithms for solving these numerical problems without reliance on shooting methods; 2) a comprehensive analysis of the impact of external conditions on flow dynamics and stability, with potential implications for optimized vehicle design; 3) a stability analysis of an adverse pressure gradient (APG) flow at varying wall temperatures (Cohen-Reshotko flow), offering insights into strategies for extending the laminar flow regime and delaying transition to turbulence; and 4) the derivation of trendline approximations to streamline the critical Reynolds number study for a variety of flow conditions, enabling faster and more efficient calculations.

8.2 Future Work

An investigation into the effects of surface curvature on flow stability under various pressure gradient conditions could provide valuable insights. Specifically, it would be

of interest to explore whether modifying the curvature—either increasing or decreasing it—can be used as a strategy to stabilize the flow and extend the laminar flow regime. To conduct these studies, it would be necessary to develop an Orr-Sommerfeld boundary layer solution that incorporates the effects of surface curvature.

An explicit finite difference scheme was employed to conduct the numerical analysis of the similarity equations, including the Blasius, Falkner-Skan, Cohen-Reshotko, and other related boundary layer equations. These solvers exhibit significant potential for computational optimization. Future developments could focus on enhancing the efficiency of the code, particularly through the integration of parallel processing techniques such as OpenMP or Open Multiprocessing. OpenMP, which utilizes processor threads (the fundamental units of computational work), can be leveraged to parallelize the solution process, thereby expediting calculations, especially when dealing with a large number of nodes. Furthermore, the stability analysis, which relies on the finite difference method (FDM), is also amenable to optimization. This could be achieved by refining the MATLAB left division operation or implementing transformations within the eigenvalue matrix to accelerate the solver's performance. Consequently, future research could include a comprehensive computational cost analysis, comparing the performance improvements of the optimized parallelized code against the sequential implementation. Such an analysis would provide insights into the efficiency gains achievable through these optimizations, especially for large-scale simulations.

Appendix A
Falkner-Skan and Blasius Algorithms

A.0.1 Blasius Incompressible Flow Simulation Code

The Blasius similarity solution is solved using a Finite Difference Explicit algorithm without the need of a shooting method to guess the value of f'' or the shear stress at the wall.

The algorithm is as follows:

Inputs:L,N

Form η vector of Length L. Spacing:$\Delta\eta = \eta_2 - \eta_1$.

Initialization and Boundary Conditions: $f' = ErrorFunction(\eta)$; $f_1 = 0$;

Main Loop Start: for(iteration=1 to $1 * 10^{10}$)

Update: $f'^{next} = f'$

f Loop start: for (i=1 to $N - 1$)

$f_{i+1} = f_i + \Delta\eta \frac{(f'^{next}_{i+1} + f'^{next}_{i})}{2}$

f Loop end

Explicit Solution Start:

f' Loop Start: for(i=2 to $N - 1$)

$f'_i = \frac{(2+\Delta\eta f_i) f'^{next}_{i+1} + (2-\Delta\eta f_i) f'^{next}_{i-1}}{4}$

f' Loop End

Explicit Solution Ends

$Error = 0$

Error Loop Start: for(i=1 to N)

Error=Error + $abs(f_i'^{next} - f_i')$

Error Loop End

Convergence Condition: if Error is less or equal to $1 * 10^{-6}$ break loop.

Main Loop End

A.0.2 Falkner Skan Incompressible Flow Simulation Code

The Falkner-Skan incompressible flow equation is solved by a Finite Difference Explicit algorithm, without the need of a shooting method.

The algorithm is as follows:

Inputs: L, N, β

Form η vector of Length L. Spacing: $\Delta\eta = \eta_2 - \eta_1$

Initialization and Boundary Conditions: $f' = ErrorFunction(\eta)$; $f_1 = 0$

Main Loop Start: for (Iteration=1 to $1 * 10^{10}$)

Update: $f'^{next} = f'$

f Loop Start: for(i=1 to $N - 1$)

$f_{i+1} = f_i + \Delta\eta \frac{(f_{i+1}'^{next} + f_i'^{next})}{2}$

f Loop End

Interior Loop Start: for(iteration=1 to $1 * 10^{10}$)

Update: $f'^{n} = f'$

Explicit Solution Start:

f' Loop Start: for(i=2 to $N-1$)

$f_i' = \frac{(2+\Delta\eta f_i)f_{i+1}'^{n}+(2-\Delta\eta f_i)f_{i-1}'^{n}+2\Delta\eta^2\beta}{4+2\Delta\eta^2\beta f_i'^{n}}$

Explicit Solution Ends

$error = 0$

error Loop Start: for(i=1 to N)

$error = error + abs(f_i'^{n} - f_i')$

error loop end

Internal Loop convergence condition: if error is less or equal to $1 * 10^{-6}$ break loop

Interior Loop Ends

$Error = 0$

Error Loop Start: for(i=1 to N)

$Error = Error + abs(f_i'^{next} - f_i')$

Error Loop End

Internal Loop convergence condition: if Error is less or equal to $1 * 10^{-6}$ break loop

Main Loop Ends

A.0.3 Energy Laminar Incompressible Flow Simulation Code

The Energy equation similarity solution is solved using a Finite Difference Explicit algorithm without the need of a shooting method to guess the value of g' or the heat flux at the wall. The algorithm is as follows:

Inputs: L, N Pr, f, η, $\Delta\eta$

Initialization: $g = InverseErrorFunction(\eta)$;

Main Loop Start: for(iteration=1 to $1 * 10^{10}$)

Update: $g^{next} = g$

Explicit Solution Start:

g Loop Start: for(i=2:$N-1$)

$g_i = \frac{(2+Pr\Delta\eta f_i)g_{i+1}^{next}+(2-Pr\Delta\eta f_i)g_{i-1}^{next}}{4}$

g Loop End

Explicit Solution Ends

$Error = 0$

Error Loop Start: for(i=1 to N)

$Error = Error + abs(g_i^{next} - g_i)$

Error Loop End

Convergence Condition: if Error is less or equal to $1 * 10^{-6}$ break loop.

Main Loop End

A.0.4 Blasius Laminar Compressible Flow C=1 Simulation Algorithm

The Blasius Laminar Compressible flow for $C = 1$ is solved by a Finite Difference Explicit algorithm, without the need of a shooting method.

The algorithm is as follows:

Inputs: L, N, g_w, Pr, Ma_e

Form η vector of Length L. Spacing: $\Delta\eta = \eta_2 - \eta_1$

Calculate B parameter: $B = Pr(\gamma - 1)Ma_e^2$

Initialization and Boundary Conditions: $f^{'} = ErrorFunction(\eta)$; $f_1 = 0$

Initialization and Boundary Conditions: $g = (g_w - 1)InverseErrorFunction(\eta) + 1$;

Main Loop Start: for (Iteration=1 to $1 * 10^{10}$)

Update: $f'^{next} = f'$; $g^{next} = g$

f Loop Start: for(i=1 to $N - 1$)

$f_{i+1} = f_i + \Delta\eta \frac{(f_{i+1}^{'next} + f_i^{'next})}{2}$

f Loop End

Explicit Solution Start:

$f^{'}$ Loop Start: for(i=2 : $N - 1$)

$f_i^{'} = \frac{(2+\Delta\eta f_i) f_{i+1}^{'next} + (2-\Delta\eta f_i) f_{i-1}^{'next}}{4}$

$f^{'}$ Loop End

Calculate $f^{''}$ from f'^{next}

g Loop Start: for(i=2 : $N - 1$)

$g_i = \frac{(2+\Delta\eta Pr f_i) g_{i+1}^{next} + (2-\Delta\eta Pr f_i) g_{i-1}^{next} + 2\Delta\eta^2 B f^{''} f^{''}}{4}$

g Loop End

Explicit Solution Ends

$error_{f'} = 0$

$error_{f'}$ Loop Start: for(i=1 to N)

$error_{f'} = error_{f'} + abs(f_i^{'next} - f_i^{'})$;

$error_{f'}$ Loop End

$error_g$ Loop Start: for(i=1 to N)

$error_g = abs(g_i^{next} - g_i)$

$error_g$ Loop End

Internal Loop convergence condition: if $error_{f'}$ and $error_g$ are less or equal to $1 * 10^{-6}$ break loop

Main Loop Ends

A.0.5 Blasius Laminar Compressible Flow for Varialble C Simulation Algorithm

The Blasius Laminar Compressible flow for C not equal to one is solved by a Finite Difference Explicit algorithm, without the need of a shooting method.

The algorithm is as follows:

Inputs: L, N, g_w, $Power$, Pr, Ma_e

Form η vector of Length L. Spacing: $\Delta\eta = \eta_2 - \eta_1$

Calculate B parameter: $B = Pr(\gamma - 1)Ma_e^2$

Initialization and Boundary Conditions: $f^{'} = ErrorFunction(\eta)$; $f_1 = 0$

Initialization and Boundary Conditions: $g = (g_w - 1)InverseErrorFunction(\eta) + 1$;

Main Loop Start: for (Iteration=1 to $1 * 10^{10}$)

Update: $f'^{next} = f'$; $g^{next} = g$

f Loop Start: for(i=1 : $N - 1$)

$f_{i+1} = f_i + \Delta\eta \frac{f'^{next}_{i+1} + f'^{next}_i}{2}$

f Loop End

Calculate $f^{''}$ from f'^{next}

Calculate $g^{'}$ from g^{next}

C and $C^{'}$ Loop Start: for (i=1 to N)

$C_i = (g_i^{next})^{Power-1}$

$C_i^{'} = (Power-1)(g_i^{next})^{Power-2}(g_i^{'})$

C and $C^{'}$ Loop End

Explicit Solution Start:

$f^{'}$ Loop Start: for(i=2 to $N-1$)

$f_i^{'} = \frac{(2C_i+\Delta\eta(C_i^{'}+f_i))f_{i+1}^{'next}+(2C_i-\Delta\eta(C^{'}+f_i))f_{i-1}^{'next}}{4C_i}$

$f^{'}$ Loop End

g Loop Start: for(i=2 to $N-1$)

$g_i = \frac{(2C_i+\Delta\eta(C_i^{'}+Prf_i))g_{i+1}^{next}+(2C_i-\Delta\eta(C_i^{'}+Prf_i))g_{i-1}^{next}+2\Delta\eta^2 BC_i f^{''}f^{''}}{4C_i}$

g Loop End

Explicit Solution Ends

$error_{f^{'}} = 0$

$error_{f^{'}}$ Loop Start: for(i=1 to N)

$error_{f^{'}} = error_{f^{'}} + abs(f_i^{'next} - f_i^{'})$

$error_{f^{'}}$ Loop End

$error_g = 0$

$error_g$ Loop Start: for(i=1 to N)

$error_g = error_g + abs(g_i^{next} - g_i)$

$error_g$ Loop End

Internal Loop convergence condition: if $error_{f^{'}}$ and $error_g$ are less or equal to $1 * 10^{-6}$ break loop

Main Loop Ends

A.0.6 Orr-Sommerfeld Equation Numerical Solution Code

The Orr-Sommerfeld Equation is solved by using a Finite Difference scheme and the EIG function in Matlab.

Note: This code is based on (Simpson, C. 2015b).

The algorithm is as follows:

Inputs: η, f, $f^{'}$, $f^{''}$, $f^{'''}$, Re_{min}, Re_{max}, N_{Re}, α_{min}, α_{max}, N_{α}

Form the logspace Re and linear space α coordinates based on their min, max and number of nodes values N.

Set Up δ equal to the boundary layer or displacement thickness.

Find new coordinate: $\xi = \frac{\eta}{\delta}$

Set Up: $U(\xi) = f^{'}(\eta)$, $U^{'}(\xi) = f^{''}(\eta)\delta$ and $U^{''}(\xi) = f^{'''}(\eta)\delta\delta$

Find the ξ vector; the length N_{ξ}; and the spacing $d\xi = \xi_2 - \xi_1$

Temporal Stability Solver Start

Outer Main Loop Start: for($i_{Re} = 1$ to N_{Re})

Store Reynolds coordinate: $Reynolds = Re_{i_{Re}}$

Inner Main Loop Start: for($j_{\alpha} = 1$ to N_{α})

Store α coordinate: $Alpha = \alpha_{j_{\alpha}}$

Form the matrix A Start:

Matrix A elements loop start: for($i = 1$ to N_{ξ})

$a_{1i} = -1$

$a_{2i} = U(\xi)_i * Alpha * Reynolds * \sqrt{-1} + 2 * Alpha^2$

$a_{3i} = -1 * U(\xi)_i * Alpha^3 * Reynolds * \sqrt{-1} - U^{''}(\xi)_i * Alpha * Reynolds * \sqrt{-1} - Alpha^4$

Matrix A elements loop ends

Matrix A diagonal elements loop start: for($i = 1$ to N_ξ)

$A_{2(i)} = a_{1(i)}$

$A_{1(i)} = -1 * 4 * a_{1(i)} + a_{2(i)}\Delta\xi^2$

$A_{0(i)} = 6 * a_{1(i)} - 2 * a_{2(i)} * \Delta\xi^2 + a_{3(i)} * \Delta\xi^4$

$A_{-1(i)} = -1 * 4 * a_{1(i)} + a_{2(i)}\Delta\xi^2$

$A_{-2(i)} = a_{1(i)}$

Matrix A diagonal elements loop ends

Build matrix A start:

Set: $i = 2$

$A_{i,i+2} = A_{2(i)}$

$A_{i,i+1} = A_{1(i)}$

$A_{i,i} = A_{0(i)}$

$A_{i,i-1} = A_{-1(i)}$;

Loop Start: for($i = 3$ to $N_\xi - 2$)

$A_{i,i+2} = A_{2(i)}$

$A_{i,i+1} = A_{1(i)}$

$A_{i,i} = A_{0(i)}$

$A_{i,i-1} = A_{-1(i)}$;

$A_{i,i-2} = A_{-2(i)}$;

Loop Ends

Set: $I = N_\xi - 1$

$A_{i,i+1} = A_{1(i)}$

$A_{i,i} = A_{0(i)}$

$A_{i,i-1} = A_{-1(i)}$;

$A_{i,i-2} = A_{-2(i)}$;

Build matrix A end

Build matrix B start:

Matrix B elements loop start: for($i = 1$ to N_ξ)

$b_{1(i)} = Alpha * Reynolds * \sqrt{-1}$

$b_{2(i)} = Alpha^3 * Reynolds * \sqrt{-1}$

Matrix B elements loop ends

Matrix B diagonal elements loop start: for($i = 1$ to N_ξ)

$B_{1(i)} = b_{1(i)} * \Delta\xi^3$

$B_{0(i)} = -2 * b_{1(i)} * \Delta\xi^3 + b_{2(i)}\Delta\xi^4$

$B_{-1(i)} = b_{1(i)} * \Delta\xi^3$

Matrix B diagonal elements loop ends

Build matrix B start:

Loop Start: for($i = 3$ to $N_\xi - 2$)

$B_{i,i-1} = B_{-1(i)}$

$B_{i,i} = B_{0(i)}$

$B_{i,i+1} = B_{1(i)}$

Loop Ends

Build matrix B end

Strike the first and final rows of Matrix A and B.

Solve the eigen value problem: $C = B^{-1} * A$.

Note: This can be done in Matlab by applying the following command:

$[Vector, diagonal] = eig(B|A)$. Note: This is the Matlab left division of B and A.

Store the maximum imaginary value of the eigen solution in matrix $C_{temporal(i_\alpha, i_{Re})}$

Inner Main Loop End

Outer Main Loop End

Use a contour plot to view the imaginary component of $C_{temporal(i_\alpha, i_{Re})}$ to obtain the neutral curves

Temporal Stability Solver End

A.0.7 Falkner Skan equation derivation

This section details the procedure used to derived the Falkner-Skan equations for incompressible flow.

Falkner-Skan (Falkner, V. M. and Skan, S. W. 1930) that similarity for the boundary layer equations was obtained when:

$$\eta = y\sqrt{\frac{U(x)(m+1)}{2\nu x}} \tag{A.1}$$

Where: $m = \beta/(2-\beta)$.

Knowing that the boundary layer has the following form:

$$U(x) = kx^m \tag{A.2}$$

Where k is a constant.

From the stream function, the velocity u is obtained as

$$u = kx^m f' \tag{A.3}$$

Where prime indicates differentiation with respect to η.

From the continuity equation for an incompressible flow rearranging for v:

$$v = -\int_0^y \frac{\partial u}{\partial x} dy \tag{A.4}$$

Substituting equation A.3 into equation A.4 yields:

$$v = \frac{U(x)}{2x}\sqrt{\frac{2\nu x}{(m+1)\,U(x)}}\left\{-mf - m\eta f' + \eta f' - f\right\} \tag{A.5}$$

Substituting this equations A.3 and A.5 into the incompresible flow boundary layer equations, canceling the corresponding terms, and after some manipulation this equation gives:

$$f'''(\eta) + \beta\left(1 - f'(\eta)\, f'(\eta)\right) + f(\eta)\, f''(\eta) = 0 \tag{A.6}$$

This is known as the Falkner-Skan similarity solution.

A similar solution is achieved if instead of the similarity coordinate of equation A.1 the following similarity coordinate is used:

$$\eta = y\sqrt{\frac{U(x)}{2\nu x}} \tag{A.7}$$

Then the Falkner-Skan equation for incompressible flow becomes:

$$f'''(\eta) + m\left(f'(\eta)\, f'(\eta) - 1\right) + \frac{m+1}{2} f(\eta)\, f''(\eta) = 0 \tag{A.8}$$

A similar procedure is used to obtain the similarity solution for the energy equation.

Bibliography

Alao, F. I. and Folarin, S. B. (2013). Similarity solution of the influence of the thermal radiation and heat transfer on steady compressible boundary layer flow. *Open Journal of Fluid Mechanics*, 82–85. [Cited on page(s): xii, 111, 113, 114, 137, 138]

Back, L. H. (1970). Acceleration and cooling effects in laminar boundary layers-subsonic, transonic, and supersonic speeds. *AIAA Journal 8*, 794–802. [Cited on page(s): 107, 108, 110, 136, 146, 166]

Bae, Y. Y. and Emanuel, G. (1996). Tables for boundary-layer thicknesses of similar compressible laminar flow. *KSME International Journal 11*, 457–467. [Cited on page(s): 107, 108]

Blasius, H. (1908). Grenzschichten in flüssigkeiten mit kleiner reibung. *Z. Angew. Math. Phys. 56*, 1–37. [Cited on page(s): 3, 18]

Cengel, Y. A. and Cimbala, J. M. (2014). *Fluid Mechanichs Fundamentals and Applications*. McGraw-Hill. [Cited on page(s): ix, 2, 5, 6, 15, 52, 57, 75, 76, 147]

Cengel, Y. A. and Ghajar, A. J. (2015). *Heat and Mass Transfer Fundamentals and Applications*. McGraw-Hill. [Cited on page(s): 2, 3, 5, 16, 17, 52, 57, 58, 59, 61, 75, 76, 147]

Cimbala, J. M. Temporal stabiliyt of locally parallel flow - the orr-sommerfeld equation. Penn State University. [Cited on page(s): 41]

Clay Mathematics Institute. Navier-Stokes Equation. https://www.claymath.org/millennium/navier-stokes-equation/. [Cited on page(s): 1, 75]

Cohen, C. B. and Reshotcko, E. (1955). Similar solutions for the compressible laminar boundary layer with heat transfer and pressure gradient. Technical report, National Advisor Committtee for Aeronautics. [Cited on page(s): xi, xii, 7, 105, 124, 125, 126, 127, 128]

Falkner, V. M. and Skan, S. W. (1930). Falkner and Skan solutions. *Aeronautical Research Council Rep. and Mem. 1314*, 1–37. [Cited on page(s): 3, 19, 102, 181]

Goldstein, S. (1938). *Modern Developments in Fluid Dynamics an Account of Theory and Experiment Relating to Boundary Layers, Turbulent Motion and Wakes*. Oxford at the Clarendon Press. [Cited on page(s): 59]

Han, S. (2013). Finite difference solution of the falkner-skan flow equation. *International Journal of Mechanical Engineering Education. 41*(1). [Cited on page(s): 7, 13, 21]

Harris, S. D., Ingham, D. B. and Pop, I. (2002). Unsteady heat transfer in impulsive Falkner-Skan flows: Constant wall temperature case. *European Journal of Mechanics B/Fluids 21*, 447–468. [Cited on page(s): 76, 77, 79, 165]

Harris, S. D., Ingham, D. B. and Pop, I. (2008). Unsteady heat transfer in impulsive Falkner -Skan flows: Constant wall heat flux case. *Acta Mech 201*, 185–196. [Cited on page(s): 76, 77, 79, 165]

Kaups, K. and Smith, A. M. O. (1967). The laminar boundary layer in water with variable properties. *The American Society of Mechanical Engineers*. [Cited on page(s): 7]

Lipatov, I. I. and Ngo, K. T. (2020). Solutions of Falkner-Skan equations for hypersonic flows. *Fluid Dynamics 55*(4), 525–533. [Cited on page(s): 7, 8]

Malik, M. (1989). Prediction and control of transition in supersonic and hypersonic boundary layers. *AIAA Journal 27*(11), 1487. [Cited on page(s): 9]

Mukhopadhyay, S. (2009). Effects of radiation and variable fluid viscocity on flow and heat transfer on a symmetric wedge. *Journal of Applied Fluid Mechanics 2*(2), 29–34. [Cited on page(s): 113]

Murphy, J. S. (1965). Extensions of the Falkner-Skan similar solutions to flows with surface curvature. *AIAA Journal 3*, 2043–2049. [Cited on page(s): 8, 58, 60, 63, 65, 74, 164]

Ozgen, S. Linear stability theory. *Middle East Technical University, Dept. Aerospace Eng., Turkey*. [Cited on page(s): 8]

Ozgen, S. (2004). Effect of heat transfer on stability and transition characteristics of boundary layers. *International Journal of Heat and Mass Transfer 47*, 4697–4712. [Cited on page(s): 8, 40, 52, 53]

Ozgen, S. and Kircah, S. A. (2008). Linear stability analysis in compressible, flat-plate boundary-layers. *Theor. Comput. Fluid Dyn.*, 1–20. [Cited on page(s): 9, 52]

Ramirez, M. A. and Araya, G. (2020). Examination of compressibility effects in the Falkner-Skan equations. 5^{th} *Thermal and Fluids Engineering Conference (TFEC)*, 687–706. [Cited on page(s): 7]

Ramirez, M. A. and Araya, G. (2022). Falkner-Skan similarity flow solutions subject to wall curvature and passive scalar transport. *Procs. of the* 7^{th} *Thermal and Fluids Engineering Conference (TFEC2022)*, 1493–1508. [Cited on page(s): 62, 65, 74]

Ramirez, M. A. and Araya, G. (2023). Unsteady incompressible thermal laminar boundary layers subject to streamwise pressure gradients. *Proceedings of the* 21^{st} *International Conference of Numerical Analysis and Applied Mathematics, Crete, Greece 11-17 September 2023*. [Cited on page(s): 86, 101]

Ramirez, M. A. and Araya, G. (2025). Stability analysis of unsteady laminar boundary layers subject to streamwise pressure gradient. *Fluids 10*(100). [Cited on page(s): 86, 101]

Schlichting, H. and Gersten, K. (2017). *Boundary-Layer Theory*. Springer. [Cited on page(s): 59]

Schmisseur, J. D. (2013). Hypersonics into the 21st century: A perspective on afosr-sponsored research in aerothermodynamics. *43rd AIAA Fluid Dynamics Conference AIAA 2013-2606*. [Cited on page(s): ix, 2]

Simpson, C. (2015a). Derivation and nondimensionalization of the Orr-Sommerfeld equation. https://www.cdsimpson.net/2015/04/derivation-of-orr-sommerfeld-equation.html. [Cited on page(s): 41, 43, 148, 149, 162, 167]

Simpson, C. (2015b). Temporal and spatial stability analysis of the Orr-Sommerfeld equation. https://www.cdsimpson.net/2015/04/temporal-and-spatial-stability-analysis.html. [Cited on page(s): 10, 46, 148, 149, 162, 167, 178]

Tani, I. (1977). History of boundary layer theory. *Annual Review of Fluid Mechanics 9*, 87–111. [Cited on page(s): 2]

Tennekes, H. and Lumley, J. M. (1972). *A First Course in Turbulence*. Massachusets: MIT Press. [Cited on page(s): 5]

Warhaft, Z. (2000). Passive scalars in turbulent flows. *Ann. Rev. Fluid Mechanics 32*, 203–240. [Cited on page(s): 58]

Wazzan, A. R., Okamura, T. and Smith, A. M. O. (1968). The stability of water flow over heated and cooled flat plates. *Journal of Heat Transfer*, 109–114. [Cited on page(s): 9, 40, 53]

Wazzan, A. R., Okamura, T. T. and Smith, A. M. O. (1968). Spatial and temporal stability charts for the Falkner-Skan boundary layer profiles. Technical report, Mcdonnell Douglas. [Cited on page(s): xiii, 8, 148, 149, 155, 162, 167]

White, F. M. (1991). *Viscous Fluid Flow*. MacGraw-Hill. [Cited on page(s): ix, xi, 3, 4, 10, 18, 29, 30, 39, 40, 41, 43, 50, 51, 52, 57, 58, 61, 64, 65, 68, 69, 70, 71, 76, 105, 116, 147, 148, 163]

Zill, D. and Warren, W. (2013). *Differential Equations with Boundary Value Problems*. Brooks Cole Cengage Learning. [Cited on page(s): 5, 12, 21]

Zurigat, Y. H., Nayfeh, A. H. and Masad, J. A. (1992). Effect of pressure gradient on the stability of compressible boundary layers. *AIAA Journal 30*(9), 2204–2211. [Cited on page(s): 9]